Supporting information for the manuscript:

Binuclear and trinuclear 3*d*-metal complexes of HATNA and HAT(CN)$_6$ with unique magnetic behavior: from extremely strong antiferromagnetic coupling to opposite sign of zero-field splitting in the same complex.

Maxim V. Mikhailenko,[a] Tatiana Yu. Astakhova,[b] Elena N. Timokhina,[b] Maxim A. Faraonov,[a] Alexey V. Kuzmin,[c] Salavat S. Khasanov,[c] Denis V. Korchagin,[a] Gennady V. Shilov,[a] Akihiro Otsuka,[d] Hiroshi Kitagawa,[d] and Dmitri V. Konarev*[a]

[a]Federal Research Center of Problems of Chemical Physics and Medicinal Chemistry RAS, Chernogolovka, Moscow region, 142432 Russia; E-mail: konarev3@yandex.ru

[и]Emanuel Institute of Biochemical Physics, RAS, Moscow, Russia

[c]Institute of Solid State Physics RAS, Chernogolovka, Moscow region, 142432 Russia

[d]Division of Chemistry, Graduate School of Science, Kyoto University, Sakyo-ku, Kyoto, 606-8502, Japan

Table of contents

IR-spectra of the complexes

Table S1. IR-spectra (cm^{-1} in KBr pellets) of starting compounds and complexes **1**–**3**.

	Cp^*_2Fe	HATNA	$C_6H_4Cl_2$	C_6H_{14}	$(Cp^*_2Fe^+)[(Co^{II}I_2)_2 \cdot HATNA]^- \cdot 2C_6H_4Cl_2 \cdot 0.5C_6H_{14}$ (**1**)	$(Cp^*_2Fe^+)[(Fe^{II}I_2)_2 \cdot HATNA]^- \cdot 2C_6H_4Cl_2 \cdot 0.5C_6H_{14}$ (**2**)	$(Cp^*_2Fe^+)[(Mn^{II}I_2)_2 \cdot HATNA]^- \cdot 2C_6H_4Cl_2 \cdot 0.5C_6H_{14}$ (**3**)
$Cp^*_2Fe^+$	451s				445w*	447w*	-
	508w				497w	-	-
	589w				615s	615s	611m
	1025m				1016m*	1016m*	1026w*
	1071w				1084s	1084s	1081s*
	1356w				1352sh*	1344m	1364w*
	1370m				1373s*	1369m*	1373m*
	1422w				1425m*	1419w*	1421s*
	1447w				1454m*	1454m*	-
	1472w				1472m*	1469m*	1469w*
	2852w				2849w*	2852sh*	2858sh*
	2893w				2918w	2909w*	2909w
	2942w				2952w*	-	-
	2963w				-	2958w*	2959w
HATNA		413m			413m*	411m*	-
		501w			497w*	-	-
		541w			532w*	531w*	-
		606m			615s*	611m*	611m*
		757s			751s*	753s*	752s*
		771m			767m*	764s*	765s*
		802w			796w*	-	781sh*
		1020w			1016m*	1016w*	1026w*
		1078s			1084s*	1084s*	1081s*
		1129w			1137s*	1127s*	1133s*
		1236w			1244s*	1230m*	1223m
		1339m			1323sh	1344m*	1342m*
		1364m			1373s*	1369m*	1364w*
		1475w			1472m*	1469m*	1469w*
		1495m			1501m*	1499m*	1499w*
		1521w			1533w	1535w	-
		1611w			1614w*	1626w	1626w
		3056w			3057w*	3055w*	3060w*
Solvent			657w		656w*	657w*	660w*
			748s		751s*	760s	760s
			1030m		1016m	1016w*	1026w*
			1122m		1137s	1127s*	1133s*
			1453m		1425m*	1454m*	1469w
				722s	-	730sh*	-
				758w	751s*	760s*	765s*
				882m	900s	901w	901w
				1065m	1084s	1084s	1081s
				1342m	1323sh	1344m*	1342m*
				1373s	1373s*	1369m*	1364w*
				1460s	1472m	1454m*	1469w*

*****bands coincide, w - weak, m - middle, s – strong, vs- very strong intensity, sh- shoulder.

Table S2. IR-spectra (cm^{-1} in KBr pellets) of starting compounds and complexes **4** and **5**.

	Cp^*_2Fe	HATNA	$HAT(CN)_6$	$C_6H_4Cl_2$	$(Cp^*_2Fe^+)[(Fe^{II}I_2)_3 \cdot HATNA]^- \cdot C_6H_4Cl_2$ (**4**)	$(Cp^*_2Fe^+)_3[(Fe^{II}I_2)_3 \cdot HAT(CN)_6]^{3-} \cdot 4C_6H_4Cl_2$ (**5**)
$Cp^*_2Fe^+$	451s				452w*	458w*
	508w				509w*	527w
	589w				591w*	589w*
	1025m				1021m*	1030s*
	1071w				1072sh*	-
	1356w				1321w	1340w
	1370m				1376m*	1373s*
	1422w				1425w*	1423w*
	1447w				1457sh*	1452s*
	1472w				1468s*	1473w*
	2852w				-	2861sh*
	2893w				2906w	2909w
	2942w				2952w*	-
	2963w				2975w	2967w
HAT		413m	418s		-	-
		501w	462w		509w*	458w*
		541w	534w		530w	527w
		606m	621w		626s	653m
		757s	709w		759s*	-
		771m	808w		-	-
		802w	923w		790m	945w
		1020w	1146m		1021m*	1144m*
		1078s	1230s		1072sh*	1253w
		1129w	1341s		1137s*	1340sh*
		1236w	1364m		1241m*	1373s*
		1339m	1464m		1321w	1452s
		1364m	1560m		1376m	1562w*
		1475w	1706m		1468s*	1681w
		1495m	2241m		1489w*	2218s
		1521w			1537sh	
$C_6H_4Cl_2$		1611w			-	
		3056w			3061w*	
				657w	657w*	653m*
				748s	759s	750s*
				1030m	1021m*	1030s*
				1122m	1137s	1127m*
				1453m	1457sh*	1452s*

*****bands coincide, w - weak, m - middle, s – strong, vs- very strong intensity, sh- shoulder.

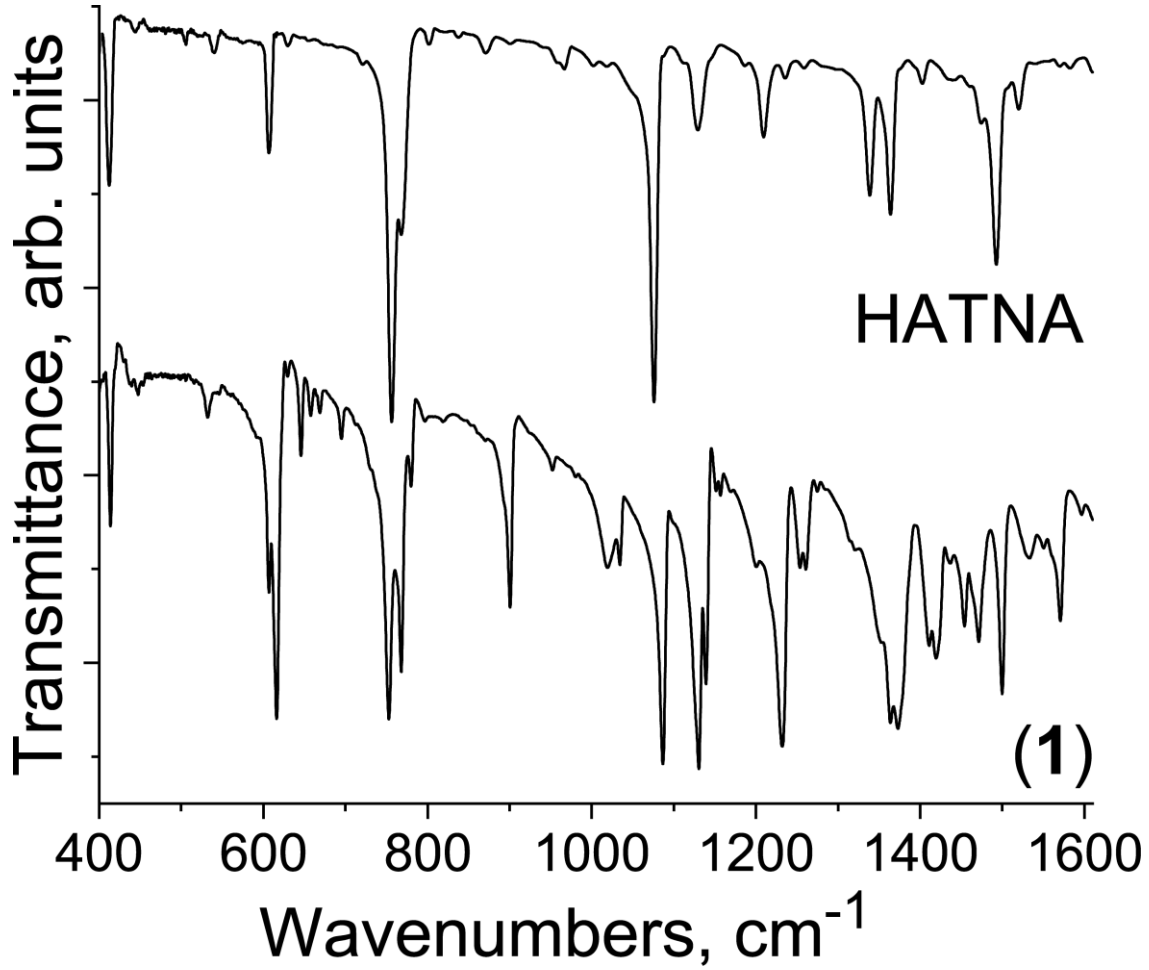

Figure S1. IR spectra of starting HATNA and complex **1** measured in KBr pellets. KBr pellet for **1** was prepared under anaerobic conditions in the glovebox.

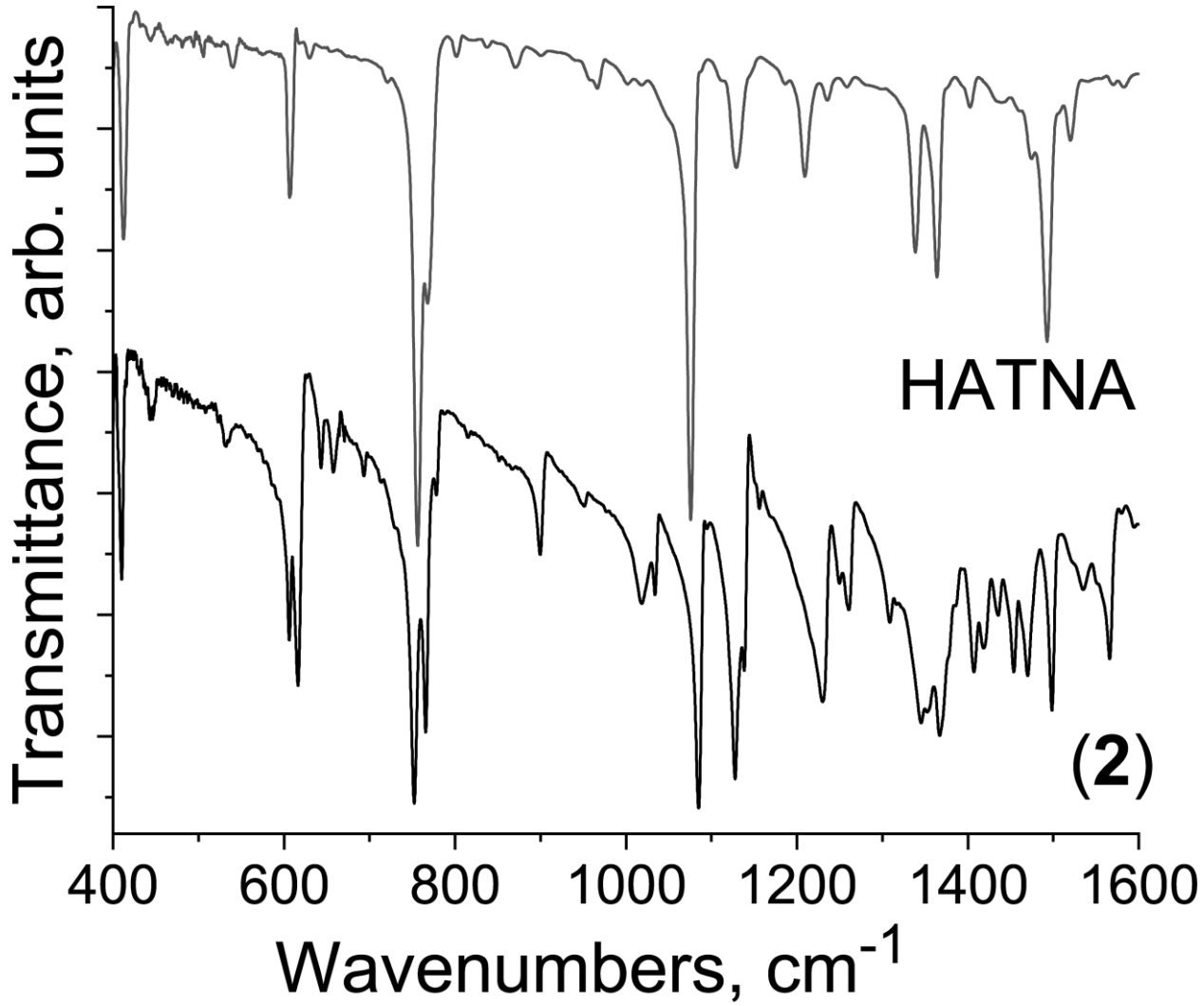

Figure S2. IR spectra of starting HATNA and complex **2** measured in KBr pellets. KBr pellet for **2** was prepared under anaerobic conditions in the glovebox.

‘

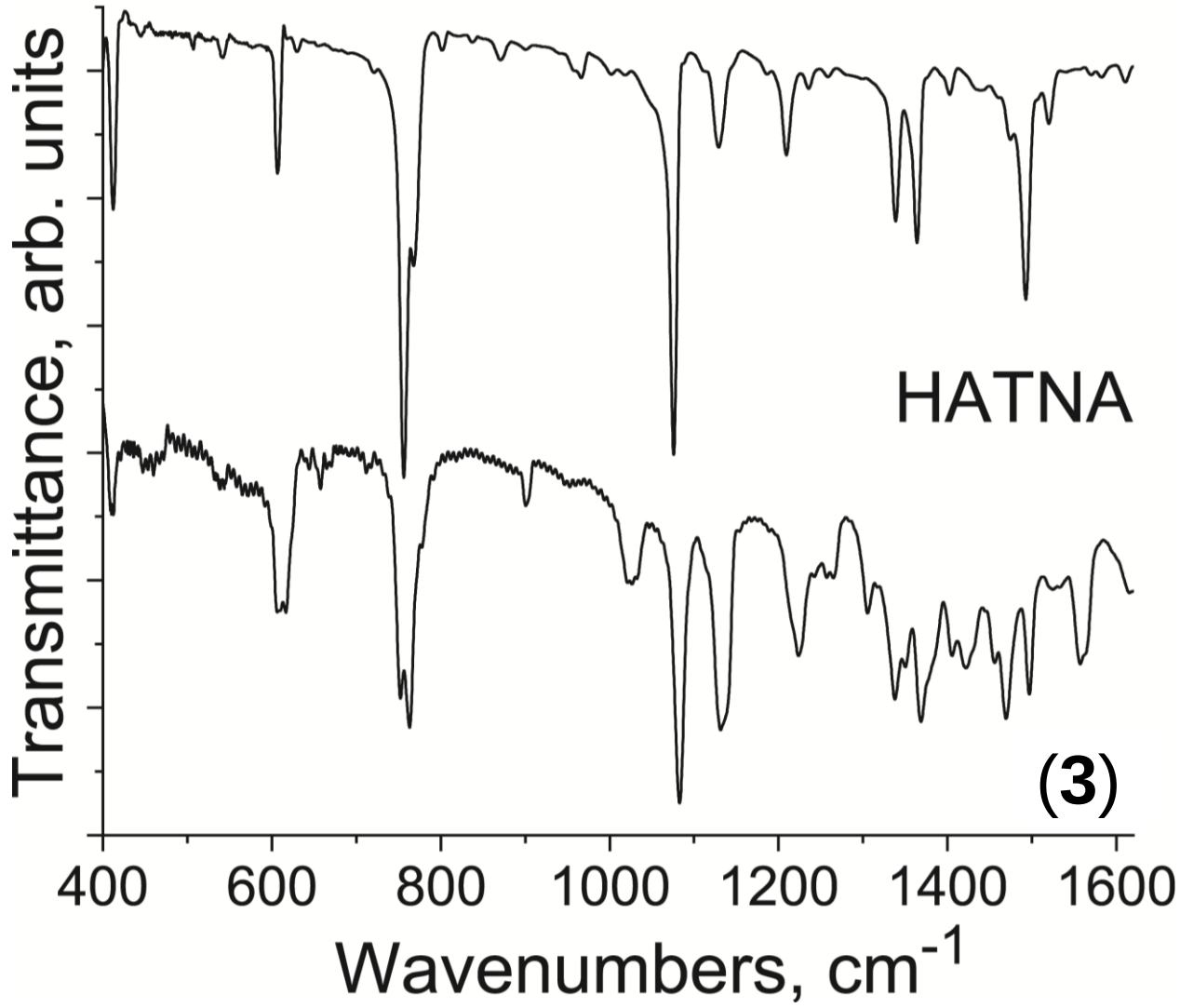

Figure S3. IR spectra of starting HATNA and complex **3** measured in KBr pellets. KBr pellet for **3** was prepared under anaerobic conditions in the glovebox.

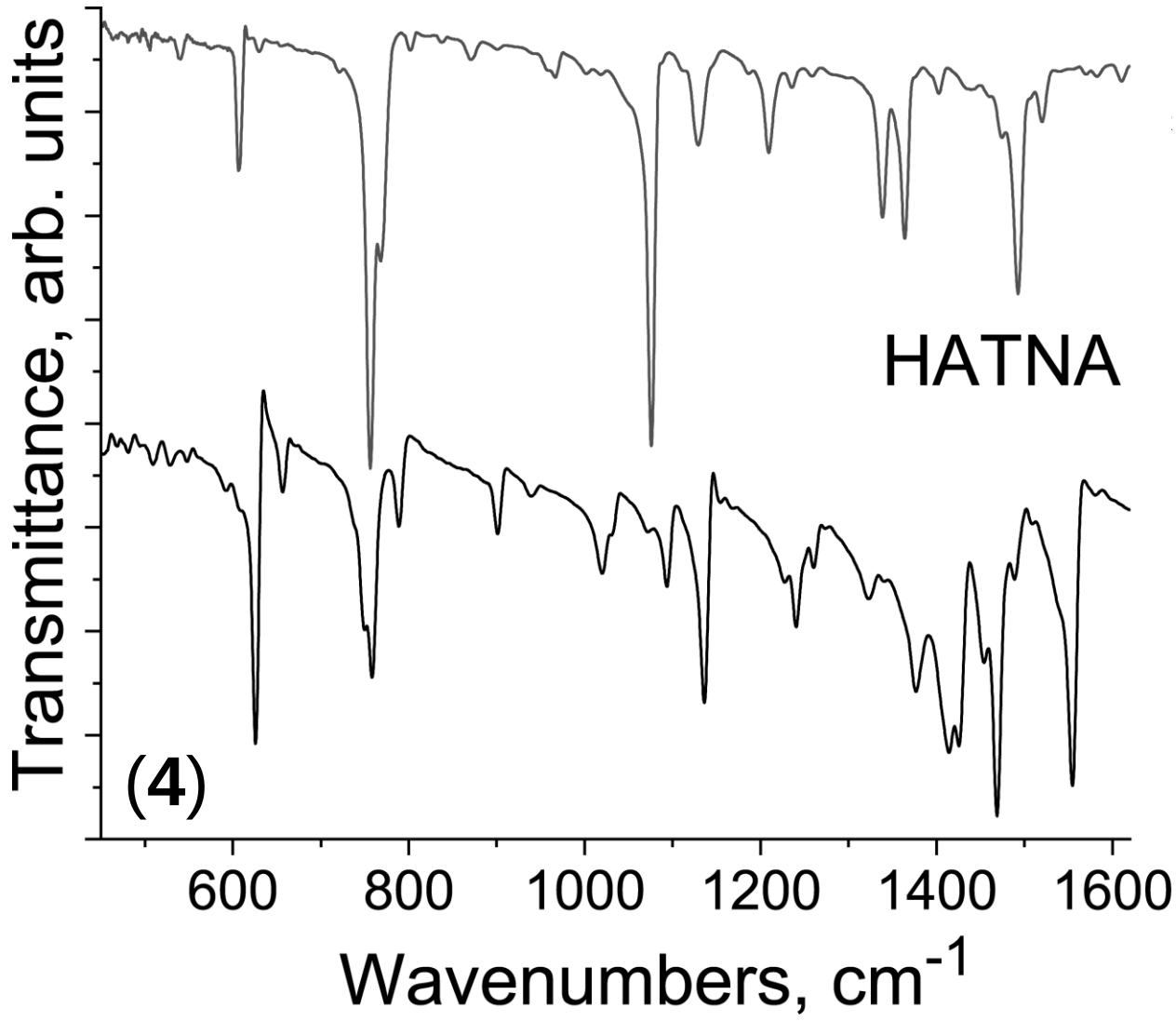

Figure S4. IR spectra of starting HATNA and complex **4** measured in KBr pellets. KBr pellet for **4** was prepared under anaerobic conditions in the glovebox.

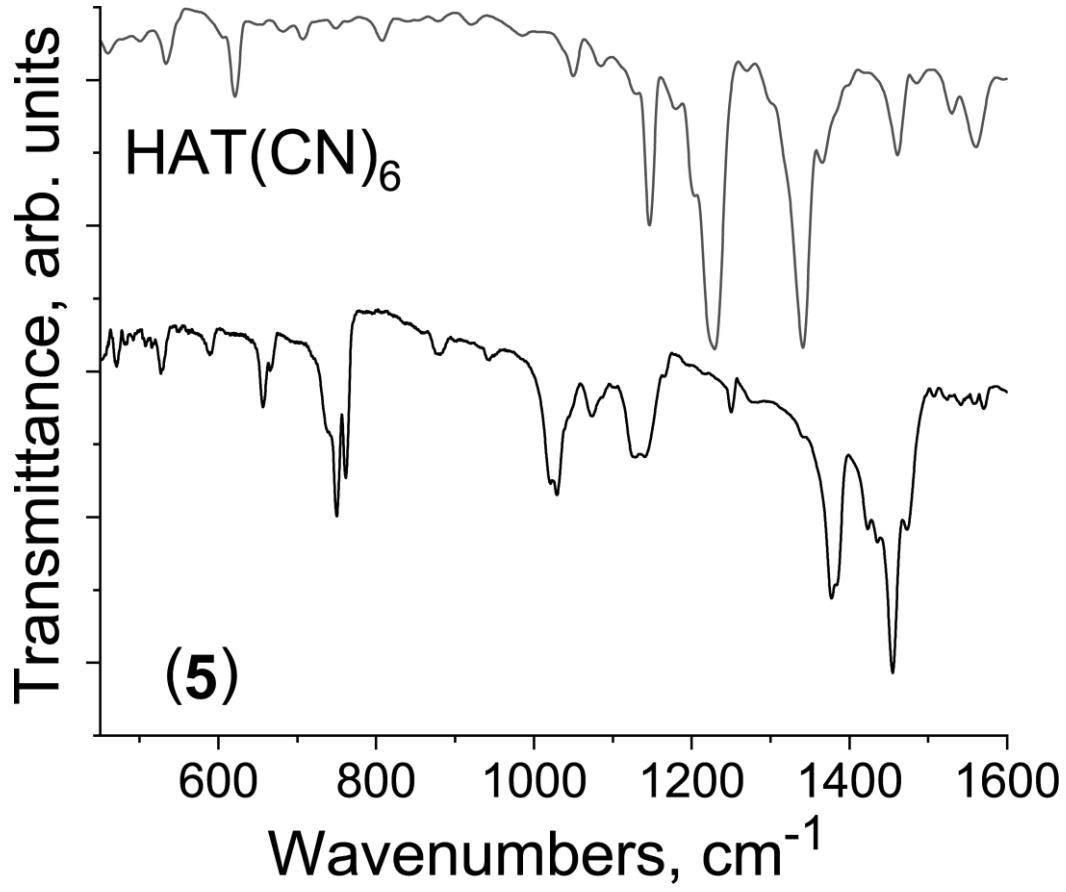

Figure S5. IR spectra of starting $HAT(CN)_6$ and complex **5** measured in KBr pellets. KBr pellet for **5** was prepared under anaerobic conditions in the glovebox.

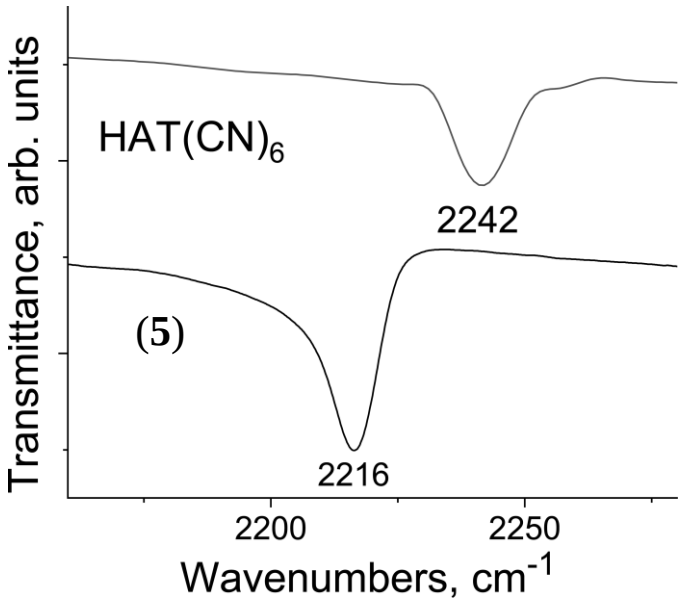

Figure S6. IR spectra of starting $HAT(CN)_6$ and complex **5** measured in KBr pellets in the 2160-2280 cm^{-1} range attributed to the CN vibrations. KBr pellet for **5** was prepared under anaerobic conditions in the glovebox.

Optical spectra

Table S3. Optical spectra of reference and obtained compounds **1**–**5**.

N	Components	UV-range	Visible range	NIR range CT bands
	HATNA	300, 390 (sh)		
	$HAT(CN)_6$	-		
1	$(Cp^*_2Fe^+)[(Co^{II}I_2)_2{\cdot}HATNA]^-{\cdot}C_6H_4Cl_2{\cdot}0.5C_6H_{14}$	335	568	1038, 1247
2	$(Cp^*_2Fe^+)[(Fe^{II}I_2)_2{\cdot}HATNA]^-{\cdot}C_6H_4Cl_2{\cdot}0.5C_6H_{14}$	325	800	1157
3	$(Cp^*_2Fe^+)[(Mn^{II}I_2)_2{\cdot}HATNA]^-{\cdot}C_6H_4Cl_2{\cdot}0.5C_6H_{14}$	336	-	1063, 1253
4	$(Cp^*_2Fe^+)[(Fe^{II}I_2)_3{\cdot}HATNA]^-{\cdot}C_6H_4Cl_2$	340		1053
5	$(Cp^*_2Fe^+)_3[(Fe^{II}I_2)_3{\cdot}HAT(CN)_6]^{3-}{\cdot}4C_6H_4Cl_2$	296, 376	580, 760	-

Optical properties of complexes **1**–**5** were studied in KBr pellets prepared in anaerobic conditions of the glovebox. Spectra of **1**–**4** indicate the formation of –1 charged units. Absorption band of starting HATNA is positioned in the UV range with maximum at 300 nm. At the reduction this band is red-shifted and maximum is appeared from 325 up to 340 nm. Previously it was shown [1] that indeed, maximum of this band is sensitive to the negative charge on the molecule and is red-shifted when formal charge of the coordination units with HATNA increases from –1 up to –3. Also all spectra show broad and rather intense bands with maxima at 1040-1160 nm (see Table S3 and Fig. S7). These spectra are similar to those studied previously for monoanionic units with HATNA binding two and three metal centers which showed these bands at 1160 and 1060 nm, respectively. It should be noted that dianions binding three metals can have completely different spectra manifesting two bands in the NIR range at 930 and 1034 nm, whereas in the trianions with three metals again only one broad band is manifested with maximum at 1070 nm [1].

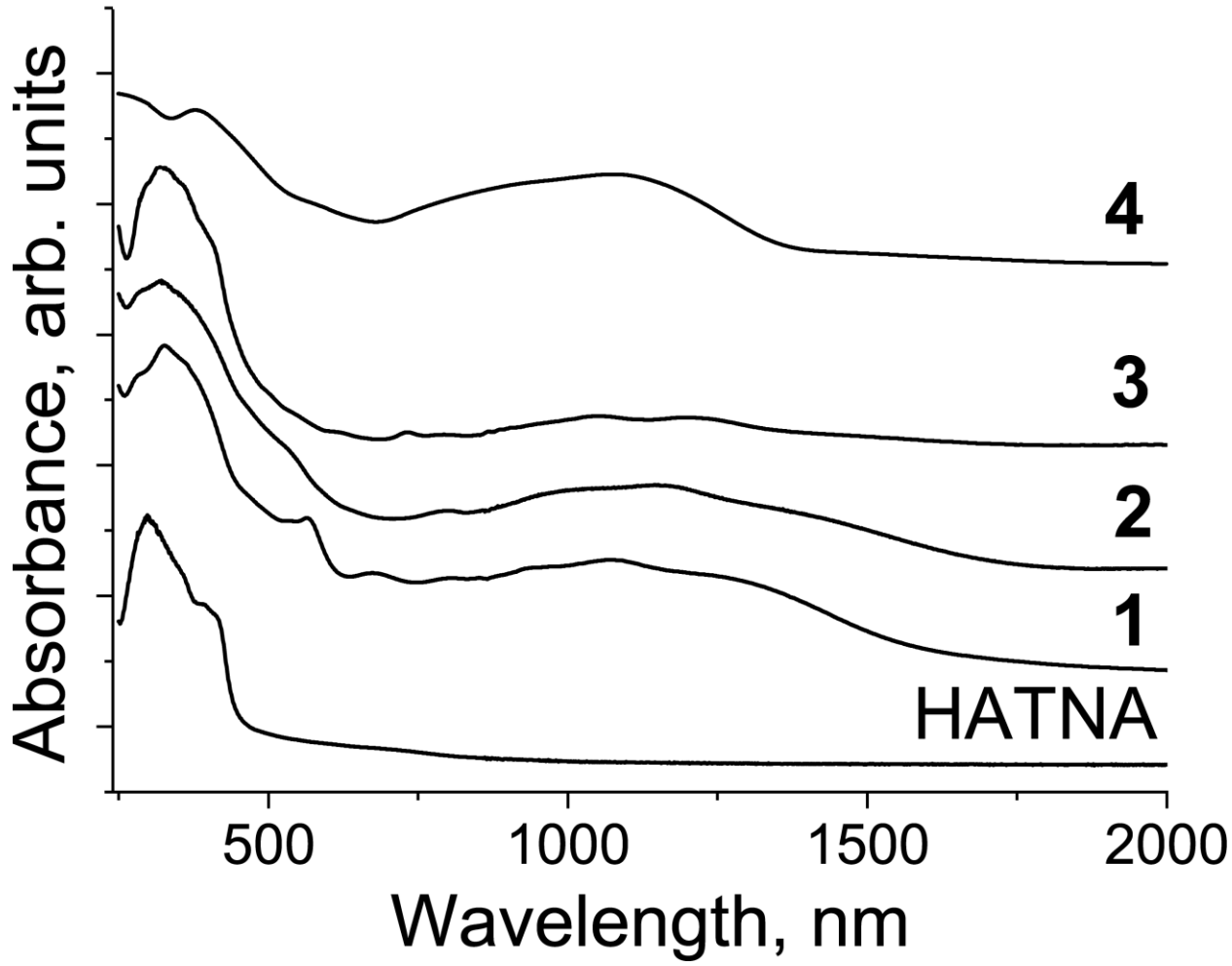

Figure S7. Spectra of starting HATNA and complexes **1**, **2**, **3** and **4** containing the $HATNA^{\bullet-}$ radical anions. Spectra are measured in KBr pellets which for **1**–**3** were prepared in anaerobic conditions of the glovebox.

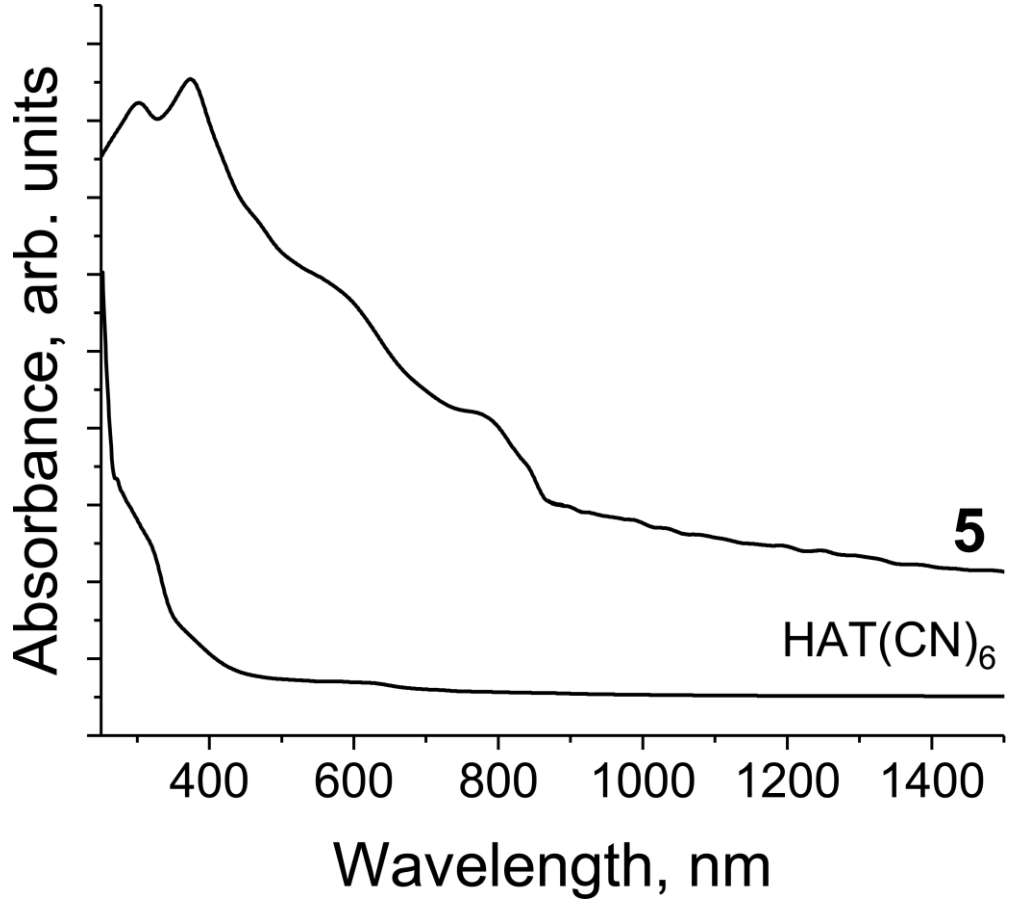

Figure S8. Spectra of starting $HAT(CN)_6$ and complex **5** containing the $HAT(CN)_6^{\bullet 3-}$ radical trianion. Spectra are measured in KBr pellet. Pellet for **5** was prepared in anaerobic conditions of the glovebox.

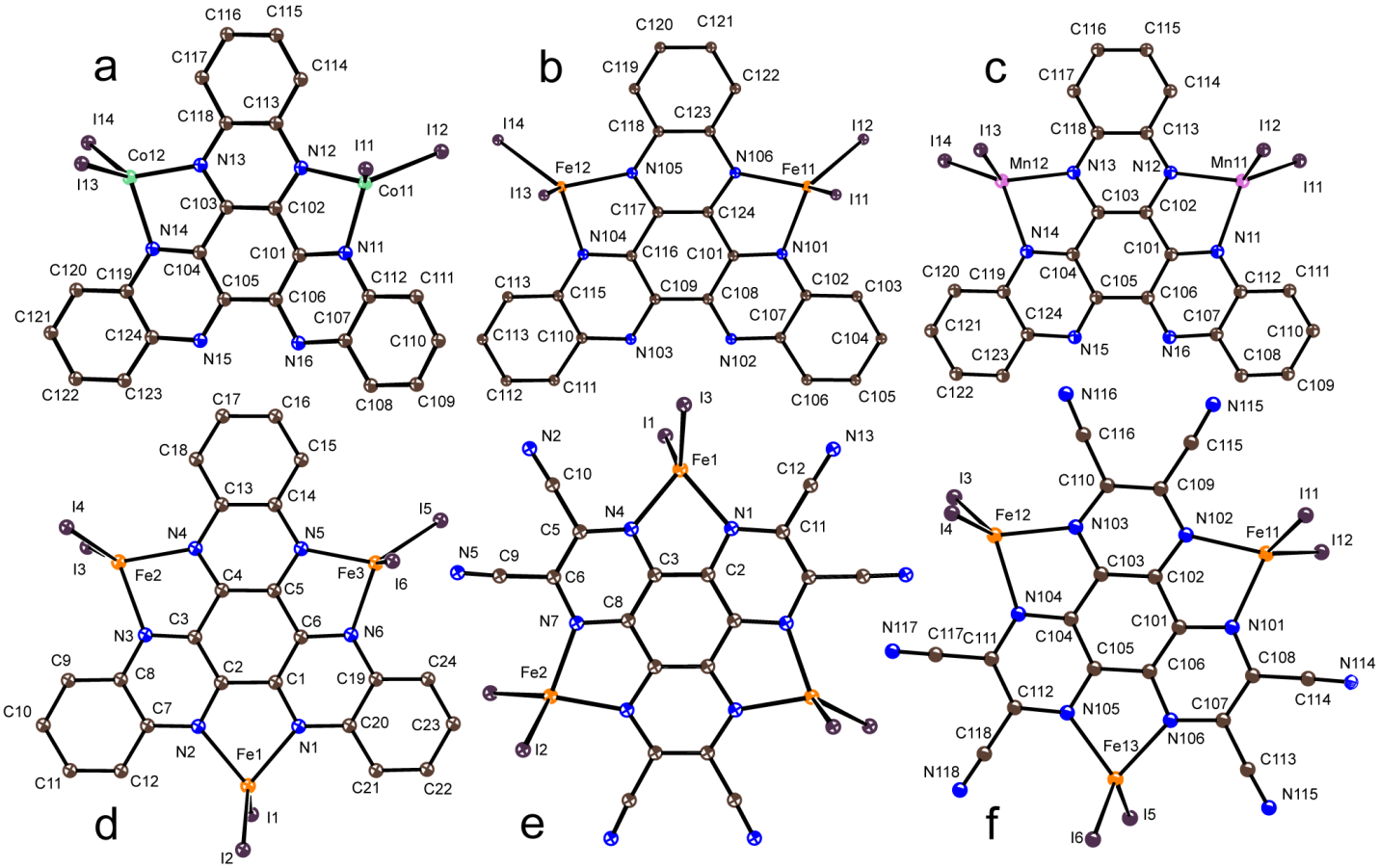

Figure S9. View on the molecular structure of anionic complexes with labeled atoms: (a) the $[(Co^{II}I_2)_2{\cdot}HATNA]^-$ anion in **1**; (b) the $[(Fe^{II}I_2)_2{\cdot}HATNA]^-$ anion in **2**; (c) the $[(Mn^{II}I_2)_2{\cdot}HATNA]^-$ anion in **3**; (d) the $[(Fe^{II}I_2)_3{\cdot}HATNA]^-$ anion in **4**; (e) the $[(Fe^{II}I_2)_3{\cdot}HAT(CN)_6]^{3-}$ trianion in **5** and (f) the $[(Fe^{II}I_2)_3{\cdot}HAT(CN)_6]^{2-}$ dianion in **6**. For complex **5** (e) only half of the molecule is independent.

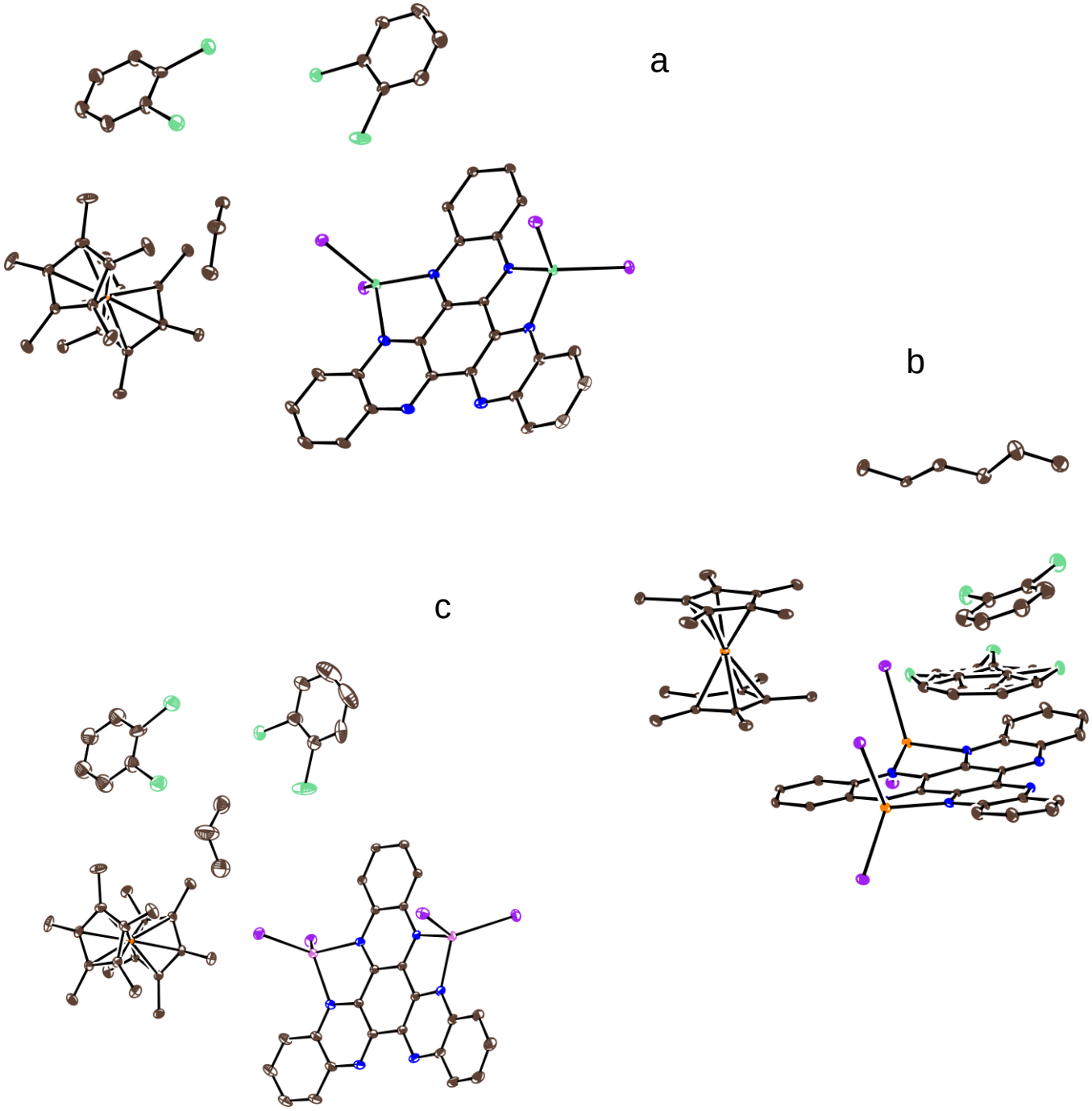

Figure S10. (a-c) Crystallographically independent units in the mononuclear coordination complexes **1, 2** and **3**, respectively. Carbon is brown, nitrogen is blue, chlorine is dark green, iodine is violet, cobalt is green, iron is orange and manganese is pink. Two independent $C_6H_4Cl_2$ molecules are observed with the 0.5 occupancy. In case of **3** one molecule is disordered with the 0.4/0.1 occupancy. In **1** and **2** only half of ordered *n*-hexane is independent, whereas in **3** n-hexane is disordered and molecule has 0.5 occupancy. Ellipsoid probability is 20%.

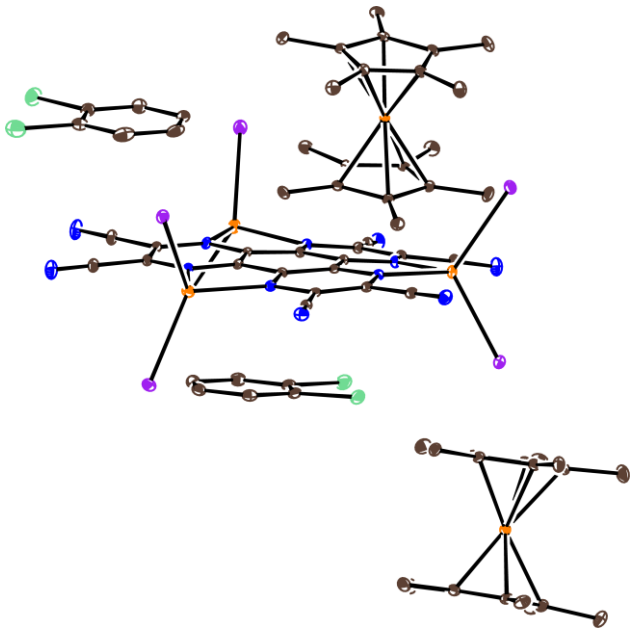

Figure S11. Crystallographically independent units in the coordination complex $(Cp^*_2Fe^+)_2[(Fe^{II}I_2)_3{\cdot}HAT(CN)_6]^{2-}{\cdot}2C_6H_4Cl_2$, for which only crystal structure is presented. Carbon is brown, nitrogen is blue, chlorine is dark green, iodine is violet, iron is orange. Ellipsoid probability is 20%.

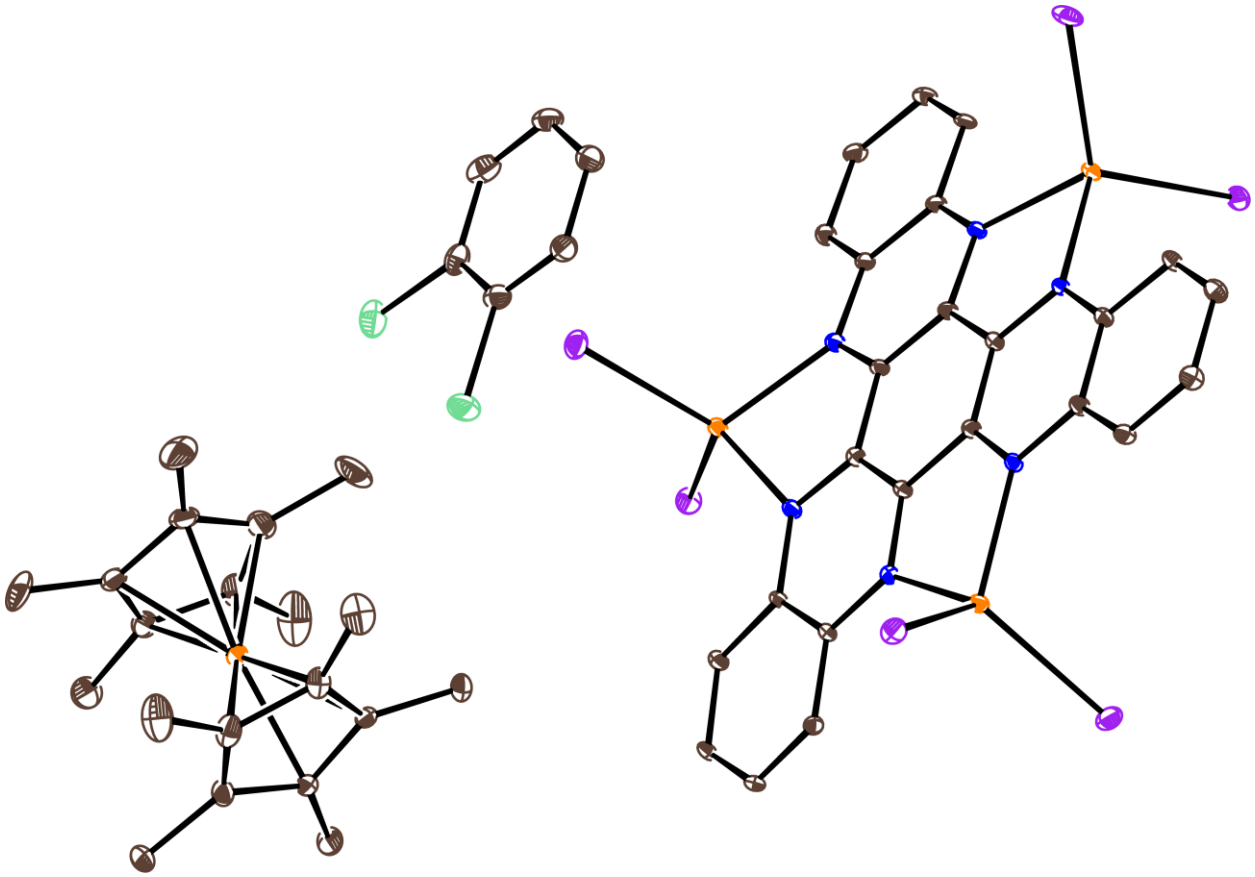

Figure S12. Crystallographically independent units in the coordination complex $(Cp^*_2Fe^+)[(Fe^{II}I_2)_3{\cdot}HATNA]^-{\cdot}C_6H_4Cl$, (**4**). It contains one crystallographically independent $Cp^*_2Fe^+$ cation; one $[(Fe^{II}I_2)_3{\cdot}HATNA]^-$ anion and one solvent $C_6H_4Cl_2$ molecule. Carbon is brown, nitrogen is blue, chlorine is dark green, iodine is violet, iron is orange. Ellipsoid probability is 20%.

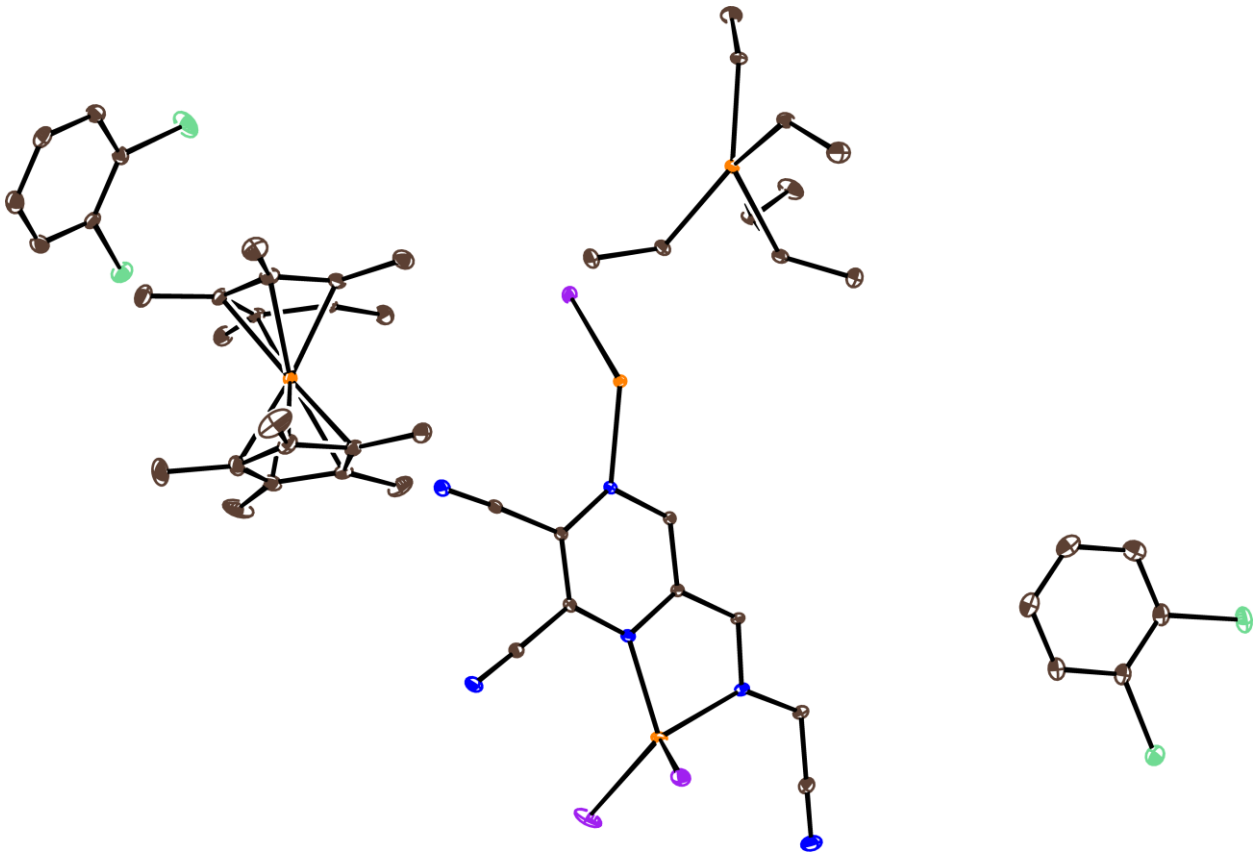

Figure S13. Crystallographically independent units in the coordination complex **(**$Cp^*_2Fe^+)_3[(Fe^{II}I_2)_3{\cdot}HAT(CN)_6]^{3-}{\cdot}4C_6H_4Cl_2$ (**5**). It contains one and half independent $Cp^*_2Fe^+$ anion; half independent $[(Fe^{II}I_2)_3{\cdot}HAT(CN)_6]^{3-}$ trianion and two solvent $C_6H_4Cl_2$ molecules. Carbon is brown, nitrogen is blue, chlorine is dark green, iodine is violet, iron is orange. Ellipsoid probability is 20%.

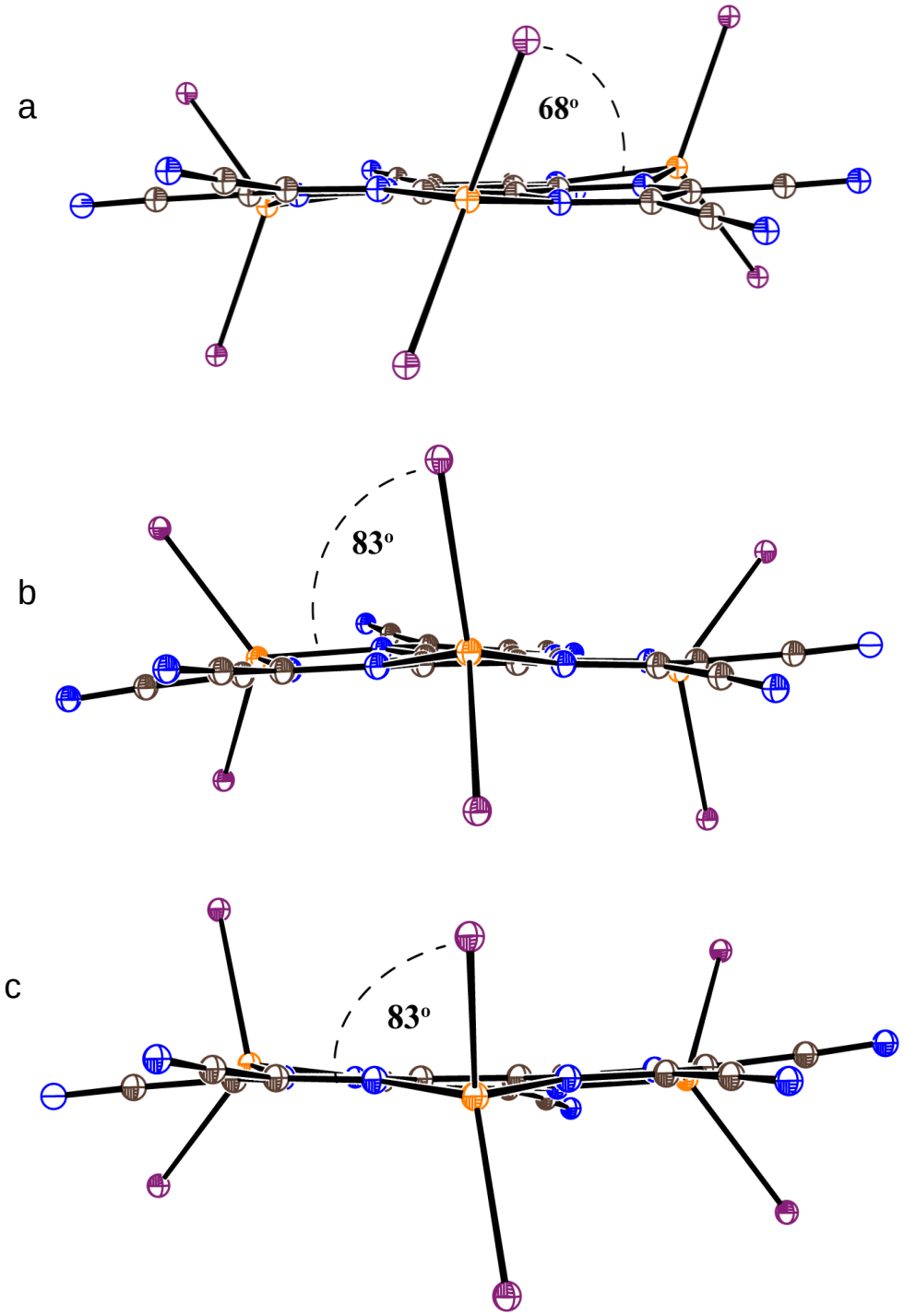

Figure S14. View on each of three Fe^{II} ions in the coordination complex **(**$(Cp^*_2Fe^+)_3[(Fe^{II}I_2)_3{\cdot}HAT(CN)_6]^{3-}{\cdot}4C_6H_4Cl_2$ (**5**). The Fe^{II} ion in the foreground in (a) is denoted as Fe^{II}_1 in the manuscript; the Fe^{II} ions in the foreground in (b) and (c) are denoted as Fe^{II}_2. Carbon is brown, nitrogen is blue, iodine is violet, iron is orange. Ellipsoid probability is 20%.

Crystal structure of 2.

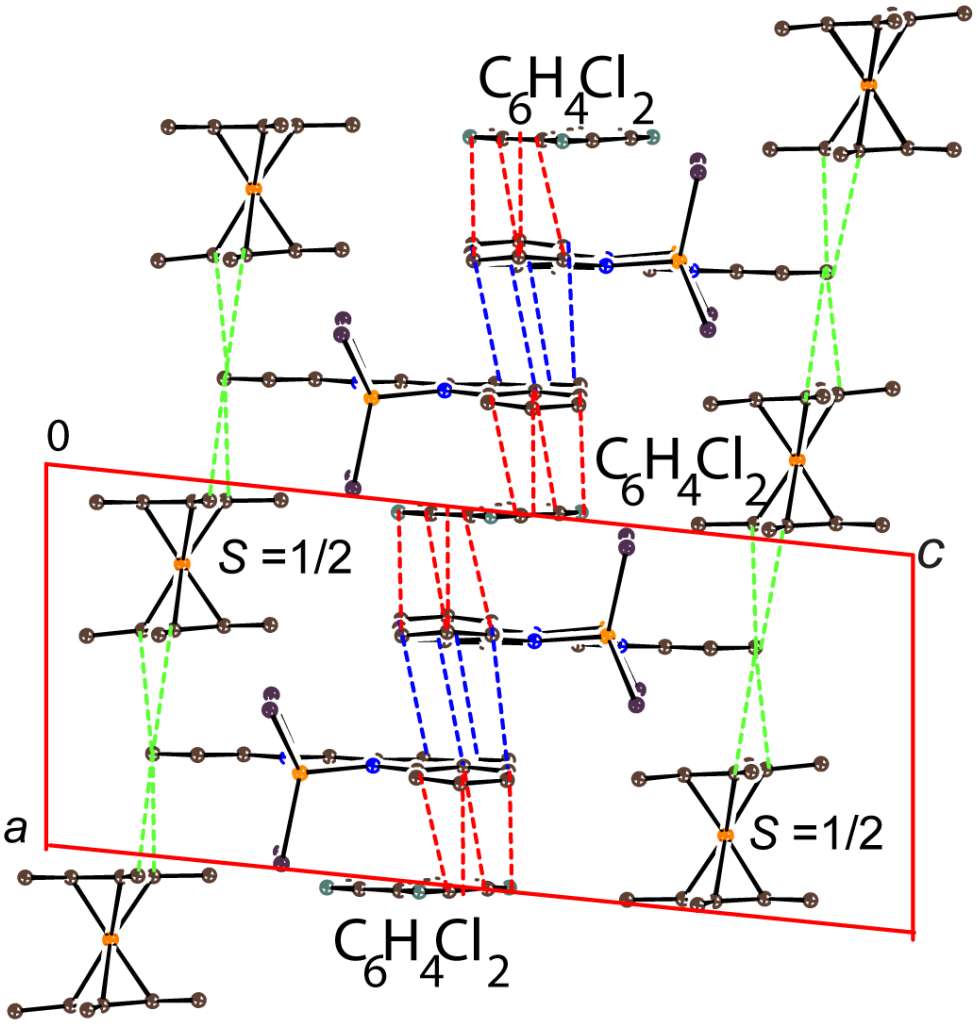

Figure S15. Molecular structure of complex: $(Cp^*_2Fe^+)[(Fe^{II}I_2)_2{\cdot}HATNA]^-{\cdot}C_6H_4Cl_2{\cdot}0.5C_6H_{14}$ (**2**). View on the stacks of $[(Fe^{II}I_2)_3{\cdot}HATNA]^-$ anions in which they are alternated with the $C_6H_4Cl_2$ molecules. Isotropic thermal parameters are shown. Van der Waals contacts of different π-π stacking motifs are shown by different colors: green for complex-$DmFc^+$, blue for complex-complex, red for complex-dichlorobenzene.

Crystal structure of 3.

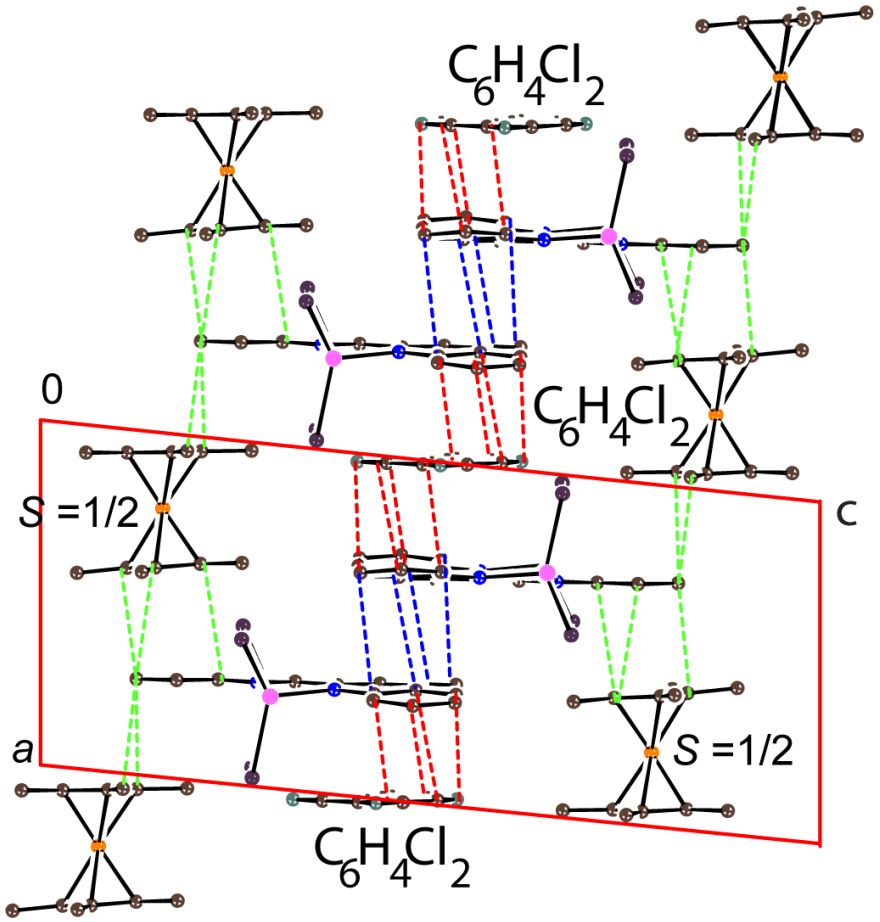

Figure S16. Molecular structure of complex: $(Cp^*_2Fe^+)[(Mn^{II}I_2)_2{\cdot}HATNA]^-{\cdot}C_6H_4Cl_2{\cdot}0.5C_6H_{14}$ (**3**). View on the stacks of $[(Mn^{II}I_2)_3{\cdot}HATNA]^-$ anions in which they are alternated with the $C_6H_4Cl_2$ molecules. Isotropic thermal parameters are shown. Van der Waals contacts of different π-π stacking motifs are shown by different colors: green for complex-$DmFc^+$, blue for complex-complex, red for complex-dichlorobenzene.

Crystal structure of $(Cp^*_2Fe^+)_2[(Fe^{II}I_2)_3{\cdot}HAT(CN)_6]^{2-}{\cdot}2C_6H_4Cl_2$

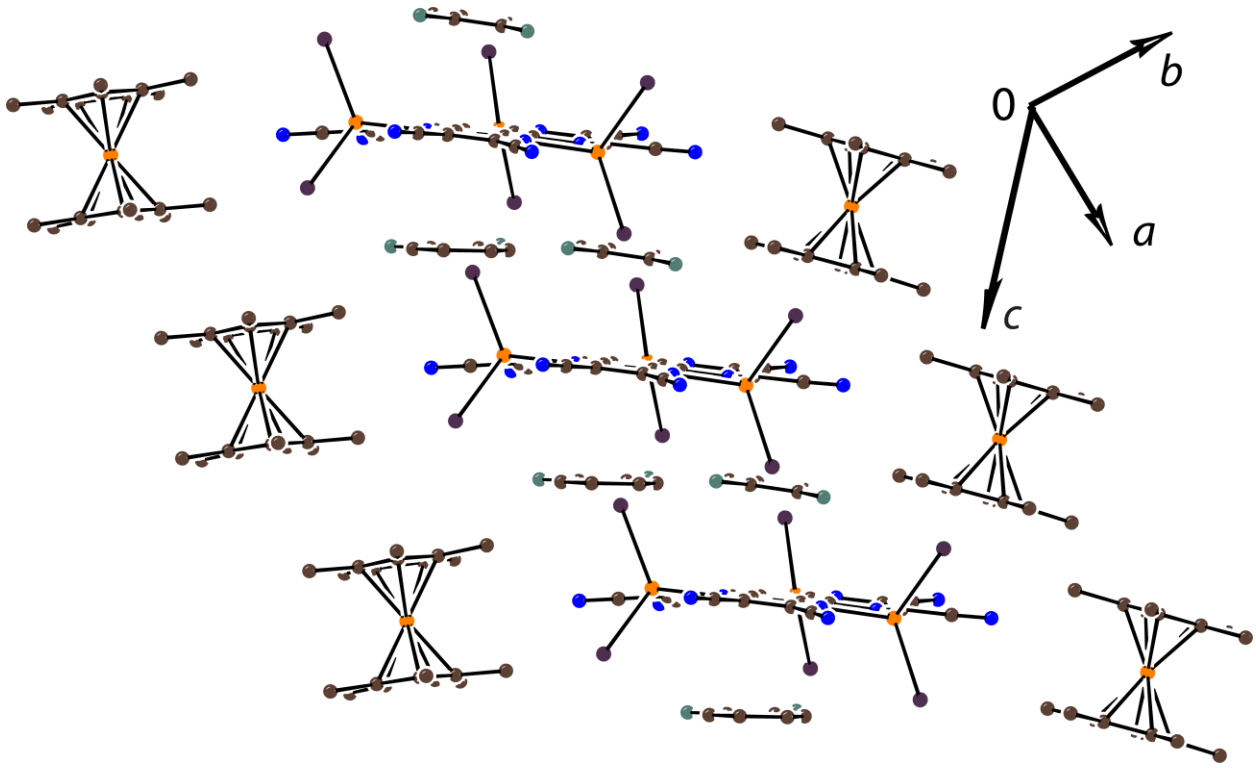

Figure S17. Molecular structure of complex: $(Cp^*_2Fe^+)_2[(Fe^{II}I_2)_3{\cdot}HAT(CN)_6]^{2-}{\cdot}2C_6H_4Cl_2$. View on the stacks from the isolated $[(Fe^{II}I_2)_3{\cdot}HAT(CN)_6]^-$ anions in which they are alternated with two $C_6H_4Cl_2$ molecules.

Spin Hamiltonians and fitting details

Complex **1** (two formula units):

$$\hat{H}_1 = -2J_{DmFc-MC} \cdot (\overrightarrow{\hat{S}_{DmFc1}}\,\overrightarrow{\hat{S}_{MC1}} + \overrightarrow{\hat{S}_{DmFc2}}\,\overrightarrow{\hat{S}_{MC2}}) - 2J_{MC-MC} \cdot \overrightarrow{\hat{S}_{MC1}}\,\overrightarrow{\hat{S}_{MC2}} + D_{MC} \cdot \sum_{i=1}^{2} (\hat{S}^2_{MCiz} - \frac{1}{3} \cdot \overrightarrow{\hat{S}_{MCi}}^2) + \mu_B(g_{DmFc}(\hat{S}_{DmFc1} + \hat{S}_{DmFc2}) + g_{MC}(\hat{S}_{MC1} + \hat{S}_{MC2})) \cdot \vec{H}$$

$J_{DmFc-MC}$ – intermolecular exchange coupling between decamethylferrocenium and molecular complex;

$\overrightarrow{\hat{S}_{DmFc1}}$ and $\overrightarrow{\hat{S}_{DmFc2}}$ – decamethylferrocenium spins;

$\overrightarrow{\hat{S}_{MC1}}$ and $\overrightarrow{\hat{S}_{MC2}}$ – conjugated spins of molecular complexes (S = 5/2);

D_{MC} – effective zero-field splitting of molecular complexes;

g_{DmFc} – decamethylferrocenium g-factor (fixed as 2.0);

g_{MC} – effective g-factor of molecular complexes.

Complex **2** ($\chi_M T$ fitting; two formula units):

$$\hat{H}_2 = -2J_{Fe-HAT} \cdot (\overrightarrow{\hat{S}_{Fe11}}\,\overrightarrow{\hat{S}_{HAT1}} + \overrightarrow{\hat{S}_{Fe12}}\,\overrightarrow{\hat{S}_{HAT1}} + \overrightarrow{\hat{S}_{Fe21}}\,\overrightarrow{\hat{S}_{HAT2}} + \overrightarrow{\hat{S}_{Fe22}}\,\overrightarrow{\hat{S}_{HAT2}}) - 2J_{MC-MC} \cdot (\overrightarrow{\hat{S}_{HAT1}}\,\overrightarrow{\hat{S}_{HAT2}} + \overrightarrow{\hat{S}_{Fe11}}\,\overrightarrow{\hat{S}_{Fe21}} + \overrightarrow{\hat{S}_{Fe11}}\,\overrightarrow{\hat{S}_{Fe22}} + \overrightarrow{\hat{S}_{Fe12}}\,\overrightarrow{\hat{S}_{Fe21}} + \overrightarrow{\hat{S}_{Fe12}}\,\overrightarrow{\hat{S}_{Fe22}}) + D_{Fe} \cdot \sum_{i=1}^{2} (\hat{S}^2_{Fe1iz} - \frac{1}{3} \cdot \overrightarrow{\hat{S}_{1i}}^2) + D_{Fe} \cdot \sum_{i=1}^{2} (\hat{S}^2_{Fe2iz} - \frac{1}{3} \cdot \overrightarrow{\hat{S}_{2i}}^2) + \mu_B(g_{Fe}(\hat{S}_{Fe11} + \hat{S}_{Fe12} + \hat{S}_{Fe21} + \hat{S}_{Fe22}) + g_{HAT}(\hat{S}_{HAT1} + \hat{S}_{HAT2})) \cdot \vec{H}$$

Additionally, intermolecular exchange coupling was taken into account as J_{inter} (zJ in PHI terminology). The data approximation in this case was conducted without a contribution from

two decamethylferrocenium cations. Therefore, this contribution was added afterwards as 0.75 emu·K/mol (theoretical value for two independent spins S = 1/2).

J_{Fe-HAT} – metal-radical exchange coupling between Fe^{II} ions and HATNA radical;

J_{MC-MC} – intermolecular exchange coupling between neighboring molecular complexes;

$\overrightarrow{\hat{S}_{Fe11}}$ and $\overrightarrow{\hat{S}_{Fe12}}$ – Fe^{II} spins of the first molecular complex;

$\overrightarrow{\hat{S}_{Fe21}}$ and $\overrightarrow{\hat{S}_{Fe22}}$ – Fe^{II} spins of the second molecular complex;

$\overrightarrow{\hat{S}_{HAT1}}$ and $\overrightarrow{\hat{S}_{HAT2}}$ – HATNA radical spins of two molecular complexes;

D_{Fe} – zero-field splitting of Fe^{II} ions;

g_{Fe} – Fe^{II} g-factor;

g_{HAT} – HATNA radical g-factor (fixed as 2.0).

Complex **2** (magnetization fitting; two formula units) – similar to complex **1** but the conjugated spin of each molecular complex S_{MC} is 7/2.

Complex **3** (one formula unit):

$$\hat{H}_3 = -2J_{Mn-HAT} \cdot \left(\overrightarrow{\hat{S}_{Mn1}}\overrightarrow{\hat{S}_{HAT}} + \overrightarrow{\hat{S}_{Mn2}}\overrightarrow{\hat{S}_{HAT}}\right) - 2J_{Mn-Mn} \cdot \overrightarrow{\hat{S}_{Mn1}}\overrightarrow{\hat{S}_{Mn2}} + \mu_B\left(g_{Mn}(\hat{S}_{Mn1} + \hat{S}_{Mn2}) + g_{HAT}\overrightarrow{\hat{S}_{HAT}} + g_{DmFc}\overrightarrow{\hat{S}_{DmFc}}\right) \cdot \vec{H}$$

Additionally, intermolecular exchange coupling was taken into account as J_{inter}.

J_{Mn-HAT} – metal-radical exchange coupling between Mn^{II} ions and HATNA radical;

J_{Mn-Mn} – metal-metal exchange coupling between Mn^{II} ions;

Complex **4** (one formula unit):

$$\hat{H}_4 = -2J_{Fe-HAT} \cdot (\overrightarrow{\hat{S}_{Fe1}}\overrightarrow{\hat{S}_{HAT}} + \overrightarrow{\hat{S}_{Fe2}}\overrightarrow{\hat{S}_{HAT}} + \overrightarrow{\hat{S}_{Fe3}}\overrightarrow{\hat{S}_{HAT}}) - 2J_{Fe-Fe} \cdot (\overrightarrow{\hat{S}_{Fe1}}\overrightarrow{\hat{S}_{Fe2}} + \overrightarrow{\hat{S}_{Fe1}}\overrightarrow{\hat{S}_{Fe3}} + \overrightarrow{\hat{S}_{Fe2}}\overrightarrow{\hat{S}_{Fe3}}) + D_{Fe} \cdot \sum_{i=1}^{3} (\hat{S}^2_{Feiz} - \frac{1}{3} \cdot \overrightarrow{\hat{S}_{Fei}}^2) + \mu_B(g_{Fe} \sum_{i=1}^{3} \overrightarrow{\hat{S}_{Fei}} + g_{HAT}\overrightarrow{\hat{S}_{HAT}} + g_{DmFc}\overrightarrow{\hat{S}_{DmFc}}) \cdot \vec{H}$$

Additionally, intermolecular exchange coupling was taken into account as J_{inter}.

Complex **5** ($\chi_M T$ fitting; one formula unit):

$$\hat{H}_5 = -2J_{Fe-HAT} \cdot (\overrightarrow{\hat{S}_{Fe1}}\overrightarrow{\hat{S}_{HAT}} + \overrightarrow{\hat{S}_{Fe2}}\overrightarrow{\hat{S}_{HAT}} + \overrightarrow{\hat{S}_{Fe3}}\overrightarrow{\hat{S}_{HAT}}) - 2J_{Fe-Fe} \cdot (\overrightarrow{\hat{S}_{Fe1}}\overrightarrow{\hat{S}_{Fe2}} + \overrightarrow{\hat{S}_{Fe1}}\overrightarrow{\hat{S}_{Fe3}} + \overrightarrow{\hat{S}_{Fe2}}\overrightarrow{\hat{S}_{Fe3}}) + D_{Fe1} \cdot \left(\hat{S}^2_{Fe1z} - \frac{1}{3} \cdot \overrightarrow{\hat{S}_{Fe1}}^2\right) + D_{Fe2} \cdot \left(\hat{S}^2_{Fe2z} - \frac{1}{3} \cdot \overrightarrow{\hat{S}_{Fe2}}^2 + \hat{S}^2_{Fe3z} - \frac{1}{3} \cdot \overrightarrow{\hat{S}_{Fe3}}^2\right) + \mu_B(g_{Fe} \sum_{i=1}^{3} \overrightarrow{\hat{S}_{Fei}} + g_{HAT}\overrightarrow{\hat{S}_{HAT}}) \cdot \vec{H}$$

Both $\chi_M T$ and magnetization data fitting did not include three decamethylferrocenium spins. As for the $\chi_M T$ fitting, 1.125 emu·K/mol, complying with three independent spins S = 1/2, was added afterwards. For magnetization fitting, a curve for three independent spins S = 1/2 was simulated separately and then added to the final data.

D_{Fe1} – zero-field splitting of one Fe^{II} ions (with unique geometry);

D_{Fe2} – zero-field splitting of two Fe^{II} ions (with similar geometry);

Error bars

The error bars were taken directly from PHI.

Reliability of the fitting parameters for complex multicomponent systems

The fitting of the $\chi_M T$ data for compound **2** was carried out separately from magnetization due to complexity of the considered system. J_1 was limited in the interval (–350…–550 cm^{-1}) between CASSCF values for Co^{II} complex **1** and Mn^{II} complex **3**. Importantly, the shape of the $\chi_M T$ data curve is very complex with two extremums and a slope at 300 K. So, with the addition of $J_{MC\text{-}MC}$ as a variable, which was already calculated from CASSCF, only one set of parameters was obtained.

For compound **4**, before CASSCF calculations were carried there were three fitting sets of parameters but two of them contained enormous J_1 and, therefore, these sets were unreasonable. Afterwards, theoretical study revealed decently close J values (Table S9) to the third set of parameters that is provided in the manuscript.

Considering equivalent J_1, J_2 and g_{Fe} for all three Fe^{II} ions in compound **5**, the fitting has only one solution provided in the manuscript. Making these parameters inequivalent for two different types of Fe^{II} ions widens the total amount of parameters to 8 and there can be several solutions but all of them imply a large difference (up twofold) in J_1 values for two types of Fe^{II} ions and so one of these two J_1 values becomes enormous. As the M-N bond lengths differ very slightly, twofold margin for metal-radical exchange coupling is unreasonable.

Magnetic data

Table S4. Data of SQUID measurements for complexes **1**–**5**.

N	Unit	N metals	Magnetic properties
1	$[(Co^{II}I_2)_2 \cdot HATNA]^{\bullet-}$	2	Spin system 1/2 - 5/2 - 5/2 - 1/2 (Fc - MC - MC - Fc) $J_{DmFc-MC}$ = −0.396(3) cm^{-1}, J_{MC-MC} = +0.046 cm^{-1} (fixed from DFT), $g_{(MC)}$ = 2.520(4), $D_{(MC)}$ = +22.1(3) cm^{-1} Θ = −4 K, $\chi_M T$ = 14.57 at 300 K (theoretical for two S = 3/2 and two S = 1/2 spins (2 units): $\chi_M T$ = 9) and 9.04 $\mu_B N_A$ at 50 kOe and 2 K (calculated per 2 formula units)
2	$[(Fe^{II}I_2)_2 \cdot HATNA]^{\bullet-}$	2	Susceptibility (Sus) and magnetization (Mag) data were fitted separately Sus: J_1 = −400(7) cm^{-1}, J_{MC-MC} = +0.041(2) cm^{-1}, J_{inter} = −0.008(1) cm^{-1}, $g_{(Fe)}$ = 2.211(2), $D_{(Fe)}$ = −9.7(3) cm^{-1} Mag: spin system 1/2 - 7/2 - 7/2 - 1/2 (Fc - MC - MC - Fc) $J_{DmFc-MC}$ = −0.51(5) cm^{-1}, J_{MC-MC} = +0.030(2) cm^{-1}, $g_{(MC)}$ = 2.26(2), $D_{(MC)}$ = −8.2(7) cm^{-1} Θ = +14 K, $\chi_M T$ = 18.59 at 300 K (theoretical for two S = 2 and two S = 1/2 spins (2 units): $\chi_M T$ = 13.5) and 10.06 $\mu_B N_A$ at 50 kOe and 2 K (calculated per 2 formula units)
3	$[(Mn^{II}I_2)_2 \cdot HATNA]^{\bullet-}$	2	J_1 = −300 cm^{-1} (fixed from CASSCF), J_2 = −11(2) cm^{-1} $g_{(Mn)}$ = 2.1102 (fixed from EPR at 5.6 K), J_{inter} = +0.0209(3) cm^{-1}, D = 0 (fixed) Θ = +20 K, $\chi_M T$ = 12.58 at 300 K (theoretical for two S = 5/2 and two S = 1/2 spins: $\chi_M T$ = 9.5) and 10.56 $\mu_B N_A$ at 50 kOe and 2 K
4	$[(Fe^{II}I_2)_3 \cdot HATNA]^{\bullet-}$	3	J_1 = −138.6(4) cm^{-1}, J_2 = −14.49(4) cm^{-1}, $g_{(Fe)}$ = 2.271(4), $D_{(Fe)}$ = −24.8(6) cm^{-1}, J_{inter} = −0.0114(3) cm^{-1} Θ = +11 K, $\chi_M T$ = 10.65 at 300 K (theoretical for three S = 2 and two S = 1/2 spins: $\chi_M T$ = 9.75) and 7.81 $\mu_B N_A$ at 50 kOe and 2 K
5	$[(Fe^{II}I_2)_3 \cdot HAT(CN)_6]^{3\bullet-}$	3	J_1 = −221.6(9) cm^{-1}, J_2 = −17.0(1) cm^{-1}, $g_{(Fe)}$ = 2.100(1), $D_{(Fe1)}$ = +29.0(1) cm^{-1}, $D_{(Fe2)}$ = −28.9(1) cm^{-1} Θ = +26 K, $\chi_M T$ = 12.03 at 300 K (theoretical for three S = 2 and four S = 1/2 spins: $\chi_M T$ = 10.5) and 9.66 $\mu_B N_A$ at 50 kOe and 2 K

DmFc – decamethylferrocenium, MC – molecular complex, $J_{DmFc-MC}$ and J_{MC-MC} denote intermolecular exchange interactions between decamethylferrocenium and molecular complex and between two neighbouring molecular complexes, J_1 and J_2 denote metal-radical and metal-metal exchange interaction values; J_{inter} denotes a general intermolecular exchange value; g is g-factor; D is zero-field splitting parameter.

Complex 1.

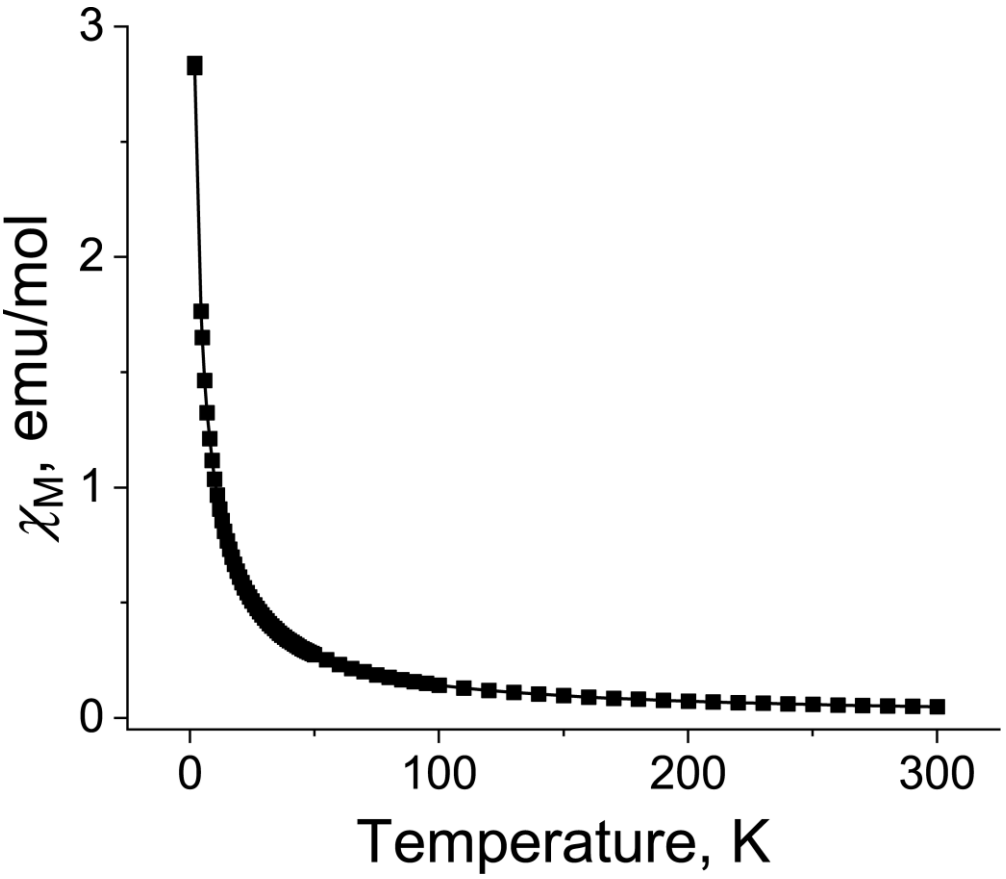

Figure S18. Temperature dependence for molar magnetic susceptibility of polycrystalline $(Cp^*_2Fe^+)[(Co^{II}I_2)_2{\cdot}HATNA]^-{\cdot}2C_6H_4Cl_2{\cdot}0.5C_6H_{14}$ (**1**) in the 1.9-300 K range after the subtraction of temperature independent contribution. Data are calculated per two formula units.

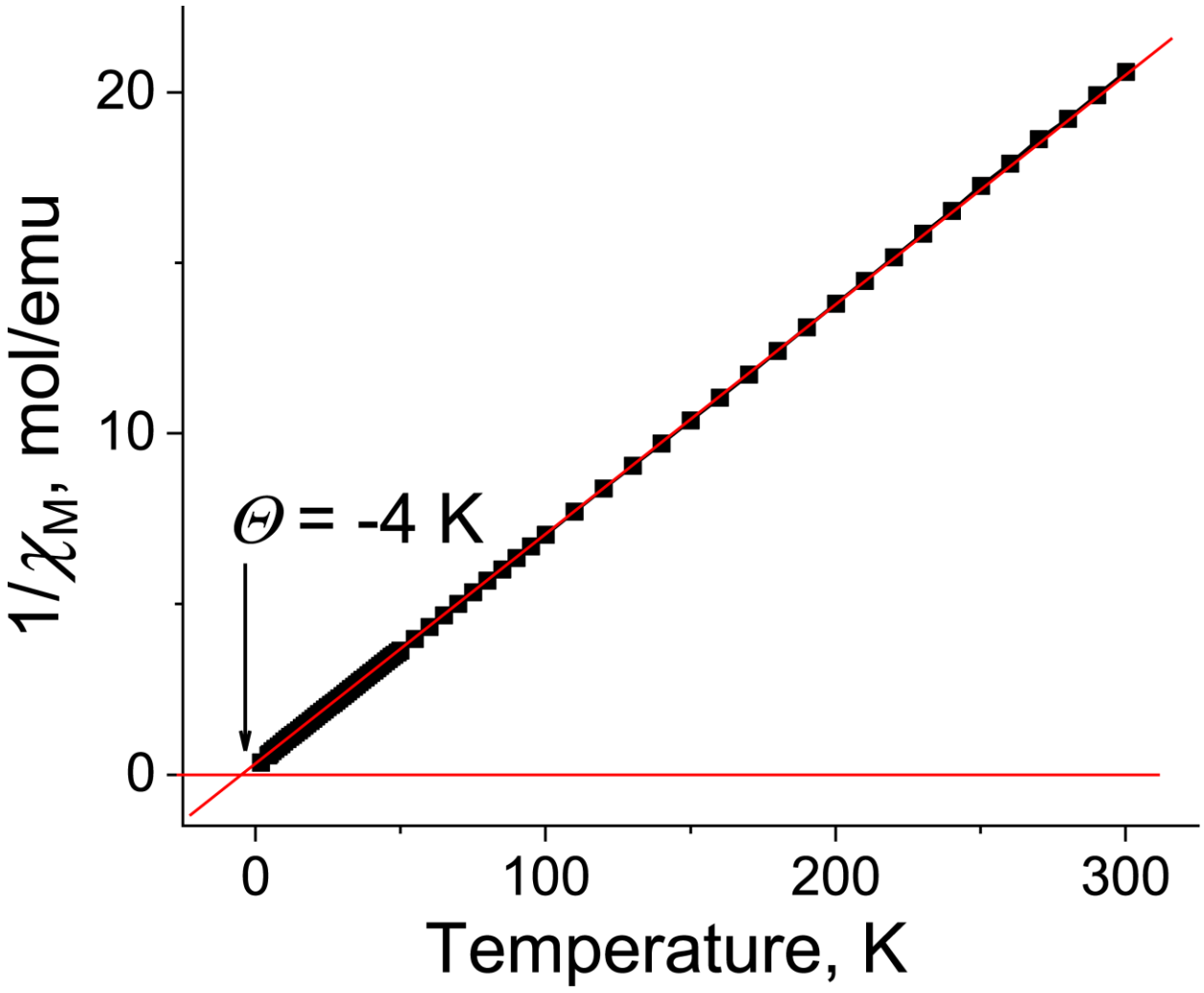

Figure S19. Temperature dependence of reciprocal molar magnetic susceptibility and approximation of the data by the Curie-Weiss law with Weiss temperature (Θ) of –4 K for polycrystalline **1** in the 1.9-300 K range. Data are calculated per two formula units.

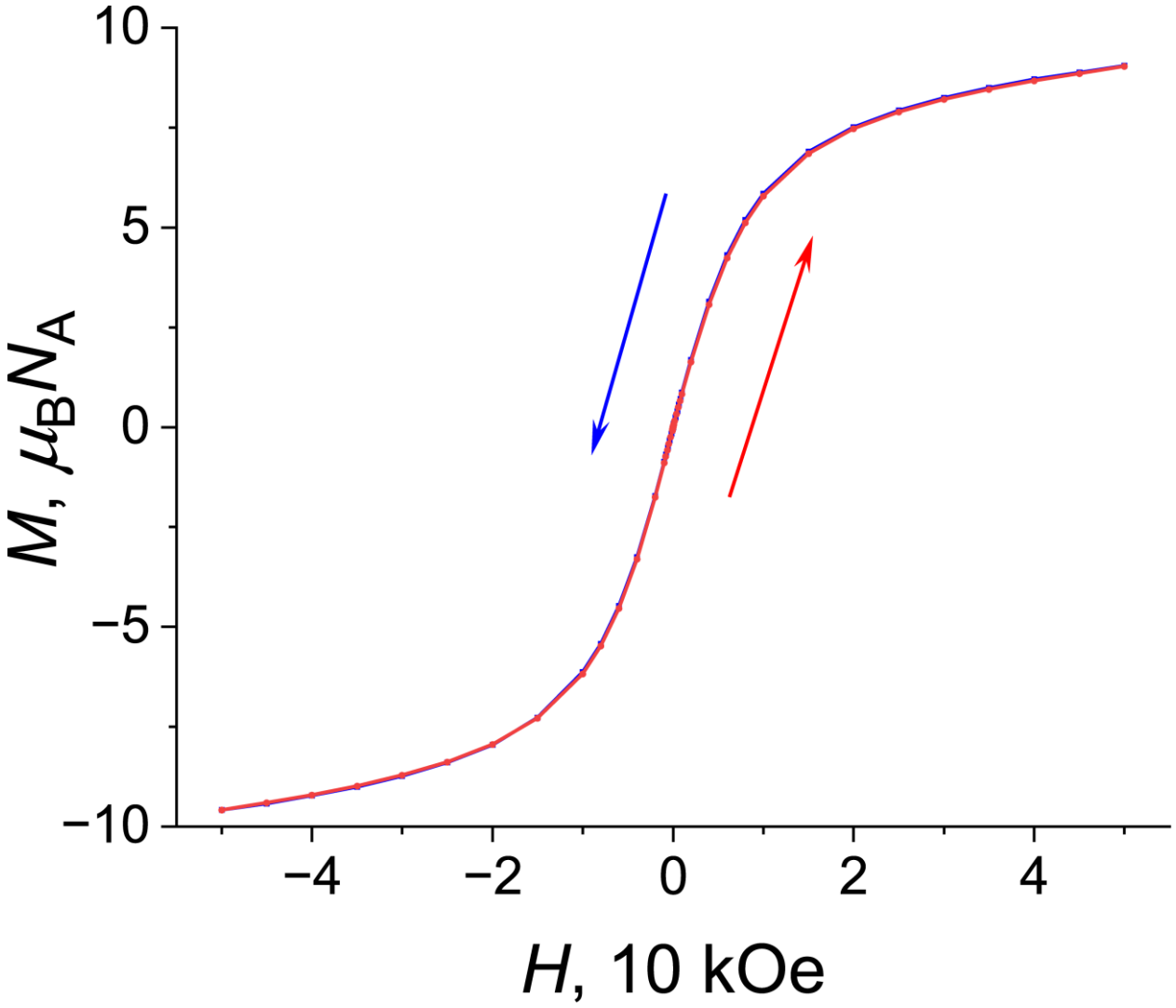

Figure S20. Dependence of magnetization *vs* magnetic field between −50 and 50 kOe (black line is a guide to the eye) for **1 at 2 K**. Data are calculated per two formula units.

Complex 2.

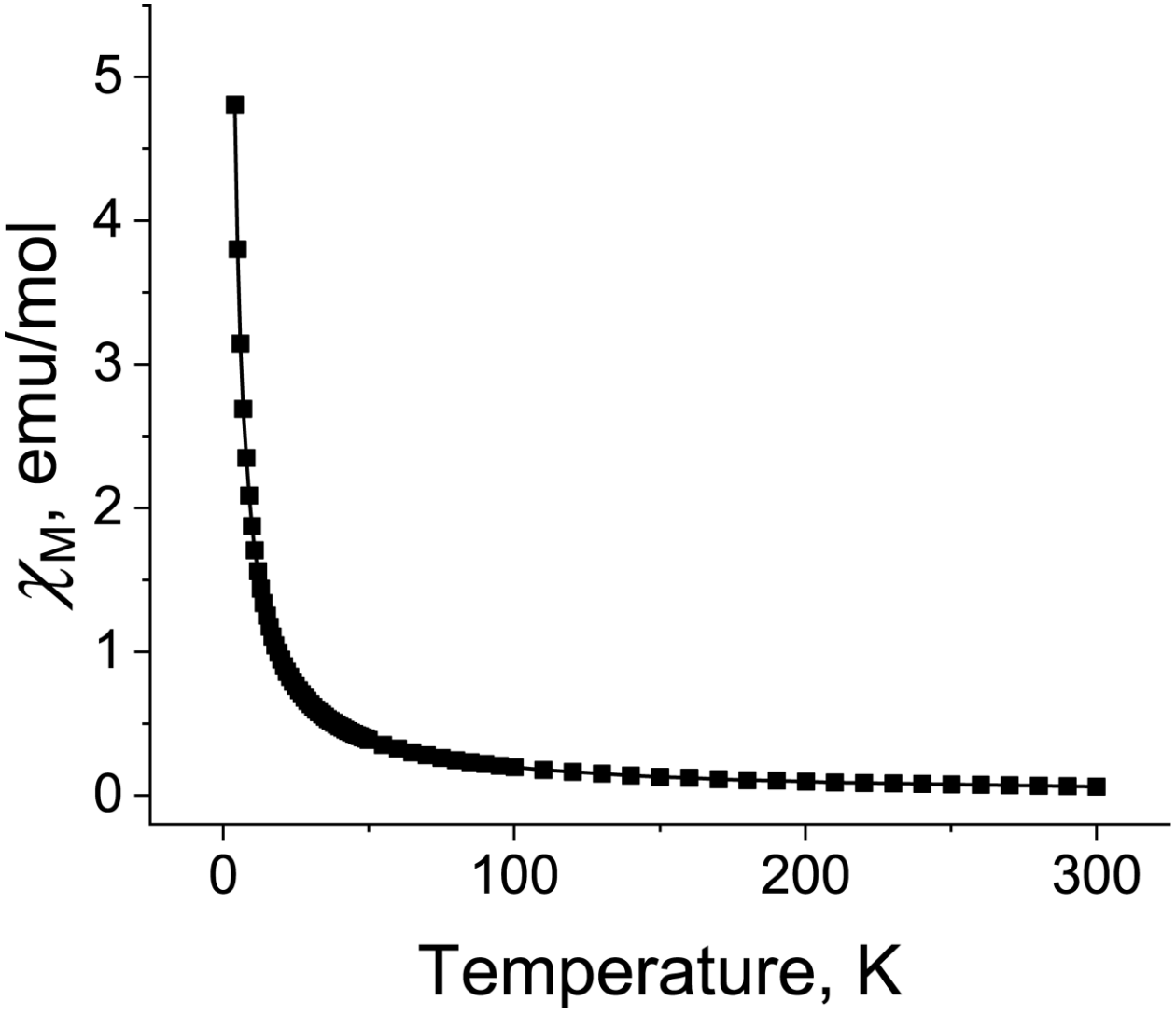

Figure S21. Temperature dependence for molar magnetic susceptibility of polycrystalline $(Cp^*_2Fe^+)[(Fe^{II}I_2)_2{\cdot}HATNA]^-{\cdot}2C_6H_4Cl_2{\cdot}0.5C_6H_{14}$ (**2**) in the 1.9-300 K range after the subtraction of temperature independent contribution. Data are calculated per two formula units.

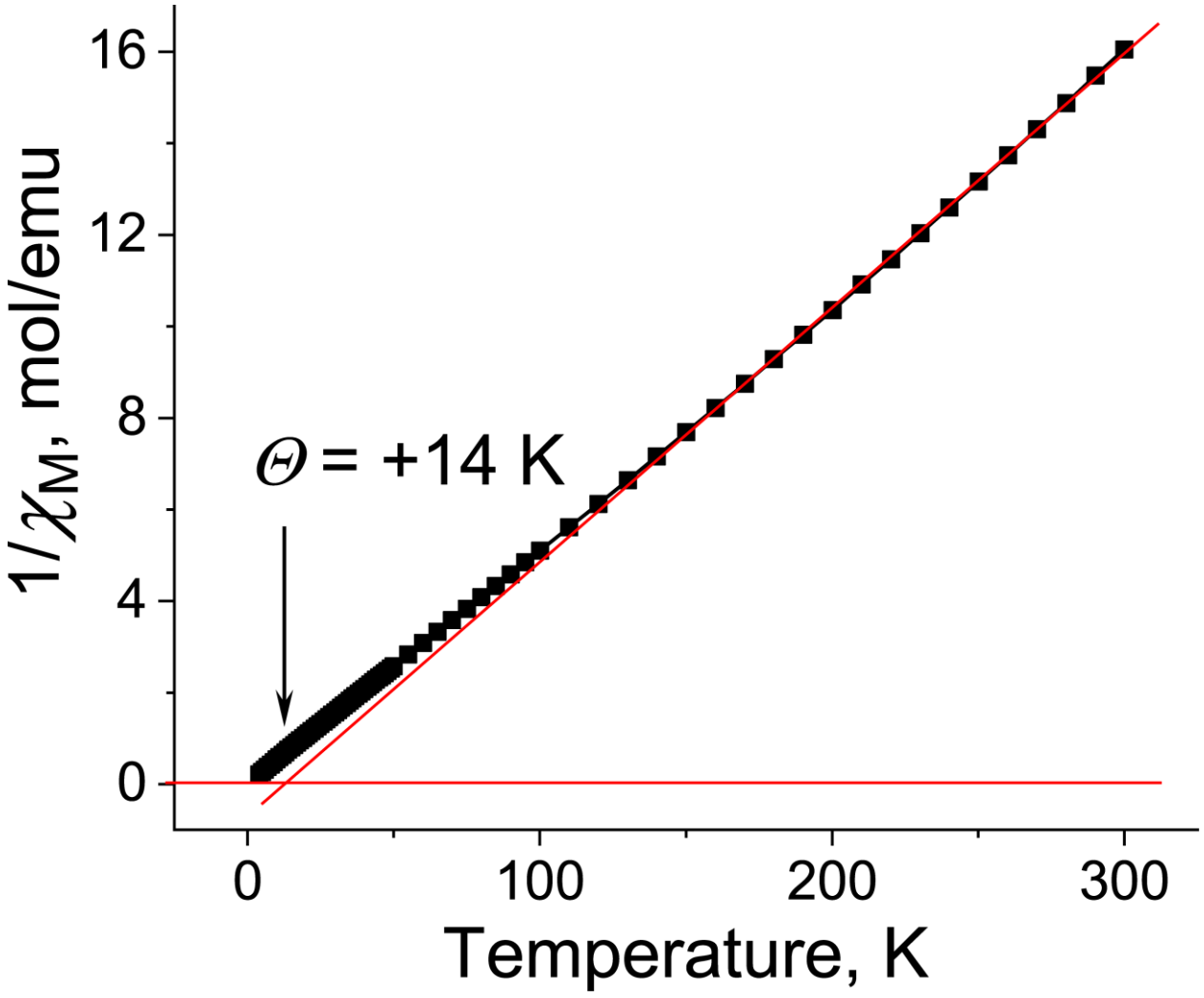

Figure S22. Temperature dependence of reciprocal molar magnetic susceptibility and approximation of the data by the Curie-Weiss law with Weiss temperature (Θ) of +14 K for polycrystalline **2** in the 1.9-300 K range. Data are calculated per two formula units.

Complex 3.

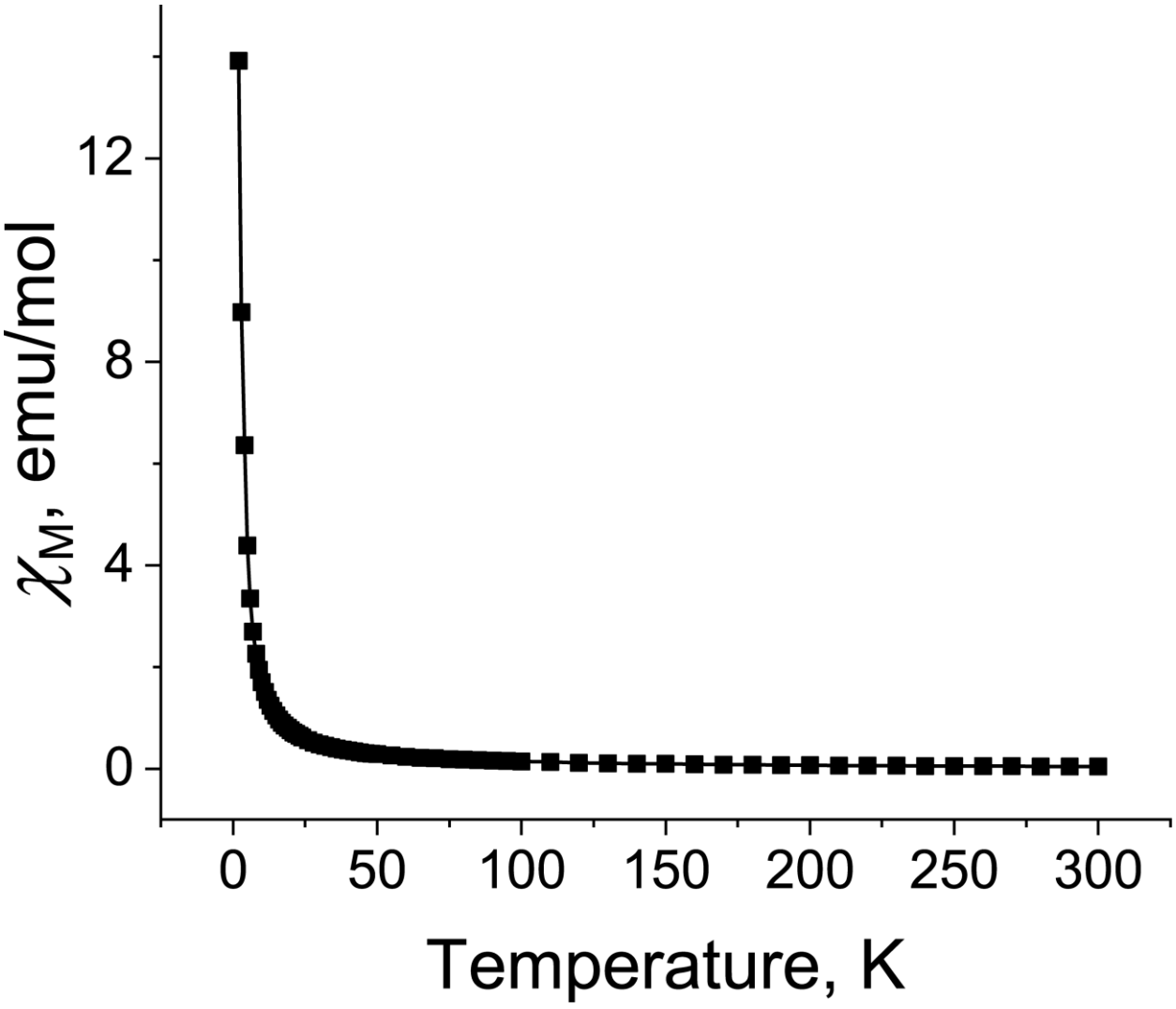

Figure S23. Temperature dependence for molar magnetic susceptibility of polycrystalline $(Cp^*_2Fe^+)[(Mn^{II}I_2)_2{\cdot}HATNA]^-{\cdot}2C_6H_4Cl_2{\cdot}0.5C_6H_{14}$ (**3**) in the 1.9-300 K range after the subtraction of temperature independent contribution. Data are calculated per two formula units.

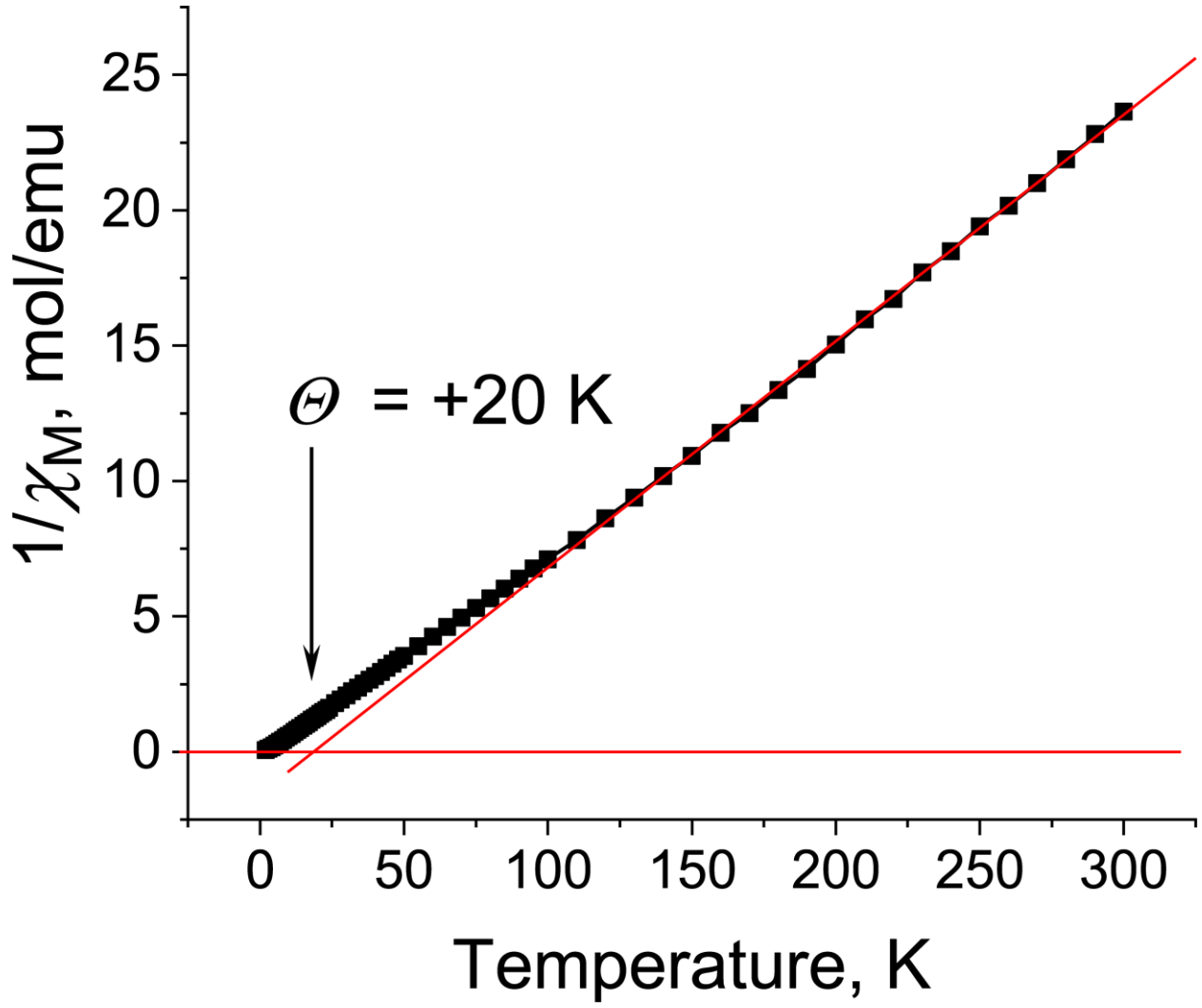

Figure S24. Temperature dependence of reciprocal molar magnetic susceptibility and approximation of the data by the Curie-Weiss law with Weiss temperature (Θ) of +20 K for polycrystalline **3** in the 1.9-300 K range. Data are calculated per two formula units.

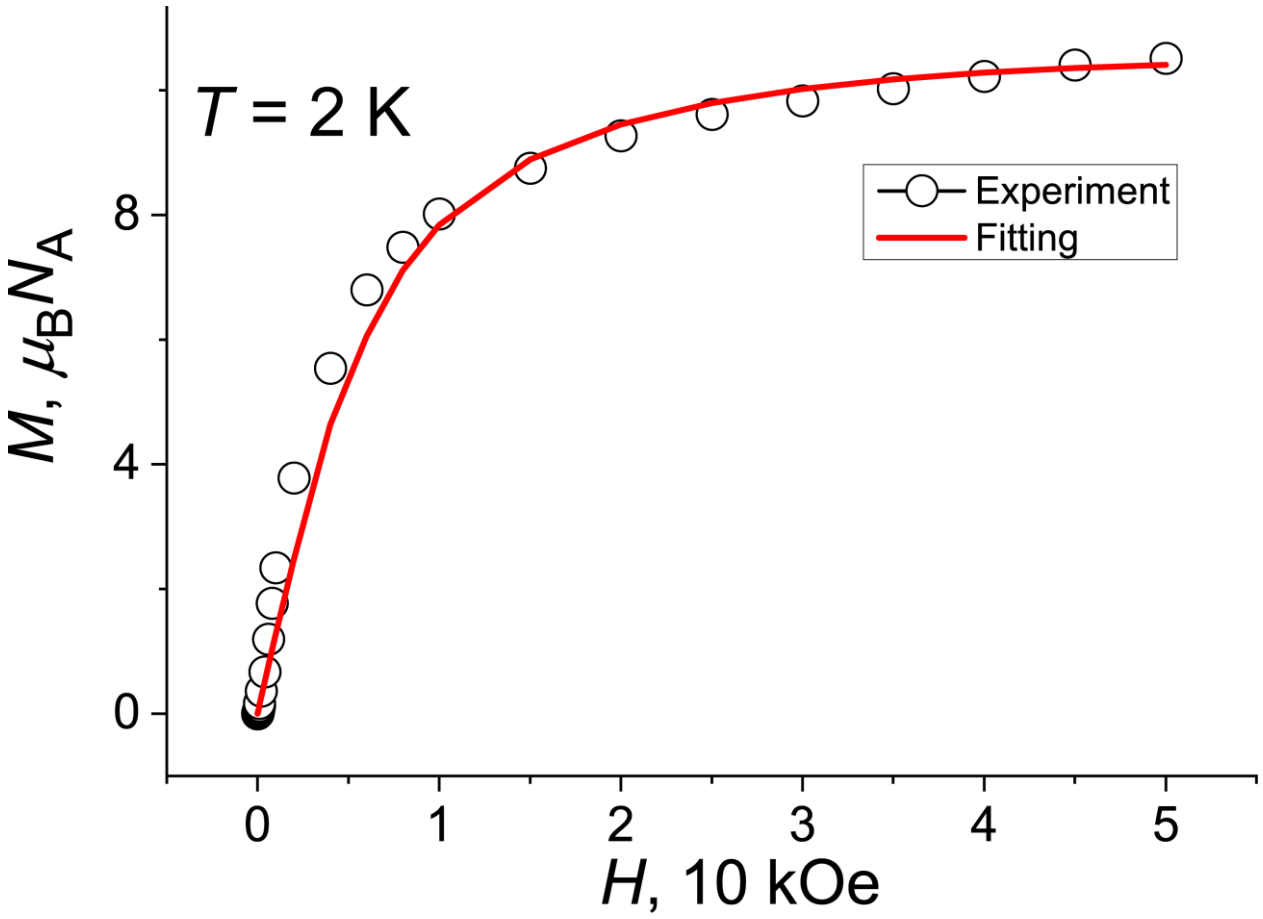

Figure S25. Dependence of magnetization of polycrystalline **3** *vs* magnetic field (black squares) up to 50 kOe magnetic field at 2 K and fitting of the data by PHI [2] (red curve) with the same parameters (simultaneous fitting) as were used for the fitting of temperature dependence of molar magnetic susceptibility (see manuscript).

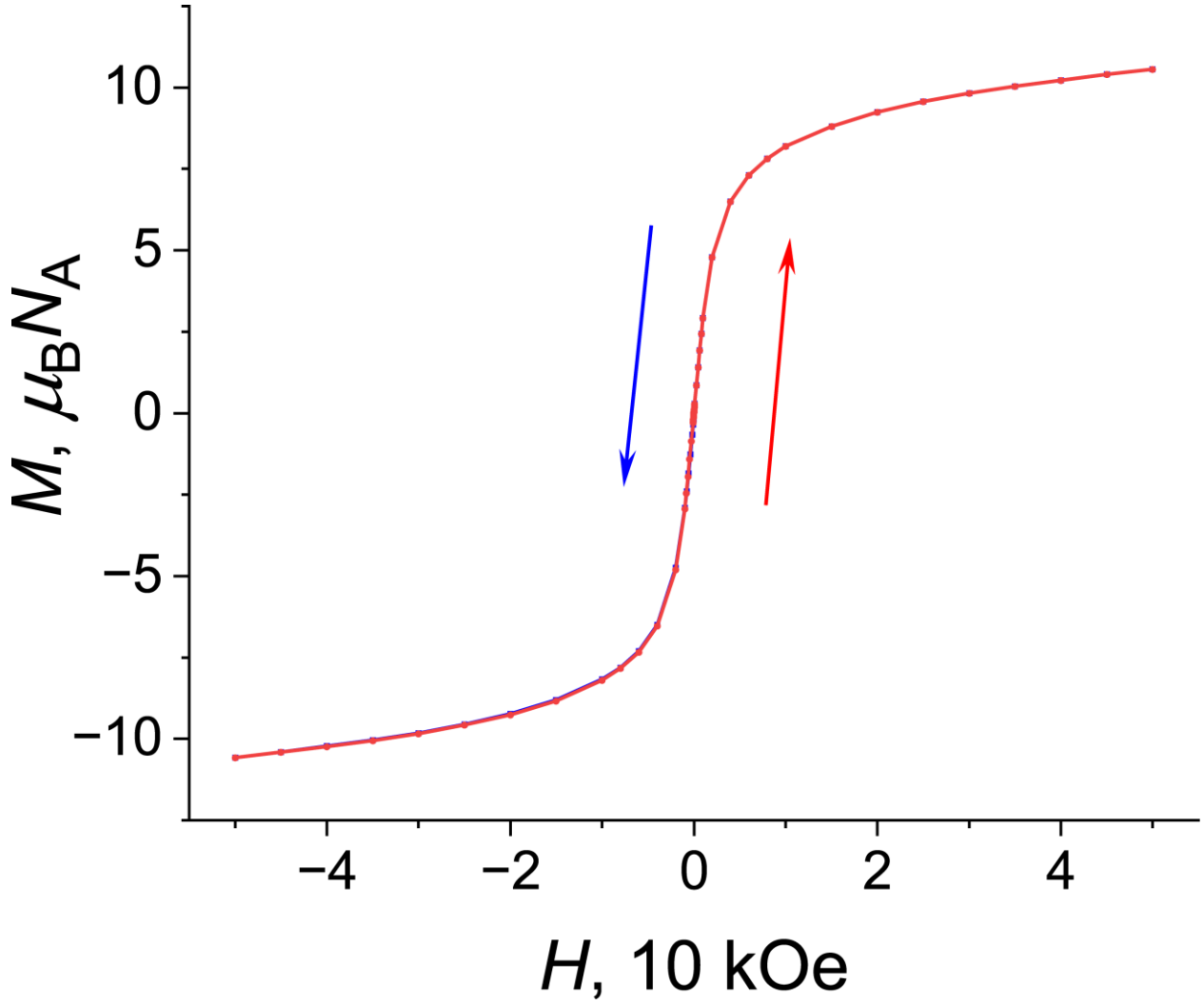

Figure S26. Dependence of magnetization *vs* magnetic field between -50 and 50 kOe (black line is a guide to the eye) for **3** at 2 K. Data are calculated per two formula units.

Complex 4.

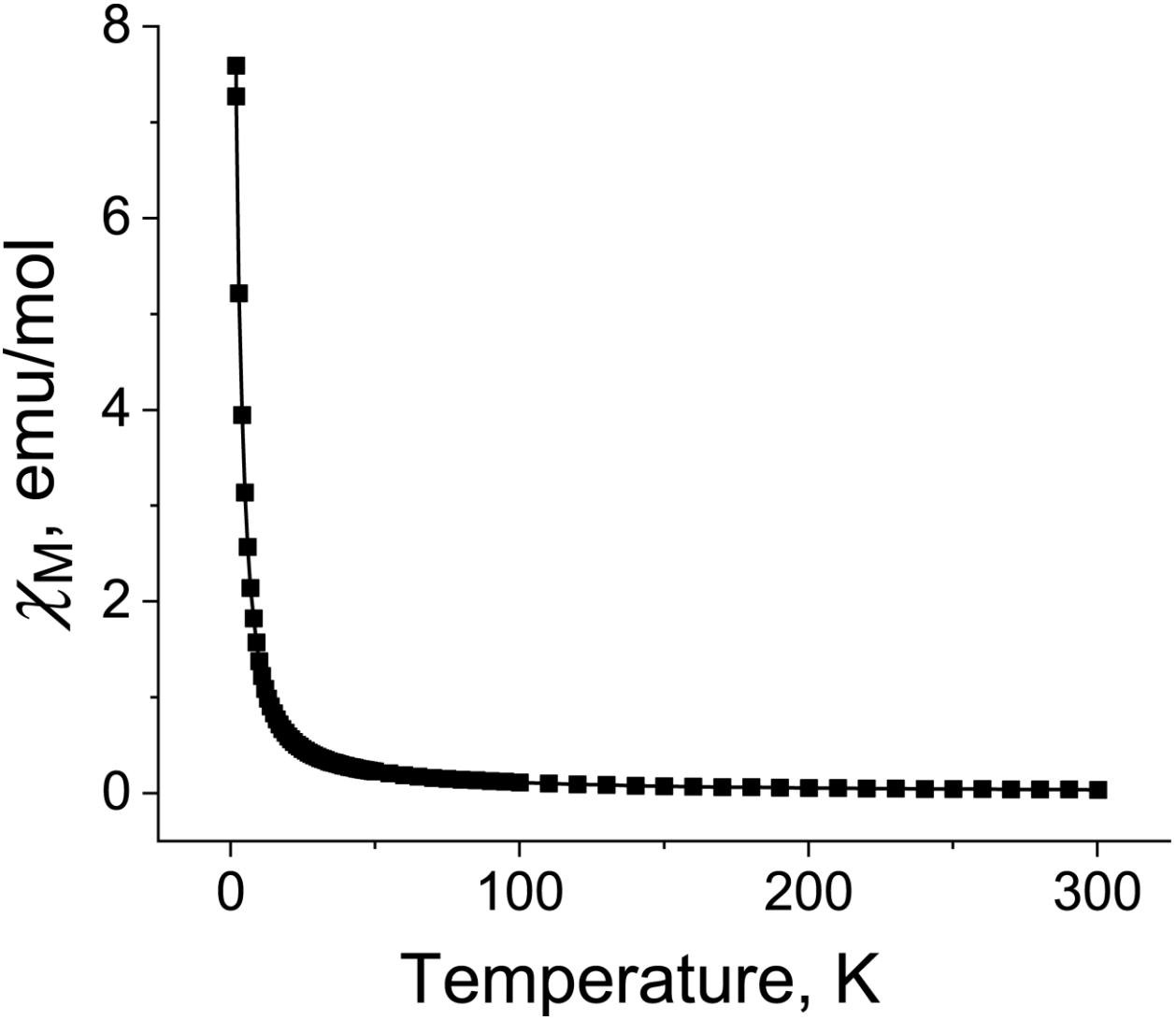

Figure S27. Temperature dependence for molar magnetic susceptibility of polycrystalline $(Cp^*_2Fe^+)[(Fe^{II}I_2)_3{\cdot}HATNA]^-{\cdot}C_6H_4Cl_2$ (**4**) in the 1.9-300 K range after the subtraction of temperature independent contribution.

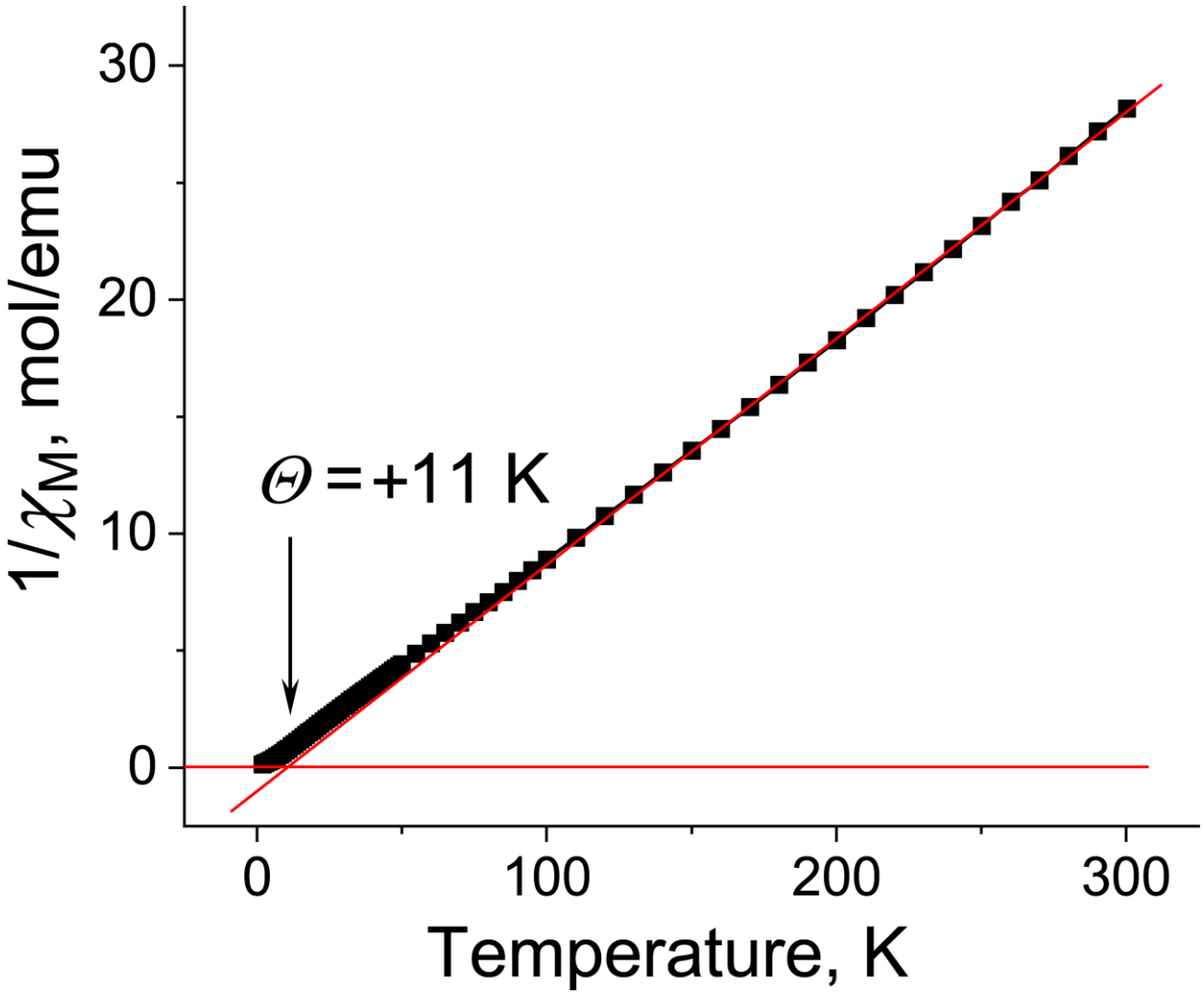

Figure S28. Temperature dependence of reciprocal molar magnetic susceptibility and approximation of the data by the Curie-Weiss law with Weiss temperature (Θ) of +11 K for polycrystalline **4** in the 1.9-300 K range.

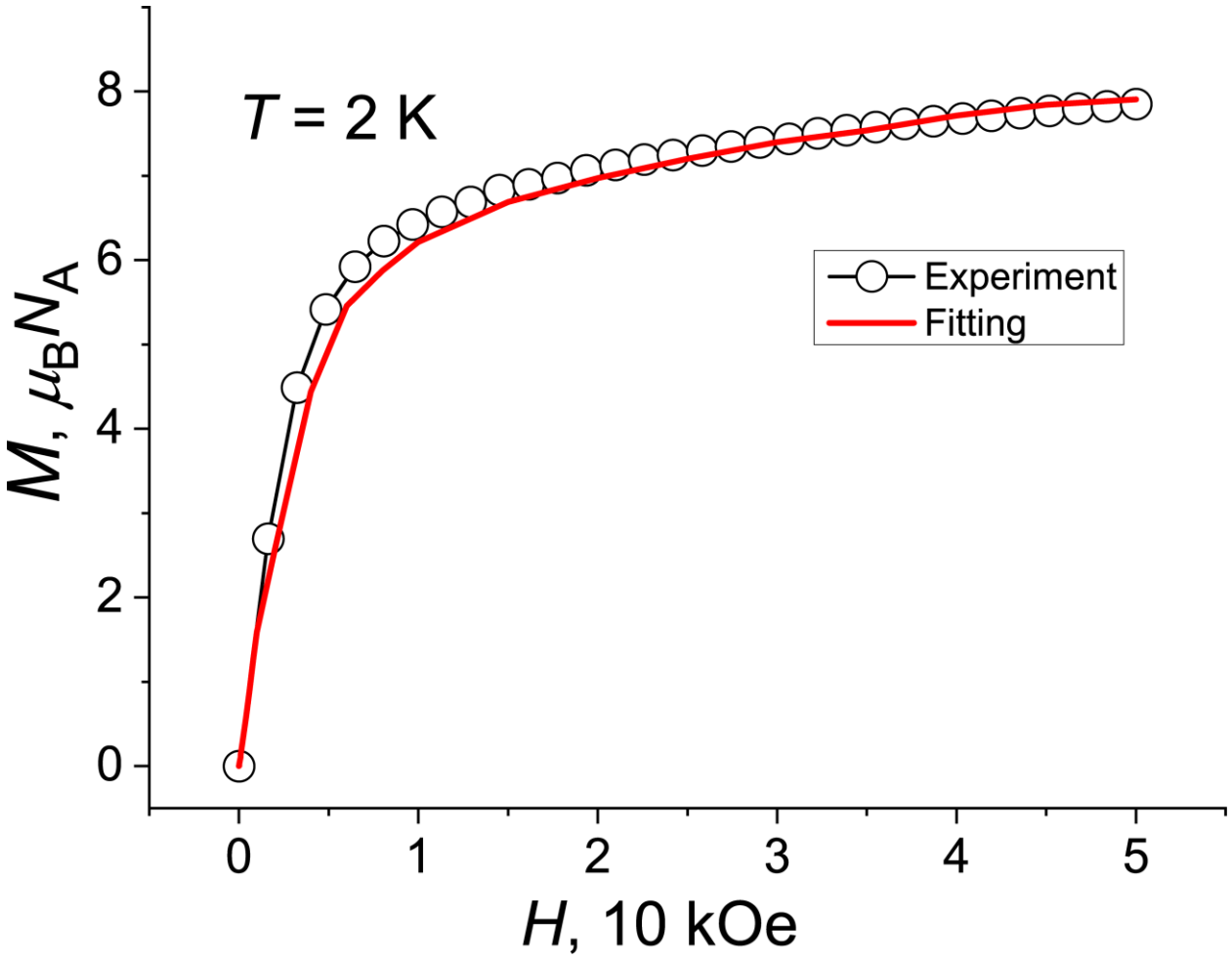

Figure S29. Dependence of magnetization of polycrystalline **4** *vs* magnetic field (black squares) up to 50 kOe magnetic field at 2 K and fitting of the data by PHI [2] (red curve) with the same parameters as were used for the fitting of temperature dependence of molar magnetic susceptibility (see manuscript).

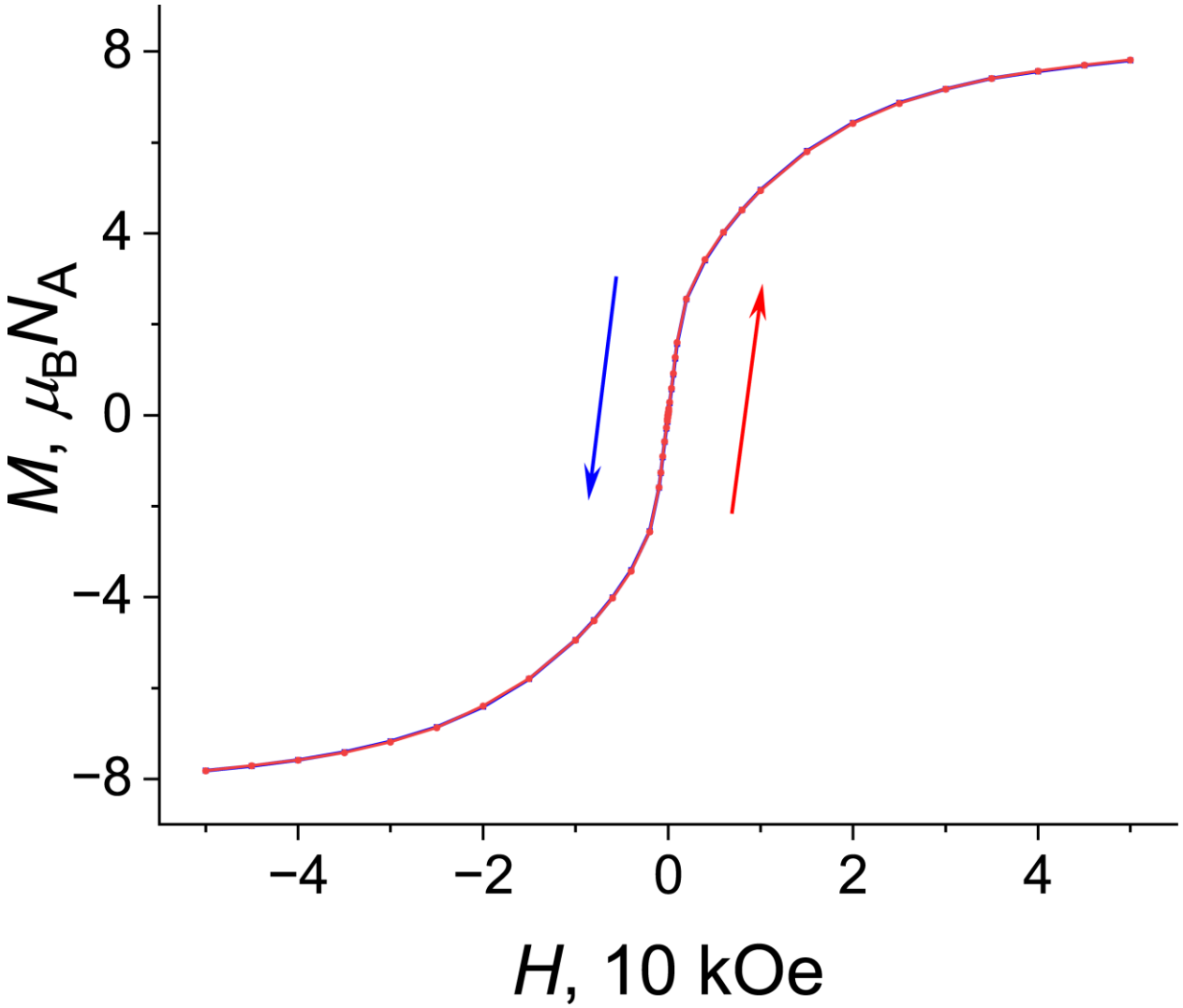

Figure S30. Dependence of magnetization *vs* magnetic field between –50 and 50 kOe (black line is a guide to the eye) for **4** at 2 K.

Complex 5.

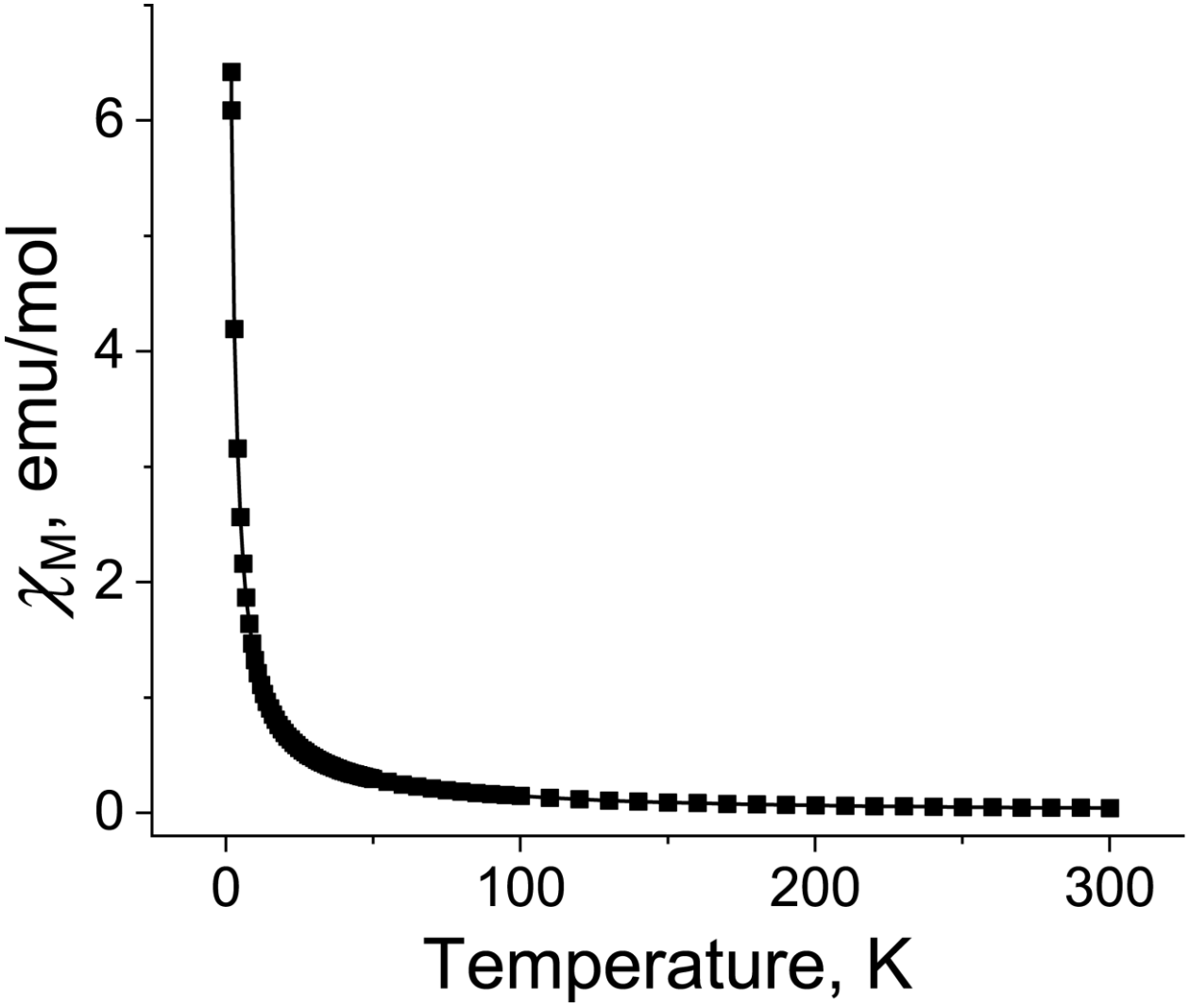

Figure S31. Temperature dependence for molar magnetic susceptibility of polycrystalline $(Cp^*_2Fe^+)_3[(Fe^{II}I_2)_3\ HAT(CN)_6]^{3-}\cdot 4C_6H_4Cl_2$ (**5**) in the 1.9-300 K range after the subtraction of temperature independent contribution.

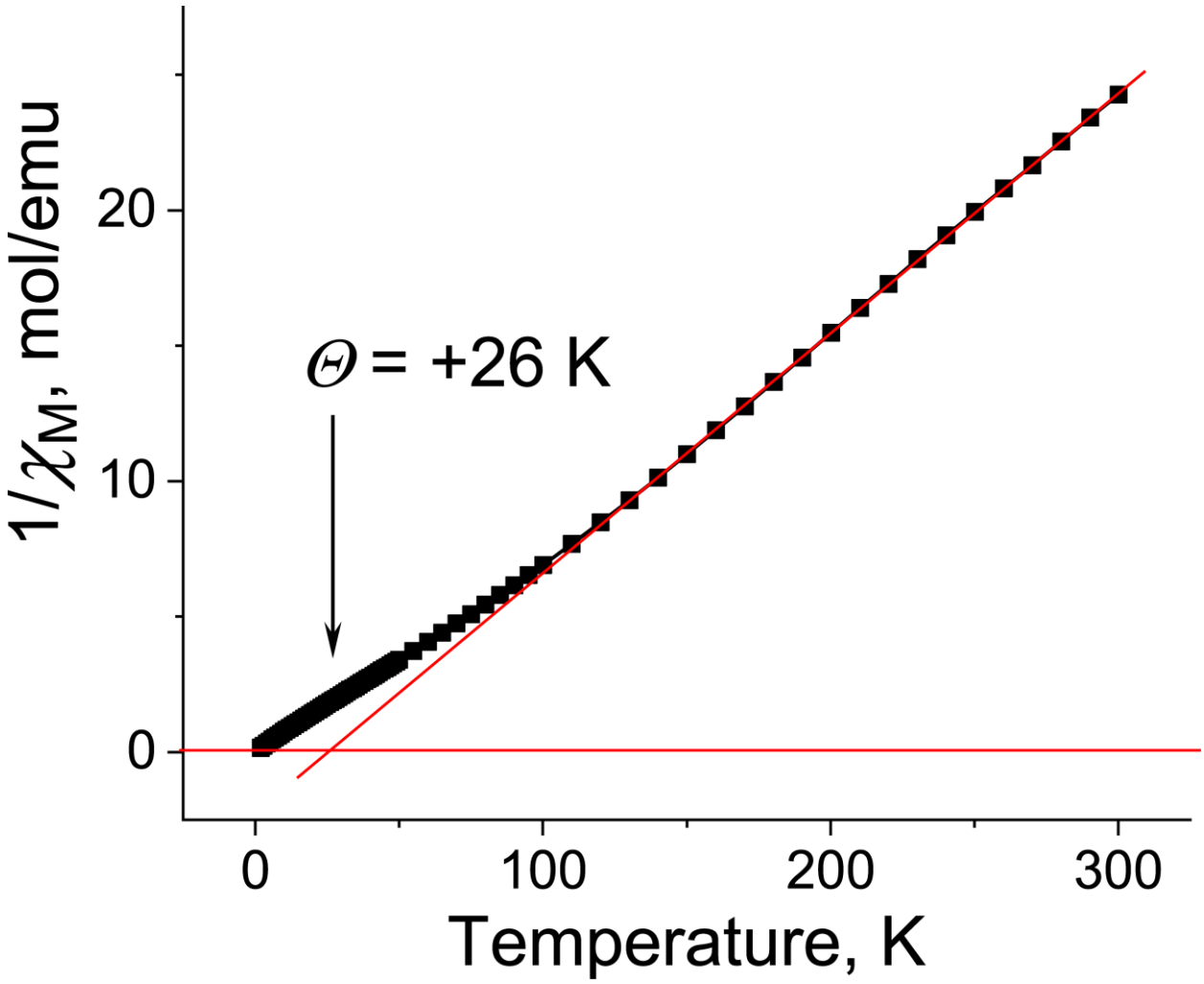

Figure S32. Temperature dependence of reciprocal molar magnetic susceptibility and approximation of the data by the Curie-Weiss law with Weiss temperature (Θ) of +26 K for polycrystalline **5** in the 1.9-300 K range.

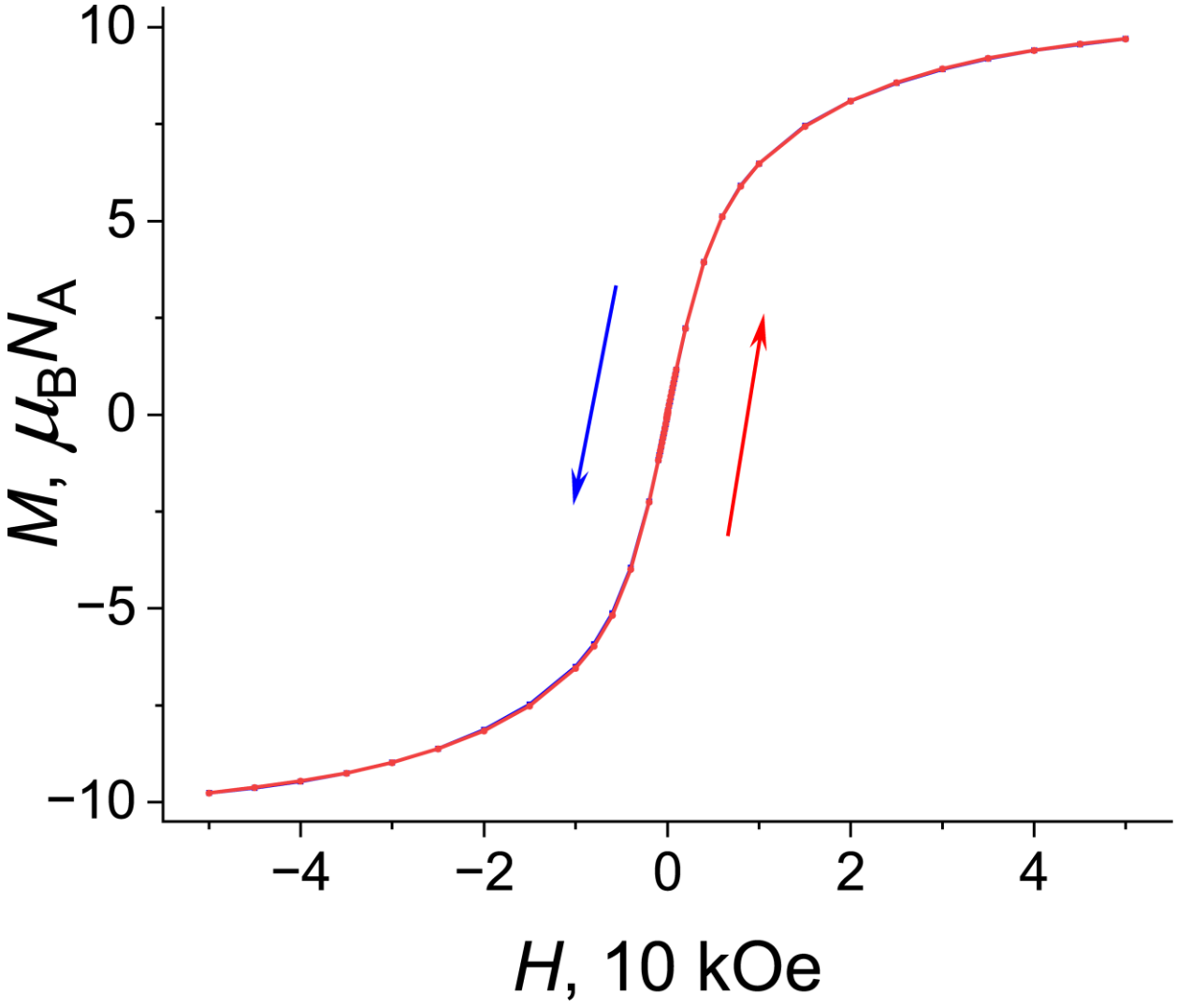

Figure S33. Dependence of magnetization *vs* magnetic field between –50 and 50 kOe (black line is a guide to the eye) for **5** at 2 K.

EPR spectrum of complex 3

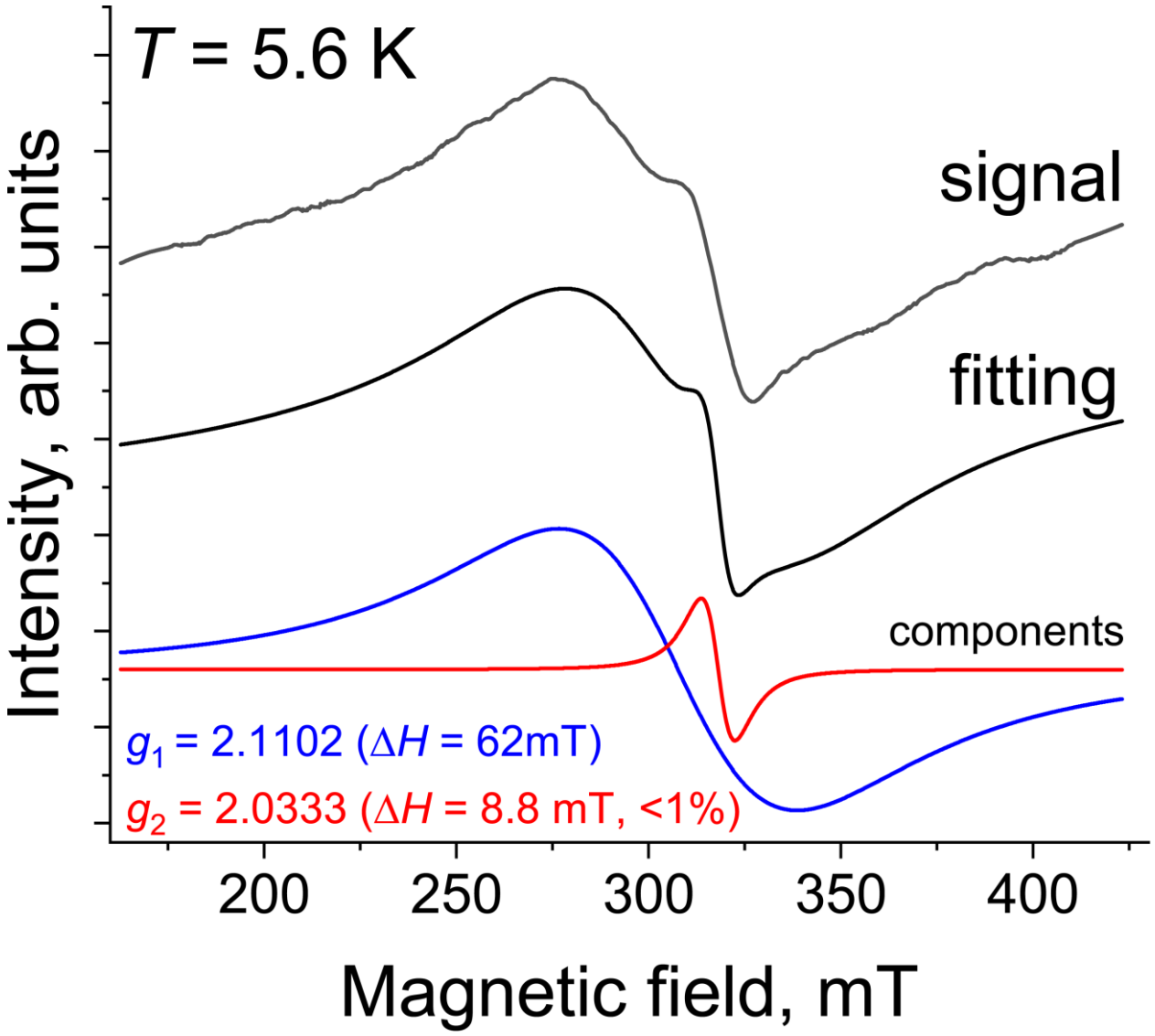

Fig. S34. EPR signal of polycrystalline **3** measured at 5.6 K. Below the spectrum fitting of EPR signal by two Lorentzian lines is shown. Line with g = 2.0333 have integral intensity less than 1% form that of the broader line and it can be attributed to paramagnetic impurity.

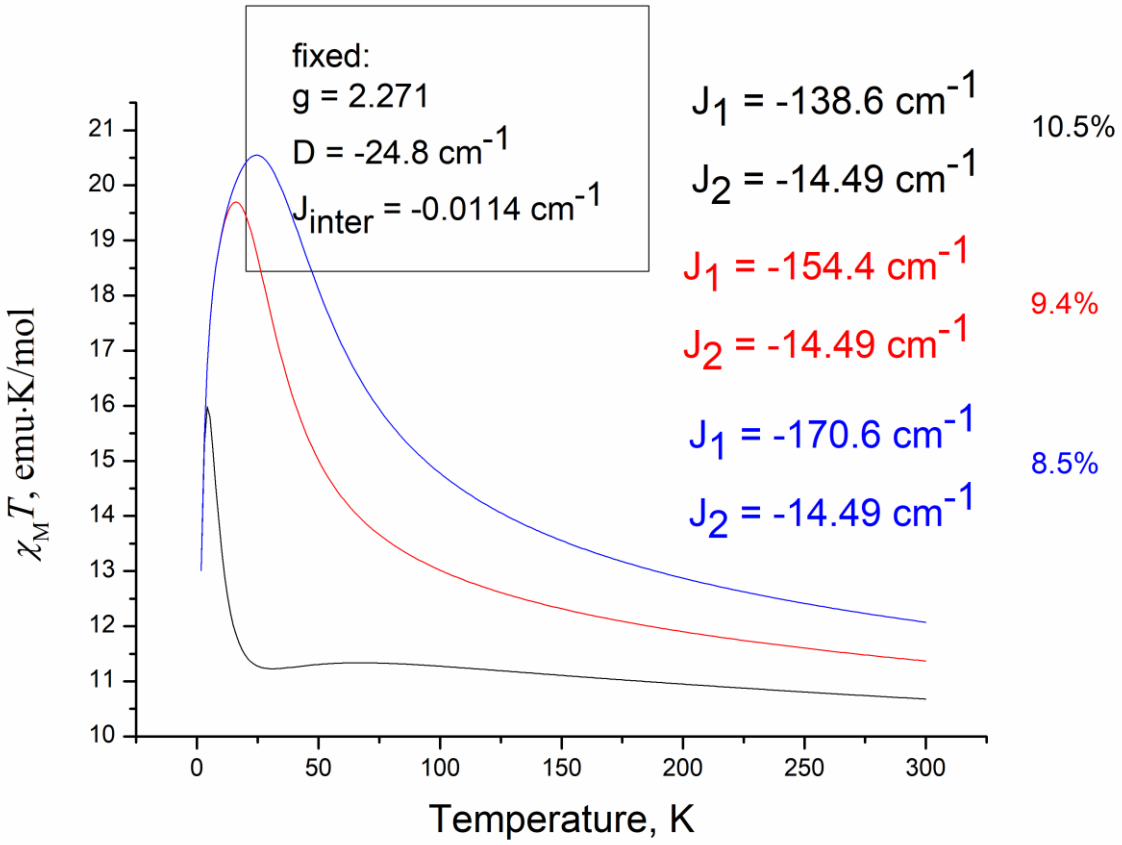

Figure S35. Variation of J_2/J_1 ratio with fixed J_2 for complex **4** towards it decrease (the colors of the value sets match with their curves). The black curve corresponds to the experimental data. While J_2 is fixed, percentages 9.4% and 8.5% were taken as example from J_2/J_1 ratios of previously reported complexes $(CV^{+})_3[(Fe^{II}Cl_2]_3(HAT(CN)_6)]^{3-}\cdot 0.5CVCl\cdot 2.5C_6H_4Cl_2$ [3] and $[(K^{+})(crypt)]_3[(Fe^{II}I_2]_3(HATNA(CN)_6)]^{3-}\cdot 2C_6H_4Cl_2$ [4].

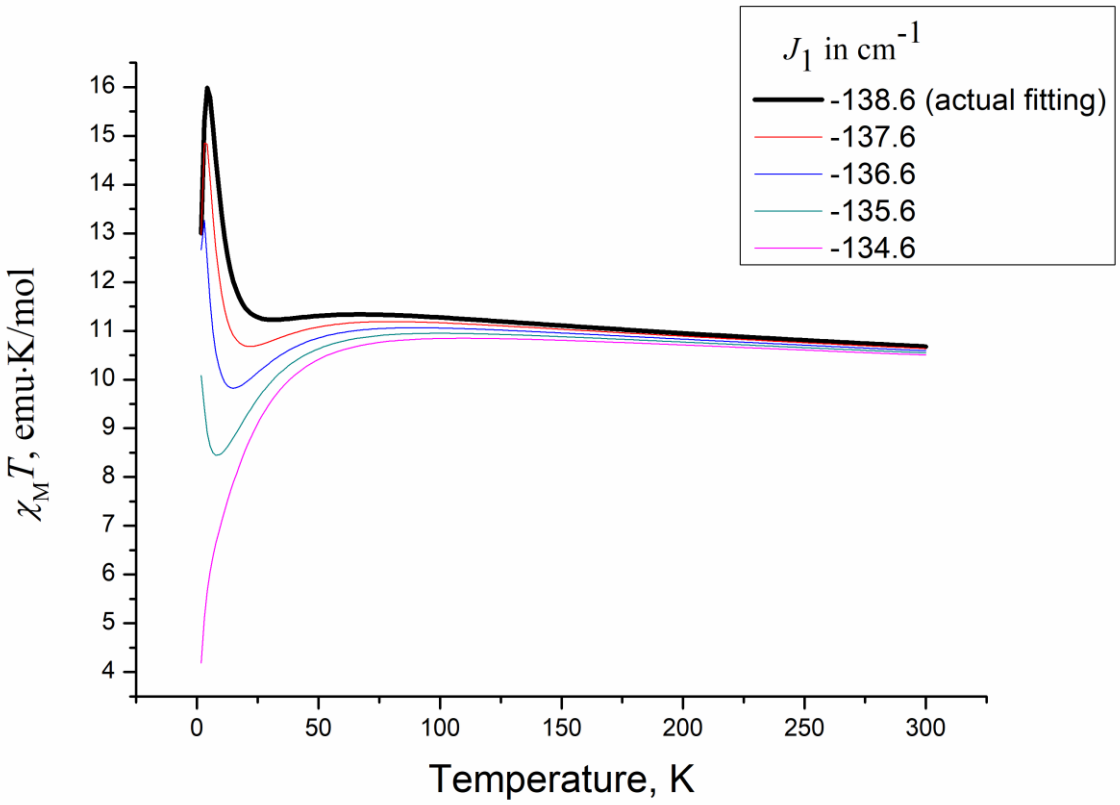

Figure S36. Variation of J_2/J_1 ratio with fixed J_2 for complex **4** towards it increase (from black to purple line). The black curve corresponds to the experimental data.

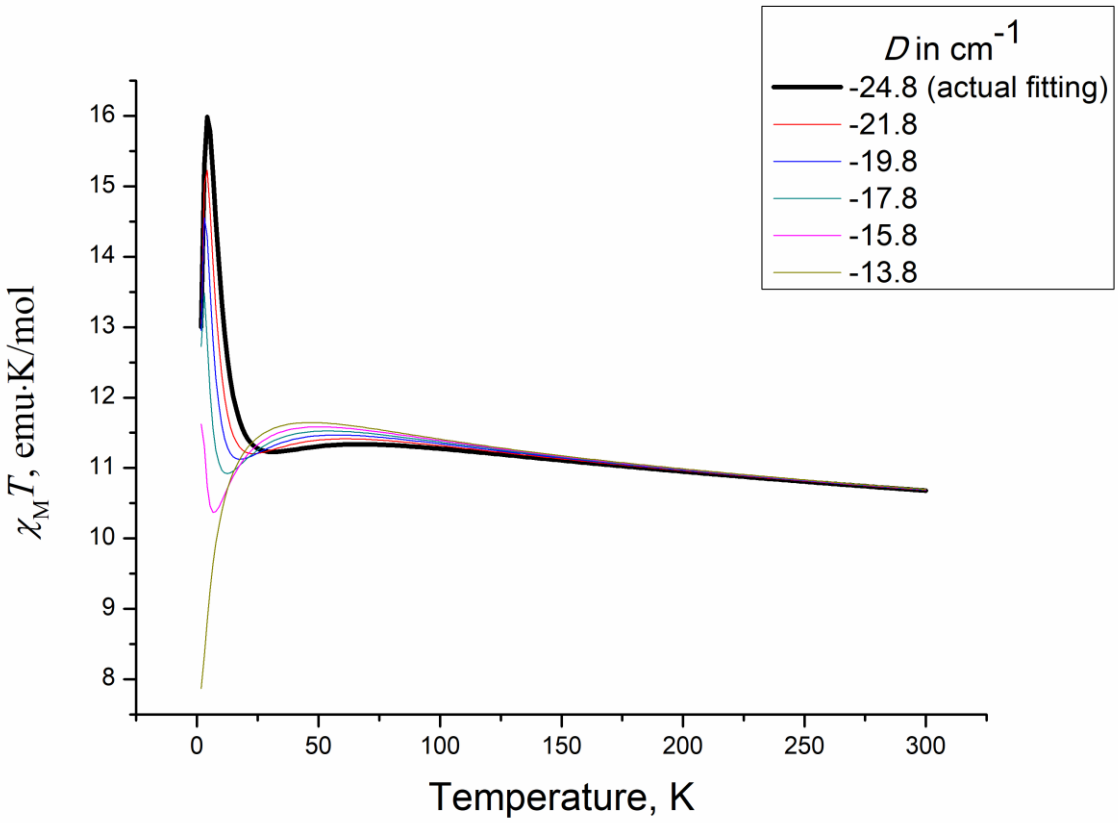

Figure S37. Variation of *D* value for complex **4**. The black curve corresponds to the experimental data.

Computational details

All calculations were performed in ORCA 6.1.1 software [5]. XYZ coordinates of all complexes were taken from X-ray crystal structures data with optimization of only hydrogen atom positions at the DFT level with B3LYP functional [6]. In all calculations, the x2c-TZVPall [7] basis set was used for all atoms, except for the d-elements, for which the x2c-QZVPall [7] basis set was used. The RIJCOSX approximation [8] in combination with AUTOAUX auxiliary basis [9] was used to accelerate calculations. Scalar relativistic effects were taken into account through the „Exact 2 component“ (X2C) Hamiltonian [10]. The X2C method is implemented in ORCA only as effective one-component method. All calculations were performed in conductive media taken into account in CPCM model ($\varepsilon = \infty$) as an approximation to a polar crystalline medium.

Single-point DFT broken symmetry (BS) calculations [11] were performed in GGA BP86 [12] and hybrid B3LYP functionals.

The multireference complete active space self-consistent field calculations (CASSCF [13]) were performed for all complexes.

The initial orbitals for the CASSCF calculations were taken from preliminary DFT calculations. For binuclear complexes, the state-average SA-CASSCF/NEVPT2 calculation was performed considering fifteen electrons (complex **1**), thirteen electrons (complex **2**) and eleven electrons (complex **3**) electrons on 10d and 1p orbitals, i.e., using the CAS(n, 11) active space, where n = 15, 13, and 11, respectively. For trinuclear complex **4**, calculation was performed considering nineteen electrons on 15d and 1p orbitals, i.e. using the CAS(19, 16) active space. In these active spaces, we calculated 10 roots for each multiplicity for all complexes, with the

exception case for multiplicity 12 of complex **3**, in which one root was calculated. In case of large active space (complex **4**), large-scale approximation CASSCF (ICE-SCF) and FIC-NEVPT2 was used [14].

The local magnetic properties (the axial zero field splitting (ZFS) parameters (D), rhombicity ratio in the ZFS (E/D), g-factor) were obtained from SA-CASSCF/NEVPT2 calculations with the spin–orbit coupling (SOC) Hamiltonian for mononuclear complexes, where one (complexes **1**, **2**, **3**) or two (complexes **4**, **5**) paramagnetic ions were replaced by diamagnetic ion Zn(II). The SOC calculation was done in the Breit-Pauli form of the SOC operator (SOMF(1X) approximation [15] for all roots according to quasi-degenerate perturbation theory (QDPT) [16]. Seven electrons on five active d-orbitals were used in calculation for Co(II) mononuclear paramagnetic fragment, all 10 quartet and 40 doublet roots were taken with equal weights. Six electrons on five active d-orbitals were used in calculation for Fe(II) mononuclear paramagnetic fragment, all 5 quintet, 45 triplet and 50 singlet roots were taken with the equal weights. Five electrons on five active d-orbitals were used in calculation for Mn(II) mononuclear paramagnetic fragment, all 1 sextet, 24 quartet and 75 doublet roots were taken with the equal weights. ORCA POLY_ANISO module was used to obtain the $\chi_M T$ dependences on the basis of the calculated local magnetic properties of auxiliary mononuclear paramagnetic fragments. Splitting of the d-orbitals was analyzed within the ab initio ligand field theory (AILFT) [17, 18].

Magnetic exchange interaction calculation

The magnetic exchange interaction was described by the Heisenberg spin Hamiltonian, which has the following form for *N+1* magnetic centers with *N* metal atoms M (M is Co(II), Fe(II) or Mn(II)) and one ligand L:

$$\hat{H} = -2\sum_{i=1}^{N} J_i \hat{S}_{M_i} \hat{S}_L - 2\sum_{i<j} J_{ij} \hat{S}_{M_i} \hat{S}_{M_j} \quad (1)$$

Here the first sum is over the metal magnetic centers and describes the exchange interaction between metal atoms and the ligand; the second sum is over all metal atoms pairs and describes the exchange interaction between metal atoms. In (1), J_i is the effective exchange interaction between *i*-th metal atom and the ligand, J_{ij} is the effective exchange interaction between *i*-th and *j*-th metal atoms, $\hat{S}_a$ is the total spin operator of the magnetic center *a* (*a* is one of metal atoms or the ligand).

In the case of two magnetic centers *a* and *b*, the Yamaguchi's approximate spin projection procedure (AP) [19] results in the following expression:

$$J_{ab}^{(AP)} = -\frac{E_{HS} - E_{LS}}{\langle S^2 \rangle_{HS} - \langle S^2 \rangle_{LS}} \quad (2)$$

E_{HS} and $<S^2>_{HS}$ and E_{LS} and $<S^2>_{LS}$ are the energy and the expectation value of the squared spin operator for high-spin and low-spin states, respectively. The generalization of AP approach to multispin systems was done in Ref. [20].

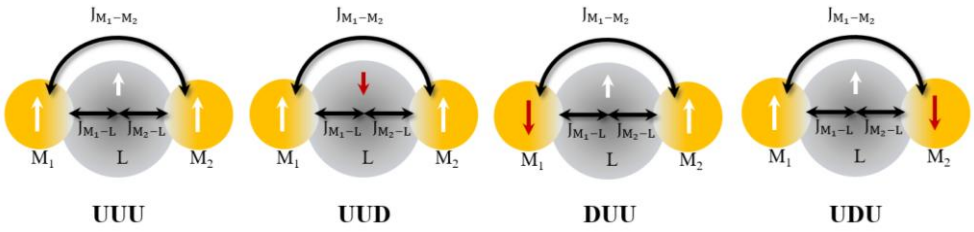

Figure S38. Calculated solutions for two-metals complexes M_1-M_2-L: UUU - all spins up; UUD – one spin down on the ligand; DUU, UDU – one spin down on one metal atom.

In the case of three magnetic centers for two-metal complexes **1** (Co(II)-Co(II)-L), **2** (Fe(II)-Fe(II)-L) and **3** (Mn(II)-Mn(II)-L), four solutions were calculated to get J_1 and J_2 values. These

solutions were “UUU”, “UUD”, “DUU” and “UDU”, where U (up) and D (down) denote the spin orientation at the M_1, M_2 and L magnetic centers (see Fig. S38). Both broken-symmetry (BS-DFT) and SA-CASSCF/NEVPT2 calculations yielded the "UUD" solution as the ground state for all two-metals complexes **1**, **2** and **3**.

The generalization of AP approach to multi-spin systems [20] resulted in the following expression for J_1 and J_2 for M_1-M_2-L systems with different metal atoms:

$$J_{M1\text{-}L} = -\frac{E_{UUU} - E_{UUD} + E_{UDU} - E_{DUU}}{\langle S^2\rangle_{UUU} - \langle S^2\rangle_{UUD} + \langle S^2\rangle_{UDU} - \langle S^2\rangle_{DUU}} \quad (3)$$

$$J_{M2\text{-}L} = -\frac{E_{UUU} - E_{UUD} - E_{UDU} + E_{DUU}}{\langle S^2\rangle_{UUU} - \langle S^2\rangle_{UUD} - \langle S^2\rangle_{UDU} + \langle S^2\rangle_{DUU}} \quad (4)$$

$$J_{M1\text{-}M2} = -\frac{E_{UUU} + E_{UUD} - E_{UDU} - E_{DUU}}{\langle S^2\rangle_{UUU} + \langle S^2\rangle_{UUD} - \langle S^2\rangle_{UDU} - \langle S^2\rangle_{DUU}} \quad (5)$$

For complexes **1**, **2**, **3** the metal atoms were assumed to be equivalent, and the exchange interaction was described by two parameters J_1 and J_2, where the metal-ligand exchange parameter J_1 and the metal – metal exchange parameter J_2. The parameters were calculated as the following:

$$J_1 = \frac{1}{2}\left(J_{M1\text{-}L} + J_{M2\text{-}L}\right) \quad (6)$$

$$J_2 = J_{M1\text{-}M2} \quad (7)$$

For complexes **1**, **2**, **3** with two equivalent metal atoms, it is sufficient to calculate three different states “UUU”, “UUD”, “UDU” (as “UDU” and “DUU” are treated as similar states). In this case, the following simplified expressions for J_1 and J_2 are available

$$J_1 = -\frac{E_{UUU} - E_{UUD}}{\langle S^2\rangle_{UUU} - \langle S^2\rangle_{UUD}} \quad (8)$$

$$J_2 = -\frac{E_{UUU} + E_{UUD} - 2E_{UDU}}{\langle S^2\rangle_{UUU} + \langle S^2\rangle_{UUD} - 2\langle S^2\rangle_{UDU}} \quad (9)$$

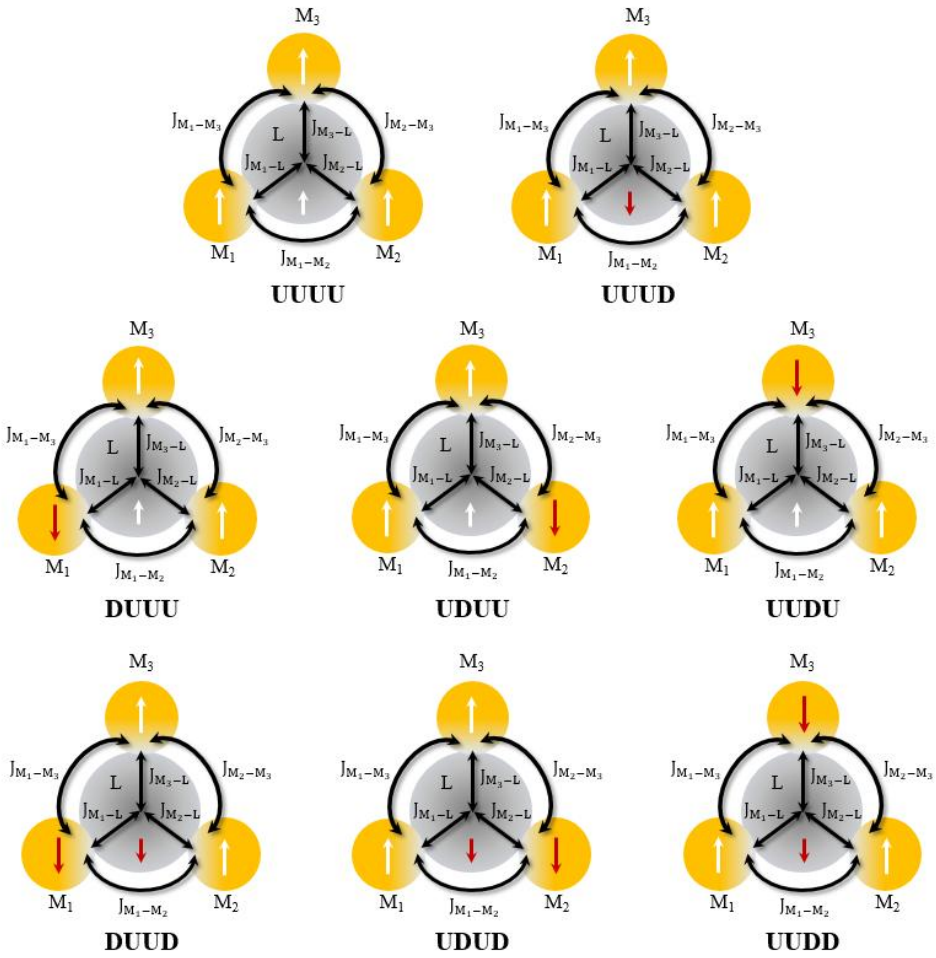

Figure S39. Calculated solutions for three-metals complexes M_1-M_2-M_3-L: UUUU – all spins up; UUUD – one spin down on the ligand; DUDU, UDUU UUDU – one spin down on the first, second and third metal; DUUD – two spins down on the first metal and on the ligand; UDUD – two spins down on the second metal and on the ligand; UUDD – two spins down on the third metal and on the ligand.

In the case of four magnetic center of a three-metals systems like M_1-M_2-M_3-L (complexes **4** and **5**), eight solutions were calculated: UUUU, UUUD, DUUU, UDUU, UUDU, DUUD,

UDUD and UUDD (see Fig. S39). Both BS-DFT and SA-CASSCF/NEVPT2 calculations yielded the "UUUD" solution to be the ground state for both complexes **4** and **5**.

$$J_{\text{M1-L}} = -\frac{E_{\text{UUUU}} - E_{\text{UUUD}} - E_{\text{DUUU}} + E_{\text{UDUU}} + E_{\text{UUDU}} + E_{\text{DUUD}} - E_{\text{UDUD}} - E_{\text{UUDD}}}{\langle S^2\rangle_{\text{UUUU}} - \langle S^2\rangle_{\text{UUUD}} - \langle S^2\rangle_{\text{DUUU}} + \langle S^2\rangle_{\text{UDUU}} + \langle S^2\rangle_{\text{UUDU}} + \langle S^2\rangle_{\text{DUUD}} - \langle S^2\rangle_{\text{UDUD}} - \langle S^2\rangle_{\text{UUDD}}} \quad (10)$$

$$J_{\text{M2-L}} = -\frac{E_{\text{UUUU}} - E_{\text{UUUD}} + E_{\text{DUUU}} - E_{\text{UDUU}} + E_{\text{UUDU}} - E_{\text{DUUD}} + E_{\text{UDUD}} - E_{\text{UUDD}}}{\langle S^2\rangle_{\text{UUUU}} - \langle S^2\rangle_{\text{UUUD}} + \langle S^2\rangle_{\text{DUUU}} - \langle S^2\rangle_{\text{UDUU}} + \langle S^2\rangle_{\text{UUDU}} - \langle S^2\rangle_{\text{DUUD}} + \langle S^2\rangle_{\text{UDUD}} - \langle S^2\rangle_{\text{UUDD}}} \quad (11)$$

$$J_{\text{M3-L}} = -\frac{E_{\text{UUUU}} - E_{\text{UUUD}} + E_{\text{DUUU}} + E_{\text{UDUU}} - E_{\text{UUDU}} - E_{\text{DUUD}} - E_{\text{UDUD}} + E_{\text{UUDD}}}{\langle S^2\rangle_{\text{UUUU}} - \langle S^2\rangle_{\text{UUUD}} + \langle S^2\rangle_{\text{DUUU}} + \langle S^2\rangle_{\text{UDUU}} - \langle S^2\rangle_{\text{UUDU}} - \langle S^2\rangle_{\text{DUUD}} - \langle S^2\rangle_{\text{UDUD}} + \langle S^2\rangle_{\text{UUDD}}} \quad (12)$$

$$J_{\text{M1-M2}} = -\frac{E_{\text{UUUU}} + E_{\text{UUUD}} - E_{\text{DUUU}} - E_{\text{UDUU}} + E_{\text{UUDU}} - E_{\text{DUUD}} - E_{\text{UDUD}} + E_{\text{UUDD}}}{\langle S^2\rangle_{\text{UUUU}} + \langle S^2\rangle_{\text{UUUD}} - \langle S^2\rangle_{\text{DUUU}} - \langle S^2\rangle_{\text{UDUU}} + \langle S^2\rangle_{\text{UUDU}} - \langle S^2\rangle_{\text{UDUD}} - \langle S^2\rangle_{\text{DUUD}} + \langle S^2\rangle_{\text{UUDD}}} \quad (13)$$

$$J_{\text{M1-M3}} = -\frac{E_{\text{UUUU}} + E_{\text{UUUD}} - E_{\text{DUUU}} + E_{\text{UDUU}} - E_{\text{UUDU}} - E_{\text{DUUD}} + E_{\text{UDUD}} - E_{\text{UUDD}}}{\langle S^2\rangle_{\text{UUUU}} + \langle S^2\rangle_{\text{UUUD}} - \langle S^2\rangle_{\text{DUUU}} + \langle S^2\rangle_{\text{UDUU}} - \langle S^2\rangle_{\text{UUDU}} - \langle S^2\rangle_{\text{DUUD}} + \langle S^2\rangle_{\text{UDUD}} - \langle S^2\rangle_{\text{UUDD}}} \quad (14)$$

$$J_{\text{M2-M3}} = -\frac{E_{\text{UUUU}} + E_{\text{UUUD}} + E_{\text{DUUU}} - E_{\text{UDUU}} - E_{\text{UUDU}} + E_{\text{DUUD}} - E_{\text{UDUD}} - E_{\text{UUDD}}}{\langle S^2\rangle_{\text{UUUU}} + \langle S^2\rangle_{\text{UUUD}} + \langle S^2\rangle_{\text{DUUU}} - \langle S^2\rangle_{\text{UDUU}} - \langle S^2\rangle_{\text{UUDU}} + \langle S^2\rangle_{\text{DUUD}} - \langle S^2\rangle_{\text{UDUD}} - \langle S^2\rangle_{\text{UUDD}}} \quad (15)$$

If all three metal atoms are assumed to be equivalent, the exchange coupling values were averaged and calculated according to the following equations:

$$J_1 = \frac{1}{3}\left(J_{\text{M1-L}} + J_{\text{M2-L}} + J_{\text{M3-L}}\right) \quad (16)$$

$$J_2 = \frac{1}{3}\left(J_{\text{M1-M2}} + J_{\text{M1-M3}} + J_{\text{M2-M3}}\right) \quad (17)$$

In this case, it is sufficient to calculate three different states “UUUU”, “UUUD”, “UUDU” (as “UUDU”, “UDUU”, and “DUUU” are treated as similar states). In this case, the following simplified expressions for J_1 and J_2 are available

$$J_1 = -\frac{E_{\text{UUUU}} - E_{\text{UUUD}}}{\langle S^2\rangle_{\text{UUUU}} - \langle S^2\rangle_{\text{UUUD}}} \quad (19)$$

$$J_2 = -\frac{2E_{\text{UUUU}} + E_{\text{UUUD}} - 3E_{\text{UUDU}}}{2\langle S^2\rangle_{\text{UUUU}} + \langle S^2\rangle_{\text{UUUD}} - 3\langle S^2\rangle_{\text{UUDU}}} \quad (20)$$

If two metals (M_1 and M_2) are assumed to be equivalent and the third metal atom (M_3) is different, the exchange coupling values are calculated as following:

$$J_{1(2)} = \frac{1}{2}\left(J_{M1\text{-}L} + J_{M2\text{-}L}\right) \quad (21)$$

$$J_{1(1)} = J_{M3\text{-}L} \quad (22)$$

$$J_{2(2)} = \frac{1}{2}\left(J_{M1\text{-}M3} + J_{M2\text{-}M3}\right) \quad (23)$$

$$J_{1(1)} = J_{M1\text{-}M2} \quad (24)$$

As complexes **1**, **2**, and **3** form dimeric structures the intermolecular exchange interaction between two molecules with total spins S_I and S_{II} was taken into account via the following additional term to the Hamiltonian (1)

$$\hat{H}_{MC\text{-}MC} = -2J_{MC\text{-}MC}\hat{S}_I\hat{S}_{II} \quad (25)$$

where $J_{MC\text{-}MC}$ is intermolecular exchange coupling value. $J_{MC\text{-}MC}$ was calculated according to the following equation

$$J_{MC\text{-}MC} = -\frac{E_F - E_{AF}}{\langle S^2\rangle_F - \langle S^2\rangle_{AF}} \quad (26)$$

where E_F and $<S^2>_F$ and E_{AF} and $<S^2>_{AF}$ are the energy and the expectation value of the squared spin operator for dimers with ferromagnetic and antiferromagnetic orientations of the spins of the constituent molecules (monomers) and the spin of each molecule corresponds to its ground state. E_F and $<S^2>_F$ and E_{AF} and $<S^2>_{AF}$ were derived from the BS-DFT calculations.

All complexes under quantum-chemical study are presented in Fig. S40.

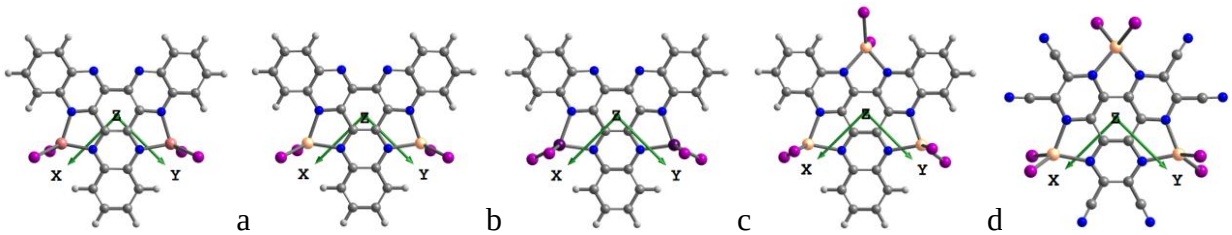

Figure S40. Coordinate system orientation for binuclear complexes **1** (a), **2** (b), **3** (c) and trinuclear complexes **4** (d) and **5** (e).

Complexes 1–4

For complexes **1**–**4** spin states energies, spin densities and exchange-coupling values were calculated at both DFT and SA-CASSCF/NEVPT2 levels for various spin states (Fig. S41, S42). In complex **1**, high-spin (HS; S = 3/2) and low-spin (LS; S = 1/2) states of Co(II) are realized. In complexes **2** and **4**, HS (S = 2) and intermediate-spin (IS; S = 1) states of Fe(II) are realized. In complex **3**, HS (S = 5/2), IS (S = 3/2) and LS (S = 1/2) states of Mn(II) are realized.

Calculations confirmed the HS state of the Co(II), HS state of the Fe(II) and HS state of the Mn(II) ions in all complexes. For binuclear complexes **1**, **2**, **3** and trinuclear complex **4**, the antiferromagnetic metal-radical ($HATNA^{-1}$, S = 1/2) orientation was confirmed by both DFT and SA-CASSCF/NEVPT2 calculations (Fig. S41, S42, Table S5, S6).

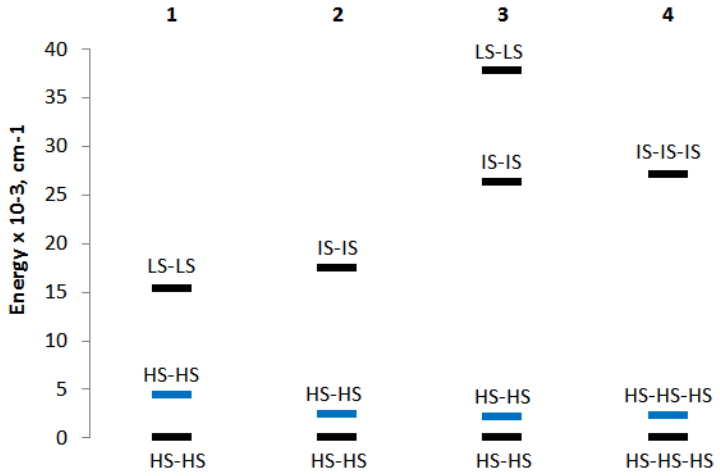

Figure S41. Energy levels as a function of spin configuration of magnetic centers for complexes **1**–**4** from DFT calculations**.** The blue levels correspond to the ferromagnetic ligand spin orientation relative to the Co/Fe/Mn magnetic centers spin.

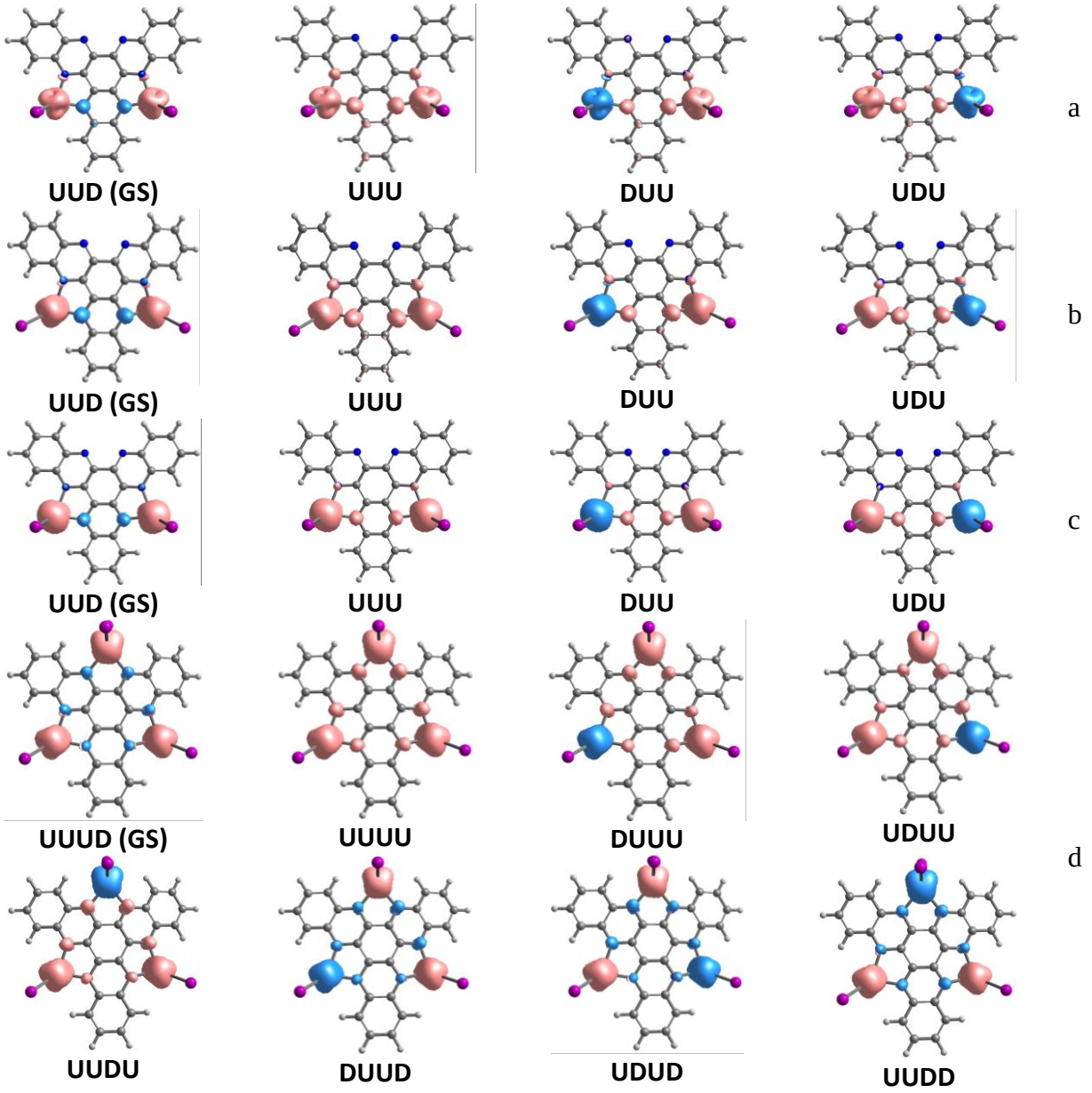

Figure S42. B3LYP BS spin densities for the **UUU**, **UUD**, **DUU**, and **UDU** states of the binuclear complexes **1** (a), **2** (b), **3** (c) and spin densities for the **UUUD**, **UUUU**, **DUUU**, **UDUU**, **UUDU**, **DUUD**, **UDUD** and **UUDD** spin states of the triuclear complex **4** (d). GS – ground spin state. Positive and negative spin densities are shown in pink and blue colors, respectively.

Table S5. Energies (a.e. Hartree) of spin solutions, spin expectations and exchange-coupling values from DFT BS calculation for complex **1**–**3**

		solution	UUU	UUD	DUU	UDU	J_{M1-L} J_{M2-L}	J_1	J_2
1	BP86	**E**	-32505.3486	-32505.3690	-32505.3611	-32505.3610	-669.2	**-671.0**	**-52.9**
		<S²>	15.780	9.122	3.171	3.167	-672.8		
	B3LYP	**E**	-32500.1799	-32500.1975	-32500.1915	-32500.1918	-622.6	**-612.4**	**-71.0**
		<S>²	15.778	9.487	3.579	3.574	-602.2		
2	BP86	**E**	-32264.0435	-32264.0524	-32264.0474	-32264.0474	230.9	**-230.9**	**7.5**
		<S>²	24.792	16.388	4.538	4.537	230.9		
	B3LYP	**E**	-32258.9295	-32258.9406	-32258.9346	-32258.9346	-296.6	**-296.4**	**6.7**
		<S>²	24.784	16.570	4.650	4.650	-296.2		
3	BP86	**E**	-32035.8202	-32035.8332	-32035.8274	-32035.8277	-283.7	**-277.2**	**-7.1**
		<S>²	35.782	25.425	5.544	5.535	-270.7		
	B3LYP	**E**	-32030.7766	-32030.7862	-32030.7816	-32030.7818	-212.4	**-208.3**	**-3.0**
		<S>²	35.778	25.615	5.682	5.679	-204.1		

Table S6. Energies (a.e. Hartree) of spin solutions, spin expectations and exchange-coupling values from DFT BS calculation for complex **4**

	solution					J_{M1-L} J_{M2-L} J_{M3-L}	J_1	J_{M1-M3} J_{M2-M3} J_{M1-M2}	J_2
BP86		**UUUU**	**UUUD**	**DUUU**	**UDUU**	-173.7 -171.1 -165.5	**-170.1**	-6.5 -5.9 -1.6	**-4.6**
	E	-47770.3102	**-47770.3205**	-47770.3158	-47770.3147				
	<S>²	48.856	36.605	12.745	12.739				
		UUDU	**DUUD**	**UUDD**	**UDUD**				
	E	-47770.3150	-47770.3170	-47770.3170	-47770.3175				
	<S>²	12.748	8.633	8.633	8.644				
B3LYP		**UUUU**	**UUUD**	**DUUU**	**UDUU**	-187.5 -192.3 -179.0	**-186.2**	-2.9 -6.2 -6.2	**-5.1**
	E	-47763.0206	**-47763.0310**	-47763.0248	-47763.0251				
	<S>²	48.804	36.582	12.706	12.697				
		UUDU	**DUUD**	**UUDD**	**UDUD**				
	E	-47763.0246	-47763.0282	-47763.0283	-47763.0283				
	<S>²	12.686	8.623	8.638	8.638				

For all complexes **1**–**4**, the BS spin density demonstrated a significant spin delocalization of metal spins on the π-system of the $HATNA^{-1}$ (S = 1/2) bridging ligand (Table S7). Complex **1** exhibited the greatest spin delocalization, which was confirmed by the largest value of the calculated magnetic exchange interaction.

Table S7. Spin density from DFT BS B3LYP Mulliken spin population analysis.

Complex	**Unpaired electrons**	**Spin population on metal site**			**% delocalization of metal spins on the ligand**
		M_1	**M_2**	**M_3**	
1	3	2.59	2.59	–	13.7
2	4	3.65	3.65	–	8.8
3	5	4.78	4.78	–	4.4
4	4	3.65	3.65	3.64	8.8

For binuclear complexes **1** (a), **2** (b), **3** (c), molecular complexes (MCs) dimers were considered. The energies, spin densities and exchange-coupling values were calculated at the DFT B3LYP level (Fig. S43, Table S8). The calculations indicated weak ferromagnetic coupling between MCs for all complexes: $J_{MC\text{-}MC}$ ~ 0.05 cm^{-1} for complex **1**, $J_{MC\text{-}MC}$ ~ 0.04 cm^{-1} for complex **2,** and $J_{MC\text{-}MC}$ ~ 0.02 cm^{-1} for complex **3**. Taking into account MC-MC interaction allows us to correctly describe the $\chi_M T$ curves in the POLY_ANISO module, as it describes the intermolecular interaction, which is crucial for these compounds.

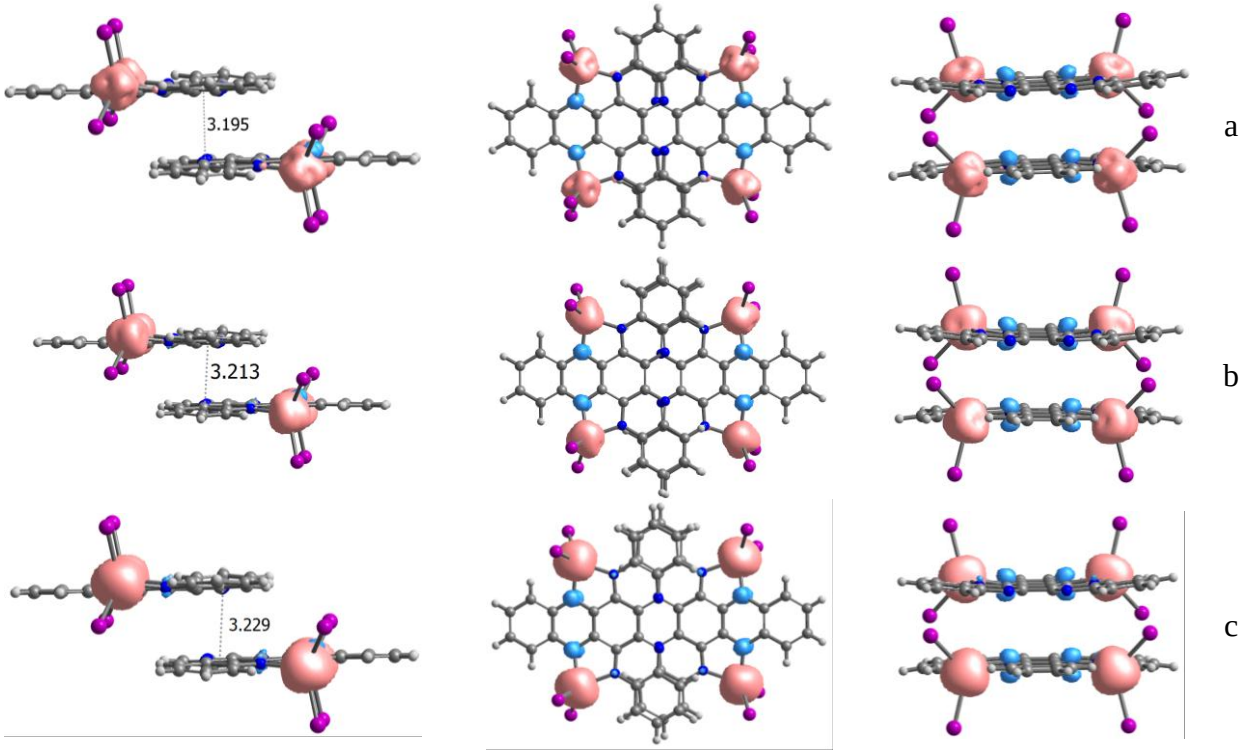

Figure S43. Different views on B3LYP BS spin densities for the dimer of the binuclear complexes **1** (a), **2** (b), **3** (c). Positive and negative spin densities are shown in pink and blue colors, respectively. The numbers in the left column represent the distances (in Å) between the planes formed by the middle C6 rings of HATNA molecules.

Table S8. Energies (a.e. Hartree) of spin solutions, spin expectations and exchange-coupling values from DFT BS B3LYP calculation for MC-MC dimers in **1**–**3**.

MC-MC	solution	FM	AFM	J_{MC-MC}
1	**E** $\langle S \rangle^2$	-65000.3812 31.473	-65000.3812 6.472	**0.046**
2	**E** $\langle S \rangle^2$	-64517.8673 57.640	-64517.8673 8.640	**0.036**
3	**E** $\langle S \rangle^2$	-64061.2075 91.731	-64061.2075 10.731	**0.021**

For all complexes the SA-CASSCF/NEVPT2 calculations confirmed HS of metal ions. Table S8 presents the magnetic parameters of the magnetic centers obtained from SA-CASSCF/NEVPT2 calculations of the modified structures in which one (complexes **1**–**3**) or two (complex **4**) metal ions were replaced by Zn(II). The table also contains exchange-coupling values from SA-CASSCF/NEVPT2 calculations assuming that both (complexes **1**–**3**) or all three (complex **4**) metal ions are equivalent. The calculated $\chi_M T$ dependences (Fig. S44) are in good agreement with the experimental data.

Table S9. ZFS parameters, g-factor and exchange-coupling values from SA-CASSCF/NEVPT2 calculation for complexes **1**–**4**.

Complex	**Metal site**	***D*, cm^{-1}**	***E*/*D***	***g*-factor**	***J*$_1$(M-L), cm^{-1}**	***J*$_2$(M-M), cm^{-1}**
1	Co_1	9.21	0.25	2.414	-689.3	-47.0
	Co_2	9.17	0.24	2.434		
2	Fe_1	-10.01	0.16	2.270	-457.5	6.4
	Fe_2	-10.01	0.16	2.270		
3	Mn_1	0.37	0.02	2.102	-298.3	-8.3
	Mn_2	0.37	0.02	2.102		
4	Fe_1	-14.47	0.14	2.373	-183.3	-16.1
	Fe_2	-14.77	0.10	2.393		
	Fe_3	-16.56	0.09	2.424		

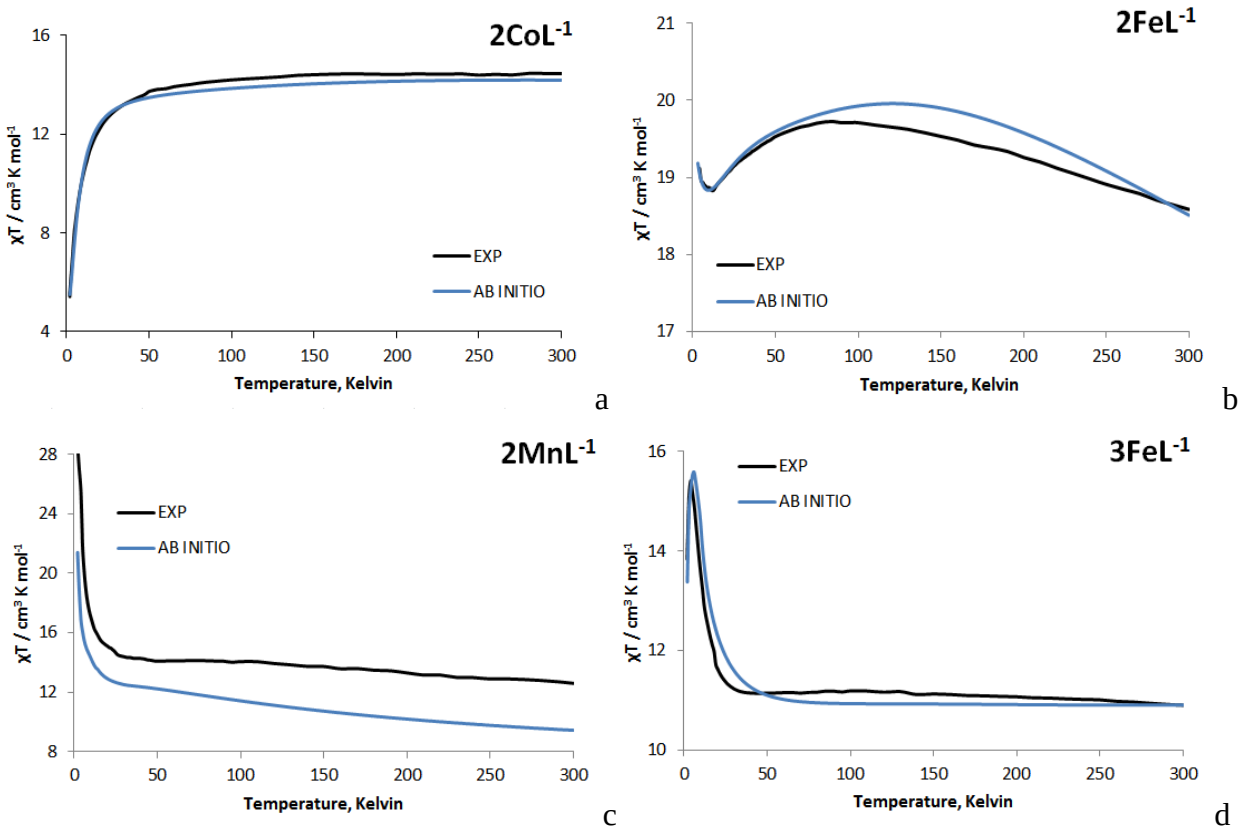

Figure S44. Calculated (POLY_ANISO module) $\chi_M T$ dependencies (blue) vs. experimental data (black) for complexes **1** (a), **2** (b), **3** (c), **4** (d) with parameters from Tables S7 and S8. For complexes **1** and **2** the data are calculated per two formula units.

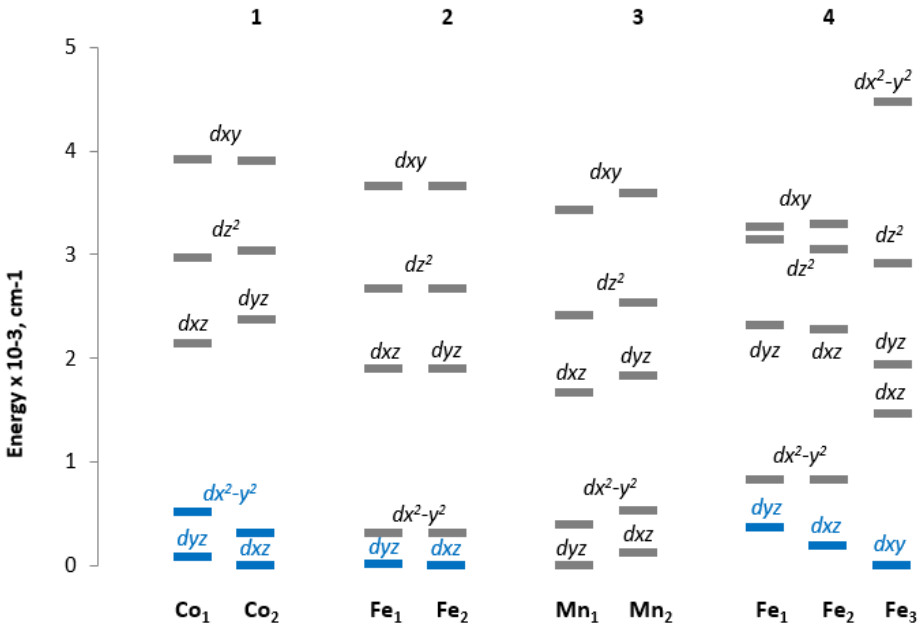

Figure S45. Ligand field splitting for the Co/Fe/Mn magnetic centers in complexes **1**–**4** (with uncharged ligand HATNA^0) obtained from SA-CASSCF/NEVPT2 calculations. The blue levels present doubly occupied orbitals.

Figures S45 and S46 demonstrate, that the unpaired electrons in mononuclear paramagnetic fragment of complex **1** are located at *dxy*, dz^2 and *dxz*/*dyz* (Co_1/Co_2) orbitals. The only orbital providing overlap with the ligand's π-system is *dxz*/*dyz*. The mixing of the *dxz*/*dyz* metal orbital and the ligand π-orbital induces an efficient spin density delocalization in complex **1** with the charged ligand (Fig. S50).

Unpaired electrons in mononuclear paramagnetic fragment of complex **2** are located at *dxy*, dz^2, *dxz*/*dyz* and dx^2-y^2 (Fe_1/Fe_2) orbitals. The only orbital providing overlap with the ligand's π-system is *dxz*/*dyz*. The mixing of the *dxz*/*dyz* orbital and the ligand π-orbital similarly induces an efficient spin density delocalization in complex **2** (Fig. S44, S46, S50).

Unpaired electrons in mononuclear paramagnetic fragment of complex **3** are located at *dxy*, dz^2, *dxz*/*dyz*, *dyz*/*dxz* and dx^2-y^2 (Mn_1/Mn_2) orbitals. The only orbitals providing overlap with the ligand's π system are *dxz*/*dyz* and *dyz*/*dxz*. The mixing of the *dxz*/*dyz* or *dyz*/*dxz* orbitals and the ligand π-orbital similarly induces an efficient spin density delocalization in complex **3** (Fig. S45, S48, S52).

Unpaired electrons in mononuclear paramagnetic fragment of complex **4** are located at *dxy*, dz^2, *dxz*/*dyz*/dz^2 and dx^2-y^2 (Fe_1/Fe_2/Fe_3) orbitals. The only orbital providing overlap with the ligand's π-system is *dxz*/*dyz*/dz^2. The mixing of the *dxz*/*dyz*/dz^2 orbital and the ligand π-orbital induces an efficient spin density delocalization in complex **4** (Fig. S45, S49, S53).

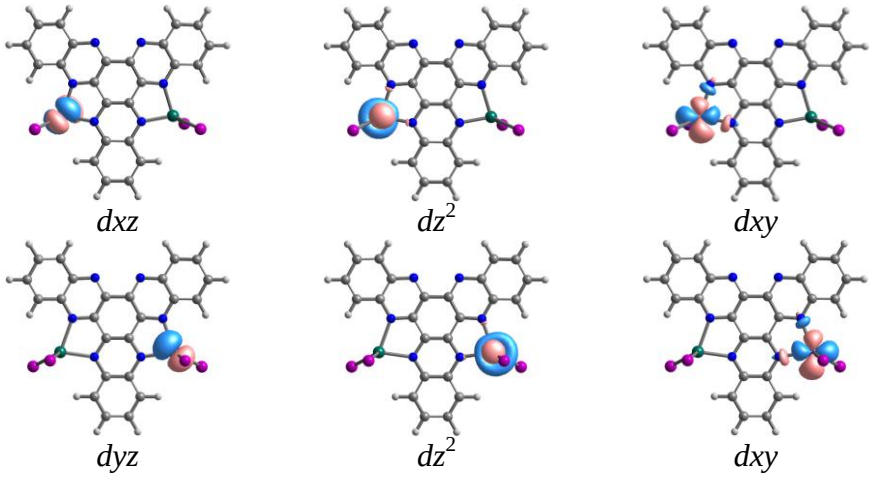

Figure S46. The SOMO orbitals Co_1 and Co_2 of complex **1** with uncharged ligand from SA-CASSCF(7,5)/NEVPT2 calculations.

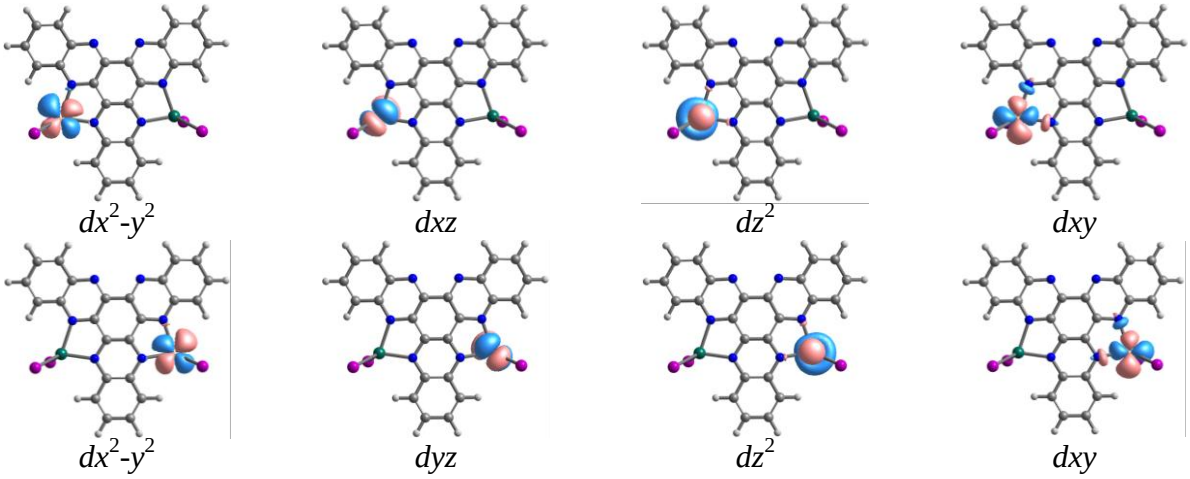

Figure S47. The SOMO orbitals Fe_1 and Fe_2 of complex **2** with uncharged ligand from SA-CASSCF(6,5)/NEVPT2 calculations.

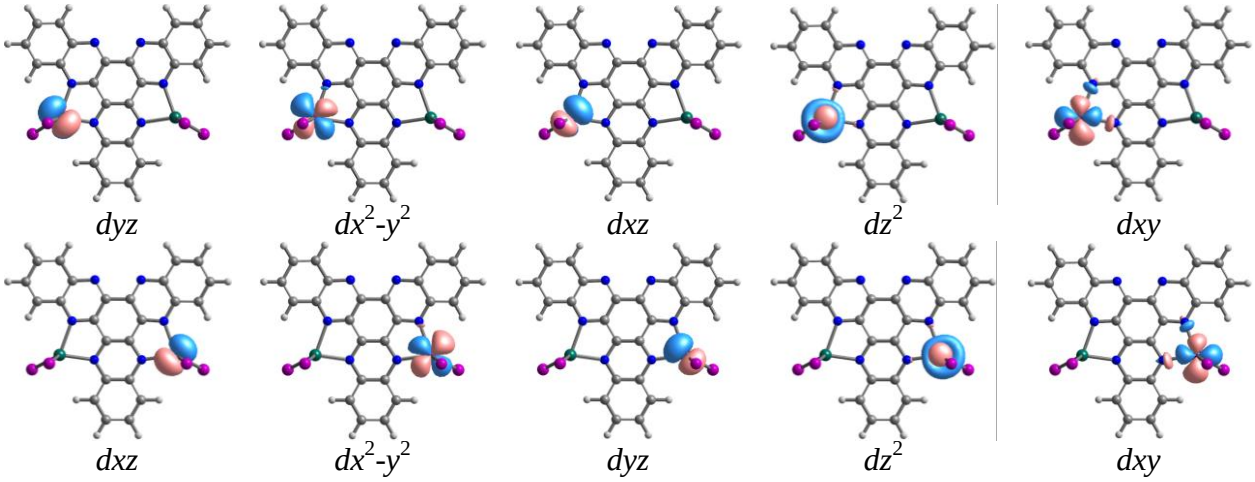

Figure S48. The SOMO orbitals Mn_1 and Mn_2 of complex **3** with uncharged ligand from SA-CASSCF(5,5)/NEVPT2 calculations.

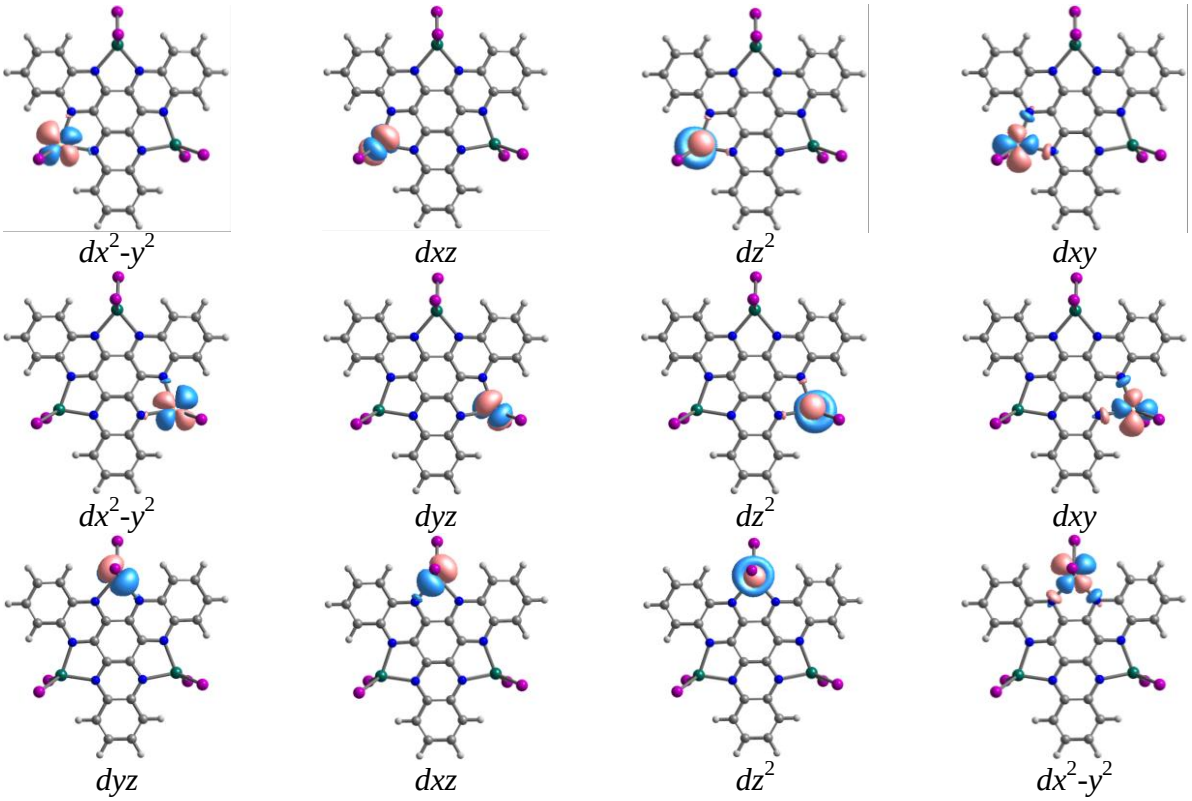

Figure S49. The SOMO orbitals Fe_1, Fe_2 and Fe_3 of complex **4** with uncharged ligand from SA-CASSCF(6,5)/NEVPT2 calculations.

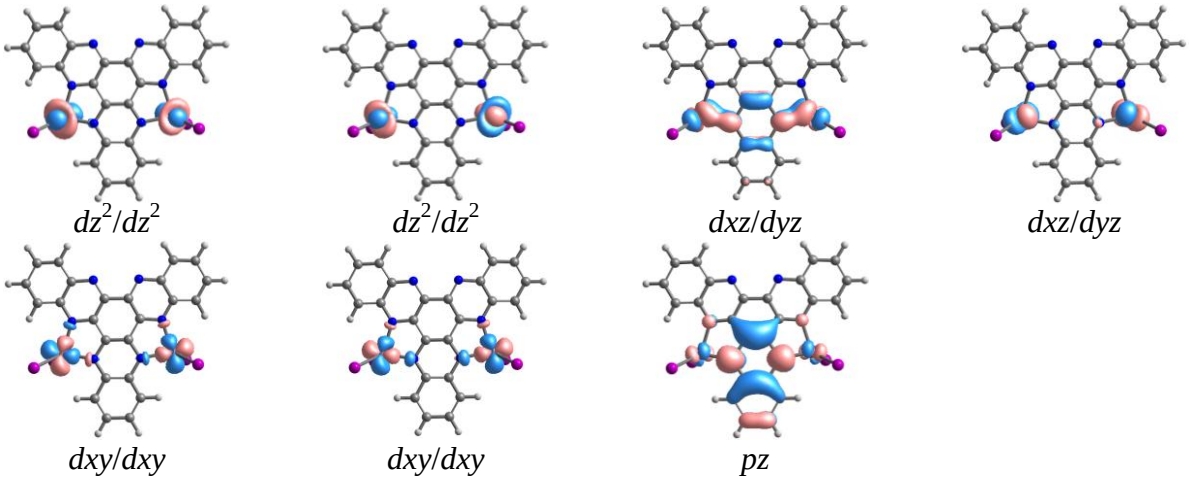

Figure S50. The SOMO orbitals of complex **1** with $HATNA^{-1}$ (S = 1/2) ligand from SA-CASSCF(15,11)/NEVPT2 calculations.

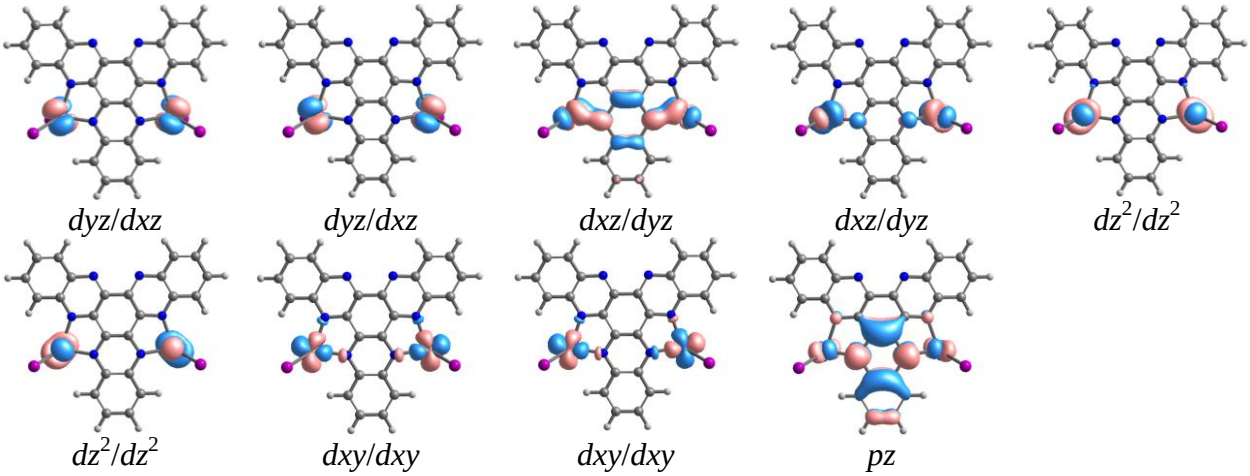

Figure S51. The SOMO orbitals of complex **2** with $HATNA^{-1}$ (S = 1/2) ligand from SA-CASSCF(13,11)/NEVPT2 calculations.

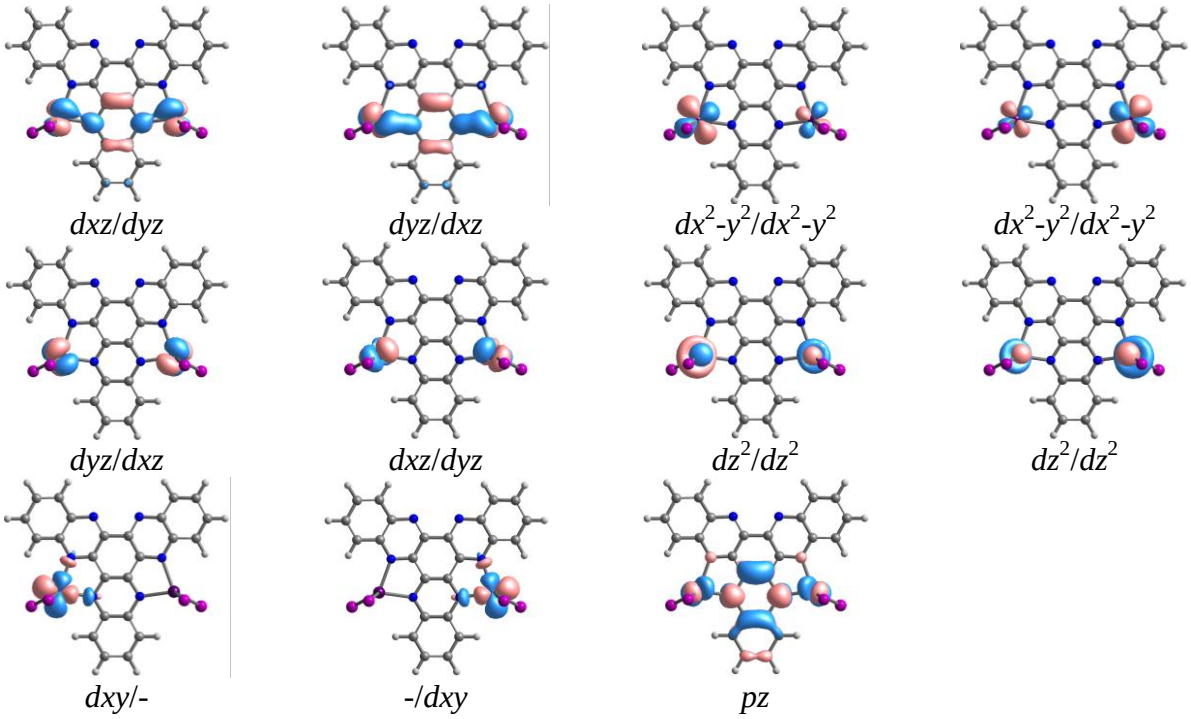

Figure 52. The SOMO orbitals of complex **3** with $HATNA^{-1}$ (S = 1/2) ligand from SA-CASSCF(11,11)/NEVPT2 calculations.

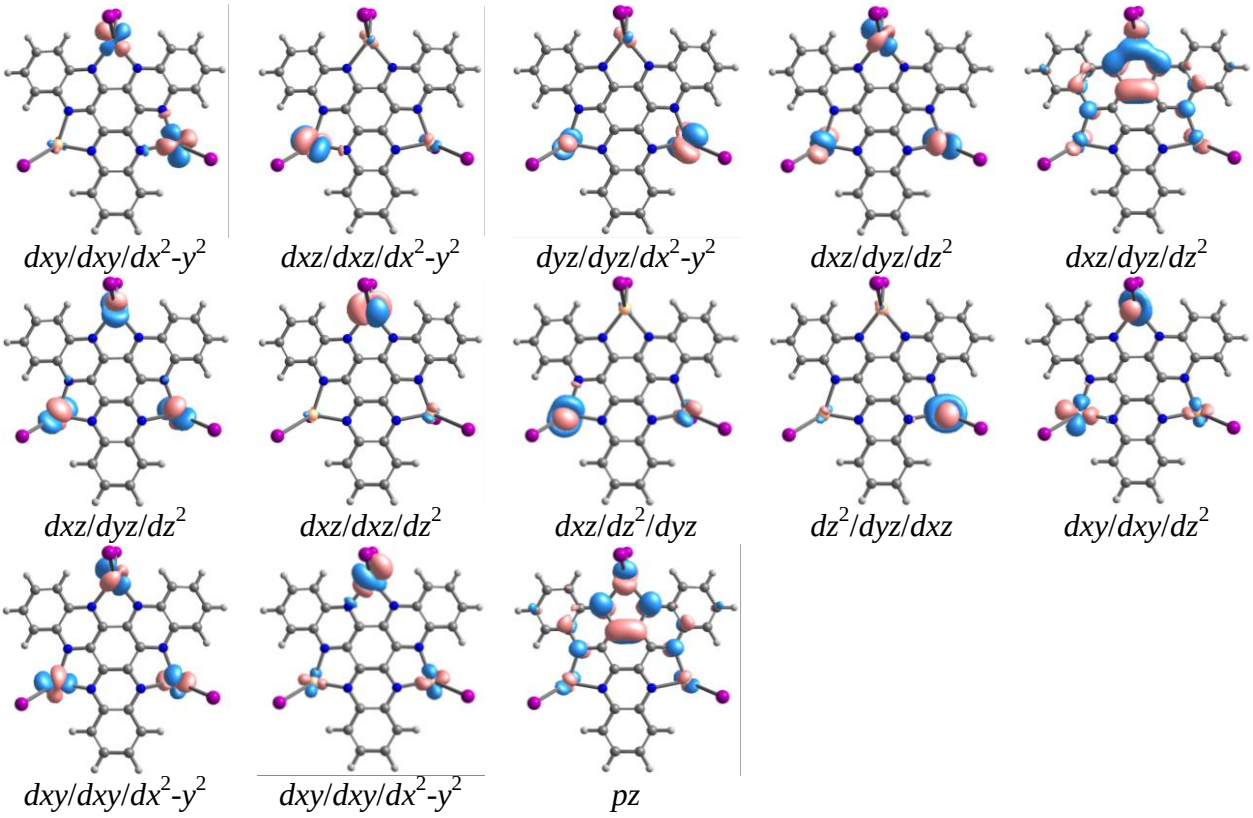

Figure S53. The SOMO orbitals of complex **4** with $HATNA^{-1}$ (S = 1/2) ligand from SA-CASSCF(19,11)/NEVPT2 calculations.

Complex 5

For complex **5**, our computational resources did not allow CASSCF/NEVPT2 calculations for the full structure. The full complex **5** was calculated in the framework of the DFT method, and modified structures with Fe(II) ions replaced by Zn(II) were calculated using the SA-CASSCF/NEVPT2 method.

The DFT calculations of both the full structure and the modified structure with all three Fe(II) ions replaced by Zn(II) and charged ligand resulted in high-spin state of the ligand $HAT(CN)_6^{-3}$ (S = 3/2).

Meanwhile, CASSCF/NEVPT2 calculations of the modified structure, in which all three Fe(II) ions were replaced by Zn(II), showed a doublet state of the ligand $HAT(CN)_6^{-3}$ (S = 1/2), with each π-orbital occupied by one electron and one electron antiferromagnetically oriented relative to the other two. The CASSCF/NEVPT2 calculation are consistent with experimental results indicating a low-spin sate of the ligand $HAT(CN)_6^{-3}$ (S = 1/2). This is why the DFT method cannot be applied to estimate the exchange coupling parameters in complex **5**.

Thus, a special approach was applied. The metal-ligand coupling values for complex **5** were derived from the SA-CASSCF/NEVPT2 calculations of three modified structures in which two of three Fe(II) ions were replaced by Zn(II) and the charged ligand was in the low-spin state (S = 1/2). The calculations confirmed antiferromagnetic metal-radical ($HAT(CN)_6^{-3}$, S = 1/2) orientation. The metal-ligand coupling values were close for all three Fe(II) ions (see Table S9), and J_1(M-L) = -250 cm^{-1} was used for calculation of $\chi_M T$ dependence in POLY_ANISO module. For good agreement with the experimental $\chi_M T$, J_2(M-M) = -10 cm^{-1} was chosen. The satisfactory agreement with experimental $\chi_M T$ was obtained (see Figure S54).

Table S10. ZFS parameters, g_z tensor and exchange-coupling values from SA-CASSCF/NEVPT2 calculation for complex **5**.

Metal site	D, cm^{-1}	E/D	g-factor	J_1(M-L), cm^{-1}
Fe_1	5.20	0.22	2.158	-256.0
Fe_2	5.20	0.22	2.158	-283.7
Fe_3	-6.25	0.09	2.159	-247.7

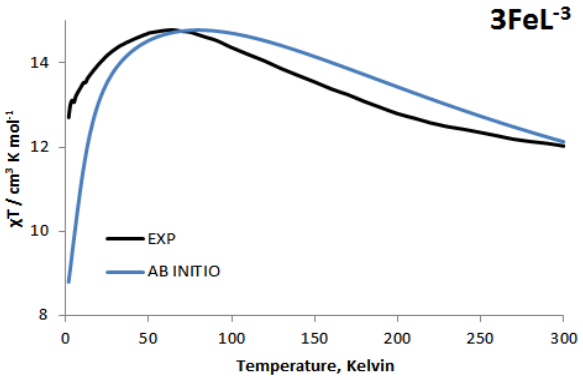

Figure S54. Calculated (POLY_ANISO module) $\chi_M T$ dependence (blue) vs. experimental data (black) for complex **5**.

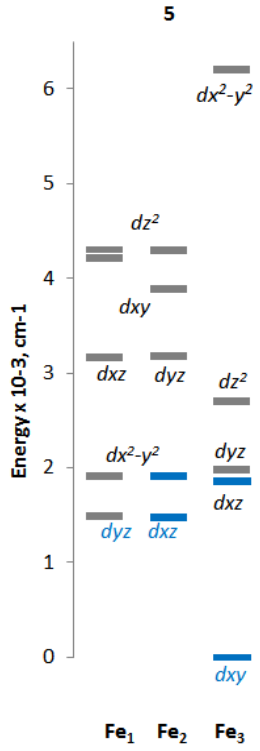

Figure S55. Ligand field splitting for Fe magnetic centers in complex **5** (with uncharged ligand $HAT(CN)_6^0$) obtained from SA-CASSCF/NEVPT2 calculations. The blue levels present doubly occupied orbitals.

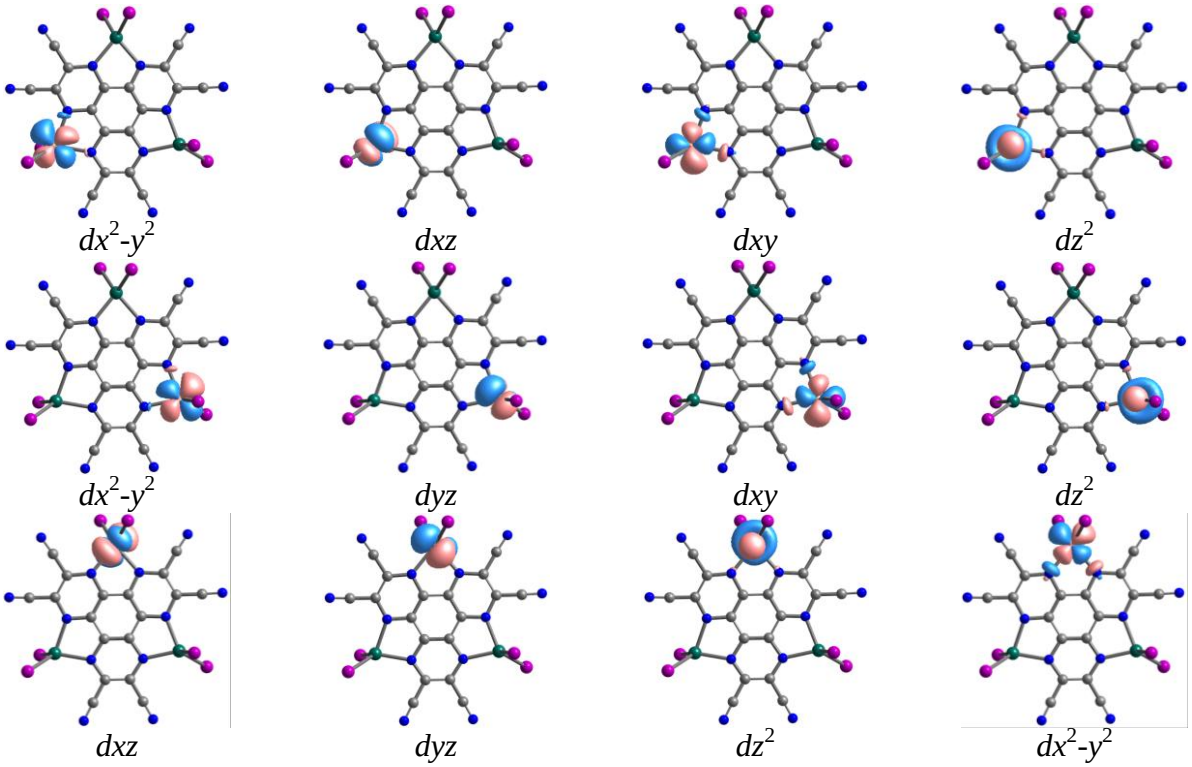

Figure S56. The SOMO orbitals Fe_1, Fe_2 and Fe_3 of complex **5** with uncharged ligand from SA-CASSCF(6,5)/NEVPT2 calculations.

Unpaired electrons of Fe(II) in the mentioned above modified structures of (with two metals replaced by Zn(II)) complex **5** are located at *dxy* (Fe_1/Fe_2), dz^2, *dxz*/*dyz*/*dxz*,*dyz* and dx^2-y^2 (Fe_1/Fe_2/Fe_3) orbitals. The only orbital providing overlap with the ligand's π-system is *dxz*/*dyz*. The mixing of the *dxz*/*dyz* orbital and the ligand π-orbital induces an efficient spin density delocalization in the complexes **5** with charged ligand (Fig. S55,56).

References

1. M. V. Mikhailenko, V. V. Ivanov, M.A. Faraonov, A. V. Kuzmin, S. S. Khasanov, I. A. Yakushev, N. N. Breslavskaya, E. N. Timokhina, T. Yu. Astakhova, A. Otsuka, H. Yamochi, H. Kitagawa and D. V. Konarev, Effect of nuclearity and reduction state of the central ligand on magnetic properties of hexaazatrinaphthylene-based cobalt(II) and iron(II) complexes: from extremely weak to record-breaking antiferromagnetic exchange interaction, *Inorg. Chem. Front.*, 2024, **11**, 7563–7575.
2. N. F. Chilton, R. P. Anderson, L. D. Turner, A. Soncini and K. S. Murray, PHI: A powerful new program for the analysis of anisotropic monomeric and exchange-coupled polynuclear *d*- and *f*-block complexes, *J. Comput. Chem.*, 2013, **34**, 1164–1175.
3. M. V. Mikhailenko, S.S. Khasanov, A.F. Shestakov, A.V. Kuzmin, A. Otsuka, H. Yamochi, H. Kitagawa and D. V. Konarev, Weak Antiferromagnetic Exchange and Ferromagnetic Alignment of Fe^{II} (S = 2) Spins in Differently Charged $\{HAT\cdot(Fe^{II}Cl_2)_3\}^n$ (n = 2– and 3–) Assemblies of Hexaazatriphenylenes (HAT), *Chem. Eur. J.*, 2022, **28**, e202104165.
4. M. V. Mikhailenko, V. V. Ivanov, S. S. Khasanov, A. F. Shestakov, A. V. Kuzmin, A. Otsuka, H. Yamochi, H. Kitagawa and D. V. Konarev, Different magnetic behavior and spin states for coordination $\{L\cdot[M^{II}(Hal)_2]_3\}^{3-}$ assemblies (Hal = Cl or I) of radical-trianion hexaazatriphenylenes (L) with three high-spin Fe^{II} (S = 2) or Co^{II} (S = 3/2) centers, *Dalton Trans.*, 2023, **52**, 11222-11233.

5. F. Neese, Software update: the ORCA program system, version 6.0 WIRES, *Comput. Molec. Sci.*, 2025, **15**, e70019.
6. P. J. Stephens, F. J. Devlin, C. F. Chabalowski and M. J. Frisch, Ab initio calculation of the thermochemistry and spectroscopy of molecules using density functional theory, The Journal of Physical Chemistry, 1994, **98**, 11623-11627.
7. P. Pollak and F. Weigend, Segmented Contracted Error-Consistent Basis Sets of Double- and Triple-ζ Valence Quality for One- and Two-Component Relativistic All-Electron Calculations, *J. Chem. Theory Comput.*, 2017, **13**, 3696-3705.
8. F. Neese, F. Wennmohs, A. Hansen and U. Becker, Efficient, approximate and parallel Hartree-Fock and hybrid DFT calculations. A 'chain-of-spheres' algorithm for the Hartree-Fock exchange, *Chem. Phys.*, 2009, **356**, 98−109.
9. G. L. Stoychev, A. A. Auer and F. Neese, Automatic Generation of Auxiliary Basis Sets, *J. Chem. Theory Comput.*, 2017, **13**, 554−562.
10. D. Peng, N. Middendorf, F. Weigend and M. Reiher, An efficient implementation of two-component relativistic exact-decoupling methods for large molecules, *J. Chem. Phys.*, 2013, **138**, 184105.
11. F. Neese, Definition of corresponding orbitals and the diradical character in broken symmetry DFT calculations on spin coupled systems, *J. Phys. Chem. Solids*, 2004, **65**, 781−785.
12. J. P. Perdew, J. Tao and S. Kummel, Uniform Density Limit of Exchange-Correlation Energy Functionals, *ACS Symp. Ser.*, 2007, **958**, 13−25.

13. C. Angeli, R. Cimiraglia, S. Evangelisti, T. Leininger and J.-P. Malrieu, Introduction of n-electron valence states for multireference perturbation theory, *J. Chem. Phys.*, 2001, **114**, 10252–10264.
14. Y. Guo, K. Sivalingam, V. G. Chilkuri and F. Neese, Approximations of density matrices in N-electron valence state second-order perturbation theory (NEVPT2). III. Large active space calculations with selected configuration interaction reference, *J. Chem. Phys.*, 2025, **162**, 144110.
15. F. Neese, Efficient and accurate approximations to the molecular spin-orbit coupling operator and their use in molecular-tensor calculations, *J. Chem. Phys.*, 2005, **122**, 034107.
16. D. Ganyushin and F. Neese, First-principles calculations of zero-field splitting parameters, *J. Chem. Phys.*, 2006, **125**, 024103.
17. M. Atanasov, D. Ganyushin, K. Sivalingam and F. Neese, in Molecular Electronic Structures of Transition Metal Complexes II, (ed. D. M. P. Mingos, P. Day and J. P. Dahl), *SpringerBerlin Heidelberg*, Berlin, Heidelberg, 2012, pp. 149−220.
18. S. K. Singh, J. Eng, M. Atanasov and F. Neese, Covalency and chemical bonding in transition metal complexes: An ab initio based ligand field perspective, *Coord. Chem. Rev.*, 2017, **344**, 2−25.
19. K. Yamaguchi, Y. Toyoda and T. Fueno, A generalized MO (GMO) approach to unstable molecules with quasi-degenerate electronic states: *ab initio* GMO calculations of intramolecular effective exchange integrals and designing of organic magnetic polymers, *Synthetic Met.*, 1987, **19**, 81−86.

20. M. Shoji , K. Koizumi, Y. Kitagawa, T. Kawakami, S. Yamanaka, M. Okumura and K. Yamaguchi, A general algorithm for calculation of Heisenberg exchange integrals *J* in multispin systems, *Chem. Phys. Lett.*, 2006, **432**, 343–347.